

NAVAL POSTGRADUATE SCHOOL

Monterey, California



THESIS

DEVELOPMENT AND VALIDATION OF A SECOND GENERATION VISIBILITY-BASED MODEL FOR PREDICTING SUBJECTIVE AND OBJECTIVE MINIMUM RESOLVABLE TEMPERATURE DIFFERENCE PERFORMANCE FOR STARING THERMAL IMAGING SYSTEMS

by

Michael S. Groen

December, 1995

Thesis Co-Advisors:

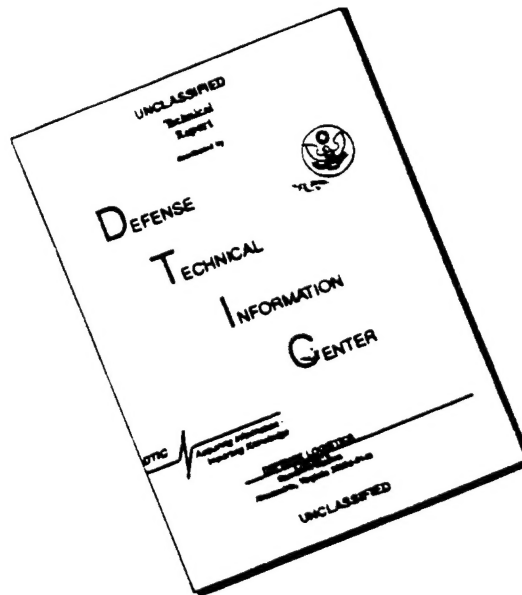
Alfred W. Cooper
Ron J. Pieper

Approved for public release; distribution is unlimited.

DTIC QUALITY INSPECTED 1

19960329 100

DISCLAIMER NOTICE



THIS DOCUMENT IS BEST QUALITY AVAILABLE. THE COPY FURNISHED TO DTIC CONTAINED A SIGNIFICANT NUMBER OF PAGES WHICH DO NOT REPRODUCE LEGIBLY.

REPORT DOCUMENTATION PAGEForm Approved
OMB No. 0704-0188

Public reporting burden for this collection of information is estimated to average 1 hour per response, including the time reviewing instructions, searching existing data sources, gathering and maintaining the data needed, and completing and reviewing the collection of information. Send comments regarding this burden estimate or any other aspect of this collection of information, including suggestions for reducing this burden to Washington Headquarters Services, Directorate for Information Operations and Reports, 1215 Jefferson Davis Highway, Suite 1204, Arlington, VA 22202-4302, and to the Office of Management and Budget, Paperwork Reduction Project (0704-0188), Washington, DC 20503.

1. AGENCY USE ONLY (Leave Blank)		2. REPORT DATE December 1995	3. REPORT TYPE AND DATES COVERED Master's Thesis
4. TITLE AND SUBTITLE DEVELOPMENT AND VALIDATION OF A SECOND GENERATION VISIBILITY-BASED MODEL FOR PREDICTING SUBJECTIVE AND OBJECTIVE MINIMUM RESOLVABLE TEMPERATURE DIFFERENCE PERFORMANCE FOR STARING THERMAL IMAGING SYSTEMS (U)			5. FUNDING NUMBERS
6. AUTHOR(S) Groen, Michael S.			
7. PERFORMING ORGANIZATION NAME(S) AND ADDRESS(ES) Naval Postgraduate School Monterey, CA 93943-5000			8. PERFORMING ORGANIZATION REPORT NUMBER
9. SPONSORING/ MONITORING AGENCY NAME(S) AND ADDRESS(ES) Naval Command and Control and Ocean Surveillance Center 53570 Silvergate Ave. San Diego, CA 92152-5230			10. SPONSORING/ MONITORING AGENCY REPORT NUMBER Project MPB45R5T25
11. SUPPLEMENTARY NOTES The views expressed in this thesis are those of the author and do not reflect the official policy or position of the Department of Defense or the United States Government.			
12a. DISTRIBUTION / AVAILABILITY STATEMENT Approved for public release; distribution is unlimited.			12b. DISTRIBUTION CODE
13. ABSTRACT (Maximum 200 words) Several models have been proposed to predict the minimum resolvable temperature difference (MRTD) performance of second generation thermal imaging systems (TIS) which incorporate staring focal plane arrays. It has been suggested that these models are not accurate for predicting the performance of second generation staring focal plane arrays which have severe phasing or sampling characteristics not amenable to linear modulation transfer function analysis. A second problem with these models is that they require a particular set of assumptions concerning the observer eye/brain recognition process, limiting their usefulness in the prediction of performance for systems that incorporate automatic target recognition (ATR) devices. In this thesis, a new model is presented for predicting the MRTD performance of second generation thermal imagers based on a minimum threshold input contrast, and a contrast reduction factor due to aliasing and blurring effects. The model makes no assumptions regarding the recognition process, which allows a separate threshold value to be defined for either a human or machine observer. The model incorporates aliasing concepts, and extends performance prediction beyond the nominal Nyquist rate of the system. The model's predictions are compared to the predictions of the current standard FLIR92 model and measured laboratory results for two different staring focal plane array imagers. In both cases, the models's predictions match measured results more closely than the predictions of FLIR92.			
14. SUBJECT TERMS thermal imaging, infrared, minimum resolvable temperature difference			15. NUMBER OF PAGES 183
			16. PRICE CODE
17. SECURITY CLASSIFICATION OF REPORT Unclassified	18. SECURITY CLASSIFICATION OF THIS PAGE Unclassified	19. SECURITY CLASSIFICATION OF ABSTRACT Unclassified	20. LIMITATION OF ABSTRACT UL

Approved for public release; distribution is unlimited.

**DEVELOPMENT AND VALIDATION OF A SECOND GENERATION
VISIBILITY-BASED MODEL FOR PREDICTING SUBJECTIVE AND OBJECTIVE
MINIMUM RESOLVABLE TEMPERATURE DIFFERENCE FOR
STARING THERMAL IMAGING SYSTEMS**

Michael S. Groen
Captain, United States Marine Corps
B.S., Calvin College, 1986

Submitted in partial fulfillment of the
requirements for the degrees of

**MASTER OF SCIENCE IN ELECTRICAL ENGINEERING
and
MASTER OF SCIENCE IN APPLIED PHYSICS**

from the

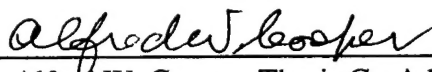
**NAVAL POSTGRADUATE SCHOOL
December, 1995**

Author:

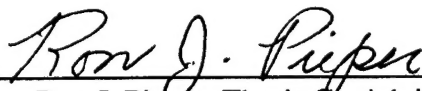


Michael S. Groen

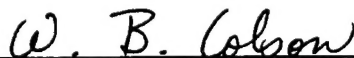
Approved by:



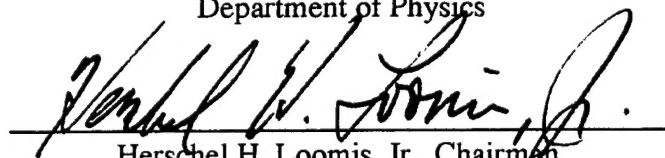
Alfred W. Cooper, Thesis Co-Advisor



Ron J. Pieper, Thesis Co-Advisor



William B. Colson, Chairman,
Department of Physics



Herschel H. Loomis, Jr., Chairman,
Department of Electrical and Computer Engineering

ABSTRACT

Several models have been proposed to predict the minimum resolvable temperature difference (MRTD) performance of second generation thermal imaging systems (TIS) which incorporate staring focal plane arrays. It has been suggested that these models are not accurate for predicting the performance of second generation staring focal plane arrays which have severe phasing or sampling characteristics not amenable to linear modulation transfer function analysis. A second problem with these models is that they require a particular set of assumptions concerning the observer eye/brain recognition process, which limits their usefulness in the prediction of the performance for systems that incorporate automatic target recognition (ATR) devices. In this thesis, a new model is presented for predicting the MRTD performance of second generation thermal imagers based on a minimum threshold input contrast, and a contrast reduction factor due to aliasing and blurring effects. The model makes no assumptions regarding the recognition process, which allows a separate threshold value to be defined for either a human or machine observer. The model incorporates aliasing concepts, and extends performance prediction beyond the nominal Nyquist rate of the system. The model's predictions are compared to the predictions of the current standard FLIR92 model and measured laboratory results for two different staring focal plane array imagers. In both cases, the model's predictions match measured results more closely than the predictions of FLIR92.

TABLE OF CONTENTS

I. INTRODUCTION.....	1
A. REVIEW OF LITERATURE	1
B. OVERVIEW OF THESIS	2
C. THE THERMAL IMAGING PROCESS.....	3
D. SYSTEM PARAMETERS AND RESOLUTION.....	5
1. System Parameters and Definitions	6
2. Linear Systems Theory Applied to TIS	8
E. MODULATION TRANSFER FUNCTION.....	9
1. Optical Sub-system Transfer Function	11
2. Detector Sub-system Transfer Function	12
3. Electronics Sub-system Transfer Function	13
4. Display Sub-system Transfer Function.....	13
5. Other Transfer Functions	14
6. Net Transfer Function.....	15
7. Detector Sampling	15
F. SYSTEM PERFORMANCE FIGURES OF MERIT	17
1. NETD	18
2. MDTD and MRTD	19
G. MOTIVATION FOR THIS WORK	21
II. FIRST GENERATION MRTD MODELS	23
A. NIGHT VISION LABORATORY STATIC PERFORMANCE MODEL ..	24
B. THE LLOYD APPROXIMATE MODEL.....	28
C. FIRST GENERATION VISIBILITY MODEL.....	32
1. Visibility Model Origins.....	33
2. Contrast Transference Parameter	35
3. Low Frequency Threshold Contrast	36
4. Visibility Model MRTD	37
III. SECOND GENERATION MODELING TOPICS.....	39

A. THREE DIMENSIONAL NOISE EFFECTS	39
B. 3-D NOISE IN FLIR92	45
C. SAMPLING AND ALIASING	49
D. SAMPLE SCENE PHASING EFFECTS	57
E. CLOCK-OUT FREQUENCY CONVERSION EFFECTS	60
F. OTHER EFFECTS	64
IV. EXPERIMENTAL DESIGN AND MEASUREMENTS	67
A. EXPERIMENTAL SETUP	68
B. EXPERIMENTAL METHOD	70
C. SYSTEM PARAMETERS	72
1. AMBER System	72
2. Mitsubishi Electronics System	74
D. MRTD MEASUREMENT RESULTS	75
E. OBJECTIVE MRTD MEASUREMENTS	79
V. SECOND GENERATION VISIBILITY MODEL	83
A. VISMODII OVERVIEW	84
1. VISMODII Modeling Concepts	85
2. Second Generation Visibility Model Enhancements	87
3. VISMODII Programming and Logical Flow	88
B. CONTRAST TRANSFERANCE PARAMETER	91
1. MTF/PTF Analysis in VISMODII	92
2. Aliasing and Scene Phasing in VISMODII	95
3. Contrast Transference Parameter Calculation	95
C. THRESHOLD INPUT CONTRAST	98
1. Analysis for Subjective Minimum Threshold Contrast	99
2. Analysis for Objective Minimum Threshold Contrast	101
D. RESULTS	103
VI. DATA ANALYSIS AND CONCLUSIONS	105
A. COMPARISON OF PREDICTIVE RESULTS TO MEASUREMENT ...	105

B. EXPLORATION OF THE MODEL	108
C. CONCLUSIONS	113
D. DIRECTIONS FOR FURTHER RESEARCH	114
LIST OF REFERENCES	117
APPENDIX A. THERMAL IMAGING SYSTEM PARAMETERS	121
A. SAMPLE FIRST GENERATION SYSTEM	121
B. AMBER ENGINEERING MODEL AE4128	122
C. MITSUBISHI M500 THERMAL IMAGER	123
APPENDIX B. RATCHES/LLOYD CONVERSION FACTOR	125
APPENDIX C. FLIR92	129
A. MTF ANALYSIS	130
1. Pre-filter MTF	131
2. Temporal Post-filter	132
3. Spatial Post-filter	133
4. System MTF	135
B. SAMPLING EFFECTS	136
C. SYSTEM NOISE	136
D. MRTD PREDICTION	138
E. SYSTEM OUTPUT	138
APPENDIX D. LABORATORY MEASUREMENT RESULTS	141
APPENDIX E. MATLAB CODE	149
A. V2.M	149
B. EFFCNT.M	152
C. ALIAS.M	156
INITIAL DISTRIBUTION LIST	159

LIST OF FIGURES

Figure 1.1. The thermal imaging process	3
Figure 1.2. Cascade of sub-system transfer functions	10
Figure 1.3. Example of a cascaded system transfer function	17
Figure 1.4. Standard four-bar resolvability targets	21
Figure 2.1. MRTD prediction plots from three first generation models	28
Figure 2.2. Contrast degradation in the visibility model, after Ref. 9	34
Figure 2.3. Visibility model contrast transference parameter	36
Figure 3.1. Three dimensional noise directional coordinate axes	40
Figure 3.2. Spatial sampling by a rectangular detector array	51
Figure 3.3. Spatial domain sampling process, after Ref. 18	52
Figure 3.4. Spatial frequency domain representation, after Ref. 18	53
Figure 3.5. One dimensional representation of sampling process	54
Figure 3.6. Application of a wide bandwidth reconstruction filter	55
Figure 3.7. Resulting spectrum with aliased component	55
Figure 3.8. Two dimensional sampling array	58
Figure 3.9. Displaced sampling function in one dimension	59
Figure 3.10. Sampled target spectrum in spatial frequency domain	60
Figure 3.11. Two possible clock-out patterns for an FPA	61
Figure 4.1. Laboratory setup for MRTD measurements	68
Figure 4.2. Target apparatus	69
Figure 4.3. The AMBER Engineering AE4128 system	72
Figure 4.4. The Mitsubishi IR-M500 system	74
Figure 4.5. Average MRTD measurements for the AMBER system	77
Figure 4.6. Average MRTD measurements for the Mitsubishi system	77
Figure 4.7. Average MRTD results for the AMBER system, logarithmic scale	78
Figure 4.8. Average MRTD results for the Mitsubishi system, logarithmic scale	78
Figure 4.9. Automatic target recognition simulation setup	79
Figure 4.10. Measurement of SNR from oscilloscope data	80
Figure 4.11. Temperature difference vs. spatial frequency for constant SNR	81

Figure 4.12. SNR vs. spatial frequency for a constant temperature difference	82
Figure 4.13. Temperature difference vs. SNR for constant spatial frequency	82
Figure 5.1. Salient features of VISMODII	87
Figure 5.2. VISMODII logical diagram	90
Figure 5.3. Four bar target pattern ($f_x = 0.6$ cy/mrad)	91
Figure 5.4. Image formation filter for Mitsubishi system	93
Figure 5.5. Image reconstruction filter for Mitsubishi system	94
Figure 5.6. Filtered output target image, spatial frequency = 0.1 cy/mrad	96
Figure 5.7. Filtered output target image, spatial frequency = 1.1 cy/mrad	96
Figure 5.8. Contrast Transference parameter, Mitsubishi system	98
Figure 5.9. VISMODII predictions for Amber system MRTD	104
Figure 5.10. VISMODII predictions for Mitsubishi system MRTD	104
Figure 6.1. Amber system two dimensional MRTD predictions	106
Figure 6.2. Mitsubishi system two dimensional MRTD predictions	107
Figure 6.3. Amber system horizontal/vertical predictions	109
Figure 6.4. Mitsubishi system horizontal/vertical predictions	110
Figure 6.5. Mitsubishi system sample-scene phase effects	111
Figure 6.6. Mitsubishi system aliasing impact on predicted MRTD	111
Figure C.1. FLIR92 predicted MRTD for Amber system	139
Figure C.2. FLIR92 predicted MRTD for Mitsubishi system	140
Figure D.1. AMBER system, horizontal MRTD trials	143
Figure D.2. AMBER system, vertical MRTD trials	143
Figure D.3. Mitsubishi system, horizontal MRTD trials	146
Figure D.4. Mitsubishi system, vertical MRTD trials	146

LIST OF TABLES

TABLE 3.1. 3-D Noise Components	42
TABLE 3.2. MRTD equation parameters	46
TABLE 3.3. Eye/brain integration factors	48
TABLE 5.1. Subjective threshold input contrast	99
TABLE C.1. Pre-filter MTF's	131
TABLE C.2. Temporal Post-filter MTF's	133
TABLE C.3. Spatial Post-filter MTF's	134
TABLE C.4. Default scale factors for staring systems	137
TABLE C.5. Default scale factors for scanning systems	137
TABLE D.1. Amber system measured horizontal MRTD	141
TABLE D.2. Amber system measured vertical MRTD	142
TABLE D.3. Mitsubishi system measured horizontal MRTD	144
TABLE D.4. Mitsubishi system measured vertical MRTD	145
TABLE D.5. Constant SNR = 6.0	147
TABLE D.6. Constant delta T = 3.5 Celsius	147
TABLE D.7. Constant spatial frequency = 0.5 cy/mrad	148

LIST OF SYMBOLS, ACRONYMS AND/OR ABBREVIATIONS

α	detector horizontal angular subtense (mrad)
α_h	horizontal correlation factor
α_t	frame to frame correlation factor
α_v	vertical correlation factor
$\alpha(f_x)$	visibility model contrast transference parameter
β	detector vertical angular subtense (mrad)
χ	Lloyd to Ratches conversion factor
$\delta(x,y)$	delta function with magnitude 1.0 at $x=y=0$
$\delta(f_z)$	delta function with magnitude 1.0 at $f_z=0$
Δf_n	detector noise measurement bandwidth (Hz)
Δf_{tot}	visibility model actual system bandwidth (Hz)
Δf_{sys}	FLIR92 model system bandwidth (Hz)
Δm	detector active region dimension (mm)
Δs	detector pitch (mm)
ΔT	target to background temperature difference (C)
ΔT_{min}	minimum input contrast in visibility model (C)
ΔT_s	contrast degraded temperature difference (C)
ΔT_{sc}	minimum threshold resolvable contrast (C)
Δx	detector cell horizontal dimension (μm)
Δx_i	horizontal instantaneous field of view (mrad)
Δy	detector cell vertical dimension (μm)
Δy_i	vertical instantaneous field of view (mrad)
Δz	detector cell horizontal and/or vertical dimension (μm)
Γ	light level (mLamberts)
η_λ	Ratches temperature derivative of Planck function

η_{OSC} overscan efficiency
 λ wavelength (μm)
 λ_p wavelength of peak radiance (μm)
 Λ spatial sampling period (mrad)
 σ standard deviation
 σ_{alias} VISMODII alias noise term
 σ_g^2 blurred optics variance
 σ_{tvh} 3-D noise standard deviation in the subscripted direction
 σ_{total}^2 total 3D noise variance
 τ_a atmospheric transmittance
 τ_{cis} clock-out interval in-scan direction (sec)
 τ_{cos} clock-out interval out-scan direction (sec)
 τ_{cycle} clock-out interval for one cycle of bar pattern (sec)
 τ_d detector dwell time (sec)
 τ_o optical element transmittance
 Ω_h horizontal noise term in 3D noise analysis
 Ω_v vertical noise term in 3D noise analysis
 $\square MTF$ square wave response in Lloyd model
 $a(x,y)$ aliasing term in spatial domain
 $A(f_x, f_y)$ aliasing term in spatial frequency domain
 A_d detector area (μm^2)
 A_o optical aperture area (cm^2)
 ATR automatic target recognition
 b sampling function sample scene phasing displacement
 C_s numerical constant in MRT general form

CRT cathode ray tube
 D_o optical aperture diameter (cm)
 D^* specific detectivity ($\text{cm Hz}^{0.5}/\text{W}$)
 DOD department of defense
 $E_{t,v,h}$ eye/brain integration factor in the subscripted direction
 f spatial frequency (cy/mrad)
 f_c cutoff frequency
 f_{\max} maximum boost frequency
 f_N system Nyquist frequency
 f_0 electronics low-pass equivalent 3-dB frequency
 f_{ocal} optical focal length
 f_R reference filter 3-dB roll-off frequency
 f_{sz} sampling frequency in the z direction ($z = v$ or h)
 f_t temporal frequency (Hz)
 f_x horizontal spatial frequency (cy/mrad)
 f_y vertical spatial frequency (cy/mrad)
 F system f/number
 F_{dot} system frame rate (Hz)
 FFT fast Fourier transform
 FLIR92 NVESD 1992 thermal imaging system model
 FPA focal plane array
 h horizontal direction subscript
 $h_i(x,y)$ image formation impulse response
 $h_r(x,y)$ image reconstruction impulse response
 H_B boost sub-system MTF
 H_{det} detector spatial sub-system MTF

H_d	display sub-system MTF
H_{elect}	electronics sub-system MTF
H_{eye}	eye sub-system MTF
H_i	image formation MTF
H_L	FFT of one bar in long dimension
H_{LOS}	TIS vibration sub-system MTF
H_{NF}	FLIR92 noise MTF
H_{ogb}	optical geometric blur sub-system MTF
H_{opt}	optical sub-system MTF
H_{PRE}	pre-filter sub-system MTF
H_r	image reconstruction MTF
H_{ref}	Lloyd reference MTF
H_{SPF}	spatial post-filter sub-system MTF
H_{sys}	total system MTF
H_{TPF}	temporal post-filter sub-system MTF
H_W	FFT of one bar in the narrow dimension
H_λ	spectral radiance
$i(x,y)$	image output in spatial domain
$I(f_x,f_y)$	Fourier transform of $i(x,y)$
IFOV	instantaneous field of view
InSb	Indium Antimonide
k_z	MRTD directional correction factor in subscripted direction
K	boost parameter
L	length of one bar
LCD	liquid crystal display
LED	light emitting diode

m number of horizontal detector elements in an array
 M system magnification
 $MDT(D)$ minimum detectable temperature (difference)
 $MRT(D)$ minimum resolvable temperature (difference)
 $MRTD_L$ Lloyd model MRTD
 $MRTD_R$ Ratches model MRTD
 MTF modulation transfer function
 n number of vertical detector elements in an array
 N total number of detectors in an array
 N_λ target spectral radiant something or other
 $N_{t,v,h}$ 3D noise component in subscripted direction
 $NETD$ noise equivalent temperature difference
 $NVESD$ night vision and electronic sensors directorate
 NVL night vision laboratory
 $o(x,y)$ incident object function
 $O(f_x, f_y)$ Fourier transform of $o(x,y)$
 OTF optical transfer function
 $p(x,y)$ sampling function
 P device vibration variation factor
 P_λ spectral power received
 PC personal computer (IBM compatible)
 PSF point spread function
 PTF phase transfer function
 $PtSi$ Platinum Silicide
 q monitor factor
 Q Ratches term
 R observer to TIS distance

R_{λ} detector responsivity
 R_z FLIR92 spatial sampling rate (samples/mrad)
 $s(x,y)$ target scene input function
 S global data set average
 SNR signal to noise ratio
 SNR_{thr} threshold signal to noise ratio for resolution
 SPM static performance model
 t temporal direction subscript
 t_e eye integration time (sec)
 t_i detector integration time (sec)
 T temperature (K)
 $T_p(f)$ reconstructed output peak contrast in VISMODII (C)
 $T_t(f)$ reconstructed output trough contrast in VISMODII (C)
 TIS thermal imaging system
 U global data set magnitude
 v vertical direction subscript
 v scan velocity
 V_n noise voltage (V)
 V_s signal voltage (V)
 $VISMODII$. . second generation visibility model
 W width of one bar (cm)
 W_{λ} target spectral radiance per steradian
 x horizontal direction
 y vertical direction
 z horizontal or vertical as appropriate subscript
 Z instantaneous field of view in horizontal and vertical direction

ACKNOWLEDGMENT

This research has been supported by Naval Command and Control and Ocean Surveillance Center, NRaD, under NRaD project MPB45R5T25. The FLIR92 software and manuals were provided by the U.S. Army Night Vision Electronic Sensors Directorate. The support of both commands was appreciated.

I wish to acknowledge my thesis co-advisors, Professors Ron J. Pieper and Alfred W. Cooper, for their valuable help and insight in helping me in the research and writing of this thesis. I also wish to acknowledge the ECE curriculum office and the USMC representative office for their support. I also must thank Cem Koc, Turkish Navy, for his comradeship and support in the laboratory measurements.

I could not have completed this thesis without the patience and moral support of my wife, Jeanne, and the fun hours spent with my sons Joshua and Nicholas. I thank my family for always being there for me.

I. INTRODUCTION

A. REVIEW OF LITERATURE

The modeling of thermal imaging systems (TIS) in order to predict system performance has been of wide-spread interest since the 1970's. The figure of merit adopted by the early researchers in the field was the minimum resolvable temperature difference (MRTD). The earliest of predictive models followed a linear optical transfer function (OTF) analysis, and included standard probability theory in order to predict an output signal to noise ratio given TIS parameters [Refs. 1 through 7]. The early standard model was the U.S. Army Night Vision Laboratory (NVL) model, introduced in 1975. As the state of the art in TIS systems developed, shortcomings in the MRTD analysis were realized and explored, and alternative models were presented [Refs. 8 through 11].

Recently, the advent of widespread use of staring focal plane array (FPA) technology in TIS has required the predictive models to be revised yet again. The changes, and corresponding research efforts can be divided into several categories, including directional noise, aliasing, sample scene phasing and others. Directional noise modeling methods have been introduced to account for fixed pattern noise effects found in staring FPA device outputs [Refs. 12 through 15]. The U.S. Army Night Vision and Electronic Sensors Directorate (NVESD) released a new model called FLIR92 in 1992 that accounted for these directional noise effects [Ref. 16].

Unfortunately, the FLIR92 model did not address several outstanding second generation modeling concerns. Chief among these is the problem of aliasing caused by undersampling in the FPA [Refs. 17 through 25]. Other effects include nonlinear electronic processing, sample scene phasing, and image reconstruction effects; and the widespread incorporation of automatic target recognition (ATR) systems [Refs. 26 through 33]. Another consideration of TIS modeling is the proper treatment of the eye/brain recognition process, and the understanding of how the eye acts as an optical filter [Refs. 34 through 37]. These effects, among others, must be included in any complete predictive model.

B. OVERVIEW OF THESIS

This thesis has four main purposes. First, it is designed to serve as a stand-alone document describing the background of thermal imaging system (TIS) modeling development. Second, it includes a review and discussion of second generation modeling considerations and touches on the state of the art in TIS modeling. Third, and most importantly, the second generation modeling considerations explored are incorporated into an analytical model for the prediction of performance for staring focal plane array (FPA) thermal imagers. Finally, the thesis presents test data obtained in the laboratory and evaluates the performance of the predictive MRTD models.

Chapter I is an introduction to the thermal imaging process with a brief discussion of system parameters, modeling conventions, and associated concepts.

Chapter II provides historical context for second generation models by presenting established first generation models and concepts.

Chapter III discusses many of the concepts and issues of second generation TIS modeling, and methods of incorporating them into analytical models, using FLIR92 as an example.

Chapter IV is a description of the laboratory experiments conducted and the results obtained.

Chapter V describes the development of a second generation visibility model for TIS performance prediction, VISM0DII.

Chapter VI is a comparative analysis of modeled and experimental results, including conclusions and directions for further research.

Various appendices are also included that contain derivations, specifications, or data too lengthy or inconvenient to be included in the main manuscript.

C. THE THERMAL IMAGING PROCESS

Thermal imaging systems allow the utilization of middle and far infrared wavelength radiation for target detection and recognition. These systems, unlike visual or near infrared image intensification technologies, exploit the radiance of objects in the field of view; i.e., they do not require ambient reflected radiation. The spectral radiant emittance of an object in the field of view is given by Planck's blackbody radiation law, modified by the object's material properties. The wavelength of greatest radiant emittance in the object's radiative pattern is given by Wien's displacement law. The total radiance and peak wavelength of a target's radiative pattern are fundamentally determined by its temperature, modified by its physical characteristics (emissivity and reflectivity), and affected by the ambient radiance. The modified or 'apparent' temperature is often referred to as the 'radiation' temperature. For objects with radiation temperatures near 300K, the peak radiative wavelength occurs near $10\text{ }\mu\text{m}$, well above visible wavelengths. The ability of a TIS to display a visible image from this invisible and temperature-dependent radiation gives rise to the term 'thermal imager'.

A TIS can resolve a scene based on the radiation temperature differences among the objects in a scene, provided the electronic signal generated by the radiation detection process is large enough to overcome noise artifacts inherent in the TIS's several sub-systems. The thermal imaging process is best illustrated as a continuous sequence of events as portrayed in Fig. 1.1.

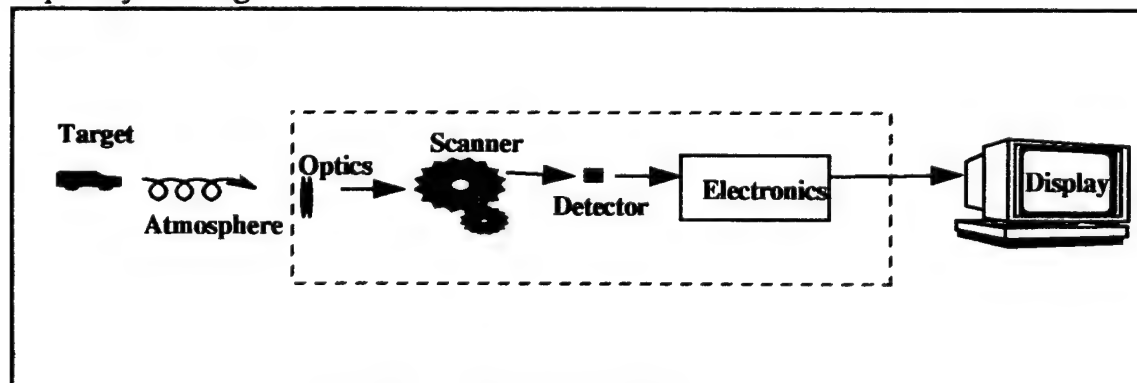


Figure 1.1. The thermal imaging process

The thermal imaging sequence begins with a scene, delimited by the projected field of view of the TIS detector element(s). The scene generally consists of a radiating target as well as the target's radiative environment. Due to radiation temperature differences between the target and this environment, the spectral radiance characteristics of each will differ. Notably, the target/background scene also contains reflections from other radiation sources in the wavelength band of interest. Most TIS are designed to operate in the 3-5 μm or 8-14 μm wavelength bands. These wavelength bands are near enough to the peak radiance of objects at 300 K (about 10 μm) to receive a significant portion of a target's radiation, and correspond to atmospheric transmission windows.

The radiation from the target/background scene passes through an intervening atmosphere to reach the TIS. The atmosphere has its own wavelength dependent scattering and absorption effects that are manifest on both the target and background radiation. For target detection and resolution applications in the field, this effect can be very significant. For resolvability tests conducted in a controlled laboratory environment, this effect is often considered to be identical on both the target and background radiation, and is often ignored.

Next, the scene radiation, modified by the atmosphere, reaches the TIS itself. The radiation is gathered and focused by a series of collecting optics and optical processing elements engineered to be transparent to the wavelength band of interest. In the focal plane of the processing optics is the detector element(s). Although the variety of detector element materials and configurations gives rise to a great number of TIS types, the function of the individual detector in each type is the same. This quantum device detects incoming photons of a specific band of wavelengths by converting the received photon energy into an electrical signal that is proportional to the photon flux received from a scene element. The wavelength band is determined by the energy band configuration of the semiconductor material from which the detector is made. The electrical signal from the detector(s) is then processed by the electrical system components. This processing typically includes temporal filtering, signal boosting, and AC-coupling to subtract common background signal levels. The output of the electrical processing sequence is, generally, a monochrome RS-170 analog video signal which is displayed by a standard television monitor. In some

cases, the output is a digital signal displayed on a computer monitor, often in pseudo-color. For most current systems, the human operator then processes the displayed image by his or her own visual and cognitive systems. In this case, the psycho-physical imaging process becomes an important part of system performance modeling. For many modern systems, however, an automatic target recognition (ATR) device takes the place of a human observer. A modern predictive performance model should also be able to incorporate these objective measurement devices.

D. SYSTEM PARAMETERS AND RESOLUTION

The great variety of detector types and configurations make it difficult to discuss thermal imaging modeling with any degree of generality. There are, however, two general categories used to describe classes of systems based on detector configuration. Those TIS labeled 'first generation' include those with a single detector or a one-dimensional array of detector elements. These systems have a scanning mechanism consisting of a set of rotating prisms or mirrors that sweeps the image over the detector(s). The speed and direction in which the scene is swept over the detector(s) defines the scene dissection into discrete elements, as well as the dwell time for which a given scene element will be focused on a detector. A second category of system uses a two-dimensional array of detectors that 'stare' at the scene with outputs clocked out at given intervals. No scanning mechanism is required for these 'second generation' systems, but their electronic complexity is correspondingly greater. The dwell time and scene dissection of staring type systems are determined by the detector element size and spacing, and the rate at which the outputs are clocked out. It should be noted that because focal plane array technology has not progressed as rapidly as expected, some systems exist that combine scanning with a smaller two dimensional array. These hybrid systems are also often referred to as 'second generation.' For the purposes of this thesis, 'second generation' refers to staring focal plane arrays; although many of the modeling topics treated here apply equally well to hybrid systems.

The 'first generation' of TIS is made up of many types of systems that share a common set of basic elements. Most of these basic elements are described in two early works in the field; the Night Vision Laboratory (NVL) Static Performance Model [Ref. 1], and a 1979 Navy Research Laboratory technical report describing the fundamentals of thermal imaging systems [Ref. 2]. Thermal imaging basics are also presented in an early text by J.M. Lloyd on the subject of thermal imaging systems [Ref. 3]. These early works and the basic system definitions they contain, are representative of the standard fundamentals that have been adopted by the thermal imaging community. Current research in 'second generation' modeling is based heavily on first generation principles, so these fundamentals are of continued relevance.

1. System Parameters and Definitions

Obviously, the image resulting from the entire thermal imaging process depends heavily on the parameters of the TIS system used. Of particular relevance to most TIS applications is the discrimination of a target signal against background clutter and system noise. From early research in television and motion picture standards, the task of discriminating an object from its background has been shown to depend on the signal to noise ratio (SNR) of the output of the system [Ref. 2, Chapter IV]. Since noise is interposed at every event in the thermal imaging sequence, the processing artifacts of each sub-system on both the target and noise signals are important. The radiation temperature difference between the target and the background required for detection or resolution by the TIS is dictated by the combination of these processing artifacts.

One aspect of the resolvability of a target is the 'thermal resolution' of the system. This parameter is determined by the material properties of the detector element(s). The spectral responsivity of a detector, $R(\lambda)$, is a measure of the output electrical signal level (in either volts or amperes) per watt of input radiative power:

$$R(\lambda) = \frac{V_s}{H_\lambda A_d} \left(\frac{\text{Volts}}{\text{Watt } \mu\text{m}} \right) \quad (1.1)$$

where V_s is the signal voltage output, H_λ is the incident spectral radiance, and A_d is the detector area [Ref. 3, Chapter 1]. A more useful detector parameter is the specific detectivity, D^* ("Dee star"). The D^* parameter is normalized to a unit detector area and a unit electrical bandwidth to give the electrical signal to rms noise ratio at the detector output. D^* is given by:

$$D^*(\lambda, f) = \frac{R(\lambda) \sqrt{A_d \Delta f_n}}{V_n} \quad (1.2)$$

where Δf_n is the detector noise measurement bandwidth, and V_n is the noise voltage output [Ref. 3, Chapter 1]. The electrical signal produced by both the target and the background radiation is generally large. Unfortunately, the important variation between the target signal and background levels is often orders of magnitude smaller. Since most TIS applications are concerned with resolvability, the contrast between signal and noise voltages is often enhanced by AC coupling the signals to remove the common DC component, thereby enhancing the thermal resolution.

In addition to the thermal resolution, the 'spatial resolution' is another important aspect of resolvability. This parameter is predominantly established by the angular field of view of the TIS as determined by the system optics, the detector response time, and the scanning frame rate. In second generation systems, the detector size and spacing, and the clock rate are significant in this regard. In some cases, it is limited by the pixel resolution of the display monitor. The field of view of the detector is the total background area subtended by the projection of the detector limits onto the target plane. The system parameters will determine how finely the scene is discretized, given that the entire scene must be scanned within one scanning period, or frame. The minimum spatial resolution is also influenced by the distance to the target and optical aperture size.

2. Linear Systems Theory Applied to TIS

The TIS response to various input signals can be described as a convolutionary process in either the temporal or spatial domain. This allows the application of linear systems theory to the problem of modeling a TIS, and predicting its thermal and spatial resolution capabilities. Linear system theory allows the prediction of the system's output as the sum of the system's total response acting on each point of the system input. This response is characterized by and commonly referred to as the 'impulse response' in electronics, or the 'point spread function' (PSF) in optics. These refer to the temporal or spatial domain spreading of a point source, or delta function, input to a sub-system. The Fourier transform of this response is defined to be the 'transfer function' of the sub-system. The assumptions made to accommodate the application of linear systems theory to TIS modeling are significant. In addition to the noncoherent detection of radiation, they include the linearity of signal processing, the uniformity of detector response, and the spatial invariance of the imaging process. Unfortunately, these conditions are routinely violated to some degree in practical TIS, posing great challenges to the system modeler. Of necessity, TIS are treated as linear over a restricted operating region to make mathematical analysis possible [Ref. 4]. A special caveat is in order here, as an analytical model is only as good as the assumptions made to develop it. It is inappropriate to blindly apply a model to a situation or application that does not fall strictly into the governing assumption set [Ref. 5]. This problem becomes quite clear in the application of linear models to sampled imaging systems as in Chapter III.

One mathematical tool of particular usefulness to the TIS modeler is the application of Fourier transform theory to the assumed convolutionary processes defined by the sub-systems. In the convolutionary process, the value of the output image distribution, $i(x,y)$, is found by summing the contributions of the system point spread function, $PSF(x,y)$, operating on each point of the incident object function $o(x,y)$:

$$i(x, y) = \int \int_{-\infty}^{\infty} o(\tau_1, \tau_2) PSF(x - \tau_1, y - \tau_2) d\tau_1 d\tau_2 \quad . \quad (1.3)$$

This is recognized as the two dimensional convolution of the object function with the system point spread function:

$$i(x, y) = o(x, y) \otimes \text{PSF}(x, y) . \quad (1.4)$$

The Fourier transform of the object function is defined as:

$$O(f_x, f_y) = \mathcal{F}\{o(x, y)\} = \int_{-\infty}^{\infty} \int_{-\infty}^{\infty} o(x, y) e^{-j2\pi(xf_x + yf_y)} dx dy . \quad (1.5)$$

Fourier analysis of the system allows the description of this series of convolutions as the cascade of a series of sub-system transfer functions operating on the spatial frequency and temporal frequency characteristics of the processed image (the Fourier transform operator will be given by the script F as in Eq. 1.5). The Fourier transform of the image distribution is given by the product of the Fourier transform of the object distribution and the Fourier transform of the system PSF. This last term is defined to be the optical transfer function (OTF) or system transfer function.

$$\mathcal{F}\{i(x, y)\} = \mathcal{F}\{o(x, y)\} \cdot \mathcal{F}\{\text{PSF}(x, y)\} , \quad (1.6)$$

and the image distribution at the output is found as:

$$i(x, y) = \mathcal{F}^{-1}\{I(f_x, f_y)\} . \quad (1.7)$$

Working with sub-system transfer functions is much simpler than evaluating multiple convolution integrals. Because basic system parameters define the system transfer function, the complete system response and overall noise levels are determined by the filtering properties of the optical, detector, electrical, and display sub-systems. For modeling efficiency, individual system parameters are often assigned to one of these four sub-systems, each having its own sub-system transfer function.

E. MODULATION TRANSFER FUNCTION

The system transfer function is determined by the cascade of the sub-system transfer functions. While working in the frequency domain, the sub-system transfer

functions can be multiplied together to produce a TIS 'system' optical transfer function (OTF). An OTF, by definition, is a complex quantity, having both magnitude and phase components. Since thermal imaging systems are non-coherent detection instruments, the phase information is typically not preserved. Phase information can become critical for defocused situations (e.g., an array with some elements out of focus). The electronic processing characteristics of the device may also include phase artifacts. The OTF is often treated as a magnitude transfer function only, referred to as the Modulation Transfer Function (MTF). In such analysis, a separate phase transfer function (PTF) can be included as necessary. The benefit in having a system-specific MTF is that it allows for analytical simulation and performance prediction for a given system under various target scene conditions. The performance of the system can be predicted by the action of the MTF on the spatial frequency composition of the input. Of course, the effects of the PTF must also be considered if they are significant. The cascade of sub-system transfer functions typical to most first generation models is shown in Fig. 1.2 [Ref. 3].

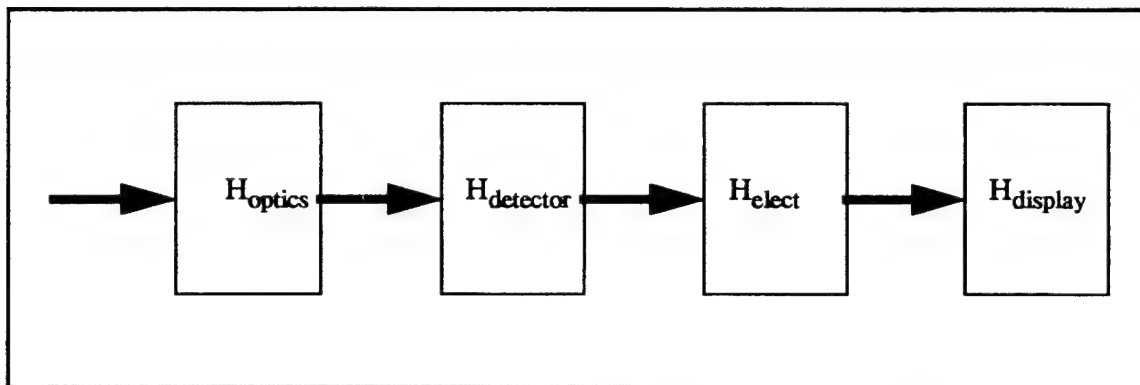


Figure 1.2. Cascade of sub-system transfer functions

To obtain this system MTF, it is necessary to first derive the individual sub-system transfer functions. The use of both spatial and temporal frequencies in the derivation is often confusing, as the electronic transfer function is usually given in Hz and the others are given in spatial frequencies of cy/mrad. The problem is usually circumvented by converting the electronic temporal frequency terms to their corresponding spatial

frequency. In first generation scanning systems, in the direction of scan, this simple conversion is given by:

$$f_x = \frac{\tau_d}{\alpha} f_t \quad (1.8)$$

where, f_x is the spatial frequency, f_t is the temporal or electrical frequency, α is the angular subtense of the system in the scanning direction, and τ_d is the dwell time of the image element on the detector element [Ref. 3, Eq. 5.57]. This simple relationship does not hold for staring systems, nor does it hold in the cross-scan direction. In a staring FPA, the electrical frequency corresponding to an input spatial frequency is a complicated function of the system clock-out pattern and rate. This is an important second generation effect that will be addressed in Chapter III. For consistency, all frequencies in the following analysis are spatial frequencies, typically given in cy/mrad.

Individual sub-system MTF's are taken from a variety of sources. They have their origin in optics, electronics, diffraction theory, television, and video standards. G. Holst has compiled an excellent treatment of the origins and specifics of many of the transfer functions used in TIS modeling [Ref. 5]. Some basic transfer functions are presented in the following paragraphs as examples. These are typical of those used by Ratches in the derivation of the NVL Static Performance Model [Ref. 1, Chapter 2], and by Lloyd in his approximation model [Ref. 3, Chapter 3]. Most of the first generation TIS models developed have used these or similar transfer functions. Second generation modeling has necessitated the formulation of updated models as discussed in subsequent chapters.

1. Optical Sub-system Transfer Function

The development of a generalized optical transfer function requires many assumptions about the system optics. Most TIS system optics are made up of circularly symmetrical elements. In a focused, diffraction-limited system, free of any major aberrations, the MTF is given by the autocorrelation of the pupil function of the optic

elements. Assuming a clear, circular aperture with uniform, monochromatic, planewave illumination, the MTF is given by:

$$H_{\text{opt}} = \frac{2}{\pi} \left\{ \arccos\left(\frac{f}{f_c}\right) - \left(\frac{f}{f_c}\right) \left[1 - \left(\frac{f}{f_c}\right)^2 \right]^{\frac{1}{2}} \right\} \quad (1.9)$$

where f is the spatial frequency in a one-dimensional analysis, or the root mean square of the two-dimensional frequency components in a two-dimensional analysis. Also, f_c , the optical cutoff frequency, is the ratio of D_0 , the effective aperture diameter, and λ , the incident wavelength. Spatial frequencies above the cutoff will be blurred by the system optics. This transfer function only applies to diffraction limited, incoherent, perfectly focused systems. Any aberrations in the optical elements will have a severe degrading effect, placing a high quality optics requirement on the design of TIS. It has been found that the above equation, evaluated at the midband wavelength, can be used to represent small wavelength band systems with no significant deviations [Ref. 3, Chapter 3].

2. Detector Sub-system Transfer Function

The detector itself will have two effects. It acts as both a temporal and spatial filter due to its finite dwell-time and finite area, respectively. If the detector dwell time, as controlled by the frame rate of the system, is long enough for the quantum processes to take place, we discount the quantum temporal filtering effect [Ref. 3, Chapter 3]. To determine the spatial transfer function due to the finite detector size, rectangular geometry is usually assumed. The transfer function is then given by the familiar 'Sinc' function in either the x or y directions:

$$H_{\text{det}} = \frac{\sin(\pi\alpha f_x)}{\pi\alpha f_x} \quad \text{or} \quad \frac{\sin(\pi\beta f_y)}{\pi\beta f_y} \quad (1.10)$$

where α is the horizontal angular subtense, and β is the vertical angular subtense of a detector. In the two dimensional MTF analysis, 'x' typically corresponds to the horizontal direction, and 'y' to the vertical.

3. Electronics Sub-system Transfer Function

Once the incident photon energy has been turned into an electrical signal by the detector(s), the signal is subject to the filtering effects of electronic processing. Fortunately, the electrical bandwidths of concern are usually much greater than the spatial bandwidth limits imposed by the other sub-systems. The net effect of the electronic component transfer functions cascaded together is usually taken to be that of an equivalent low-pass filter with system electronic transfer function given by:

$$H_{\text{elect}} = \left[1 + \left(\frac{f}{f_0} \right)^2 \right]^{-\frac{1}{2}} \quad (1.11)$$

where f_0 is the 3-dB bandwidth of the low-pass filter equivalent, converted to spatial frequency. This frequency is usually obtained by measurement of the impulse response of the system electronics. An electronics PTF is also often included [Ref. 3]. One possible formulation is:

$$\text{PTF}_{\text{elect}} = \text{atan}\left(-\frac{f}{f_0}\right) \quad (1.12)$$

4. Display Sub-system Transfer Function

The derivation of display system transfer functions is of extreme interest to television and video industries. A CRT display transfer function historically has been treated as a Gaussian spread function based on the pixel size, and can have severe phase artifacts when other than uni-directional scanning is used. The effective display transfer function is given by:

$$H_d = \exp(-qf^2) \quad (1.13)$$

where q is a monitor factor peculiar to a specific display device. The 'q' factor is obtained from the two dimensional optical spot size of an individual pixel in the display. By finding

the spot size of an equivalent Gaussian spread function that contains the same energy in a given radius as the original pixel spread function, and combining all constants into one term, the MTF can be given in this equivalent form. In the Lloyd model, the equivalence:

$$q = \pi \sigma_m^2 \quad (1.14)$$

is used [Ref. 3].

5. Other Transfer Functions

Other transfer functions may be cascaded with the net system transfer function if they represent an effect that has a significant impact on system performance. The incorporation of these additional transfer functions is not universal, and is model specific. Among them are transfer functions representing TIS motion, target motion, operator visual processes, system time constants, and other parameters. These additional effects are discussed at length in Holst [Ref. 5], and are included in most second generation models. The most contentious of these is the appropriate MTF to use to model the filtering characteristics of the eye/brain. This effect can be an important part of both the MTF analysis and the calculation of system bandwidths. There are several models postulated for this filtering effect. The first, and oldest, is a synchronous integrator model which treats the eye as a spatial and temporal integrator. The signal to noise analysis, then, is defined in terms of target area and time integrations [Ref. 2, Appendix D]. Other models use a matched filter approximation [Ref. 3]. In this case, the eye filtering effect is approximated by a filter matched to a single bar of the target. This has been demonstrated to be applicable to the eye/brain process over small areas [Ref. 3]. The NVL 1975 model is based on a matched filter concept. A third alternative is to treat the eye as a bandpass filter [Ref. 9]. This model assumes a normalized peak response to approximately 0.4 cy/mrad, followed by a decay associated with an optical transfer function based on the finite pupil size of the eye. This MTF treatment agrees well with measured human eye responses [Ref. 9]. In some second generation models, the eye is treated as a non-limiting MTF, essentially ignoring the filtering effect of the eye entirely [Ref. 16]. Some authors have

found that there is no difference in predicted performance whether the eye is treated as a synchronous integrator or a matched filter, and recommend the utilization of the simpler synchronous integrator model [Ref. 16]. Because of the wide disparity of opinion on this matter, even after years of research, it is desirable that a new predictive model make no particular assumptions about this response, thereby rendering the conflict strictly academic.

6. Net Transfer Function

The four main sub-system transfer functions and the resultant system MTF for the example first generation system presented in Appendix A are plotted in Fig. 1.3. As predicted by the central limit theorem, the cascade of the sub-system transfer functions yields a near Gaussian system transfer function [Ref. 6]. The addition of other transfer functions to the cascade increases this tendency toward the Gaussian. Note that the cascade does not incorporate any sampling effects as may be present in a two dimensional array.

7. Detector Sampling

At this point it is appropriate to discuss the dual nature of the detector effect on the displayed image. The effect of the detectors in an FPA is described as an 'averaging sampling' process instead of a 'window sampling' process [Ref. 3]. That is, the detector element of dimensions Δx and Δy averages the signal received over its finite active area, and accomplishes a sampling process due to the pitch between detectors. As shown below, an averaging sampling process is equivalent to convolving the image with the function described by the detector active area and then sampling by means of a multiplication by a delta function at the location of the detector element, $\delta(x,y)$ [Ref. 3, Chapter 9]. For a single detector located at (x,y) , the spatial output image produced by the detector is described by:

$$i(x, y) = \left[\frac{1}{\Delta x \Delta y} \int \int_{\text{area}} o(x, y) dx dy \right] \cdot \delta(x, y) \quad , \quad (1.15)$$

where $i(x,y)$ is the image function and $o(x,y)$ is the object function following the notation of Ref. 3. The term in brackets corresponds to the averaging effect of the detector element. Assuming rectangular geometry and recognizing that $\delta(x,y)$ has non-zero value only where x and y are both zero, the bracketed term may be expressed as:

$$[\text{""}] = \left[\frac{1}{\Delta x \Delta y} \iint_{\text{area}} o(\eta_1, \eta_2) \text{rect}\left(\frac{x-\eta_1}{\Delta x}\right) \text{rect}\left(\frac{y-\eta_2}{\Delta y}\right) d\eta_1 d\eta_2 \right] \quad (1.16)$$

which is recognizable as the convolution integral. If the conventional 'rect' function is used to describe the rectangular detector geometry ($\text{rect}(x/a, y/b) = 1$ for $-a/2 < x < a/2$, $-b/2 < y < b/2$, else $=0$) The output image becomes:

$$i(x, y) = \frac{1}{\Delta x \Delta y} \left[o(x, y) \otimes \text{rect}\left(\frac{y}{\Delta y}\right) \otimes \text{rect}\left(\frac{x}{\Delta x}\right) \right] \cdot \delta(x, y) \quad (1.17)$$

In the spatial frequency domain:

$$I(f_x, f_y) = [O(f_x, f_y) \cdot \text{sinc}(\Delta x f_x) \cdot \text{sinc}(\Delta y f_y)] \otimes \delta(n f_{sx}, m f_{sy}) \quad (1.18)$$

where the 'sinc' function is defined as the Fourier transform of the 'rect' function. The sampling delta functions are repeated at integer multiples of the sampling frequencies in both the horizontal, f_{sx} , and vertical, f_{sy} , direction. Equation 1.16 demonstrates an important but often overlooked point because it allows the detector spatial MTF to be considered separately from its position in the sampling array. This fact is used in VISMODII to separate the two effects. The term in the brackets, representing the averaging process that takes place over the active area of the detector, takes place in the spatial frequency domain by a normal MTF analysis. This justifies the appearance of the Fourier transforms of the detector shape in the cascaded transfer function.

Plotting the individual and total MTF's make it easy to spot limiting system parameters, and to identify possible design trade-offs. For quick analysis and 'back of the envelope' type calculations, the net transfer function can be replaced with a simple exponential [Ref. 3, p. 111]. The following approximation is often used:

$$H_{\text{sys}}(f) = \exp(-2\pi\sigma^2 f^2) \quad (1.19)$$

where σ is the standard deviation usually obtained graphically from plots similar to Fig. 1.3. This plot quite clearly indicates the progressive degradation of the system transfer function with increasing spatial frequency.

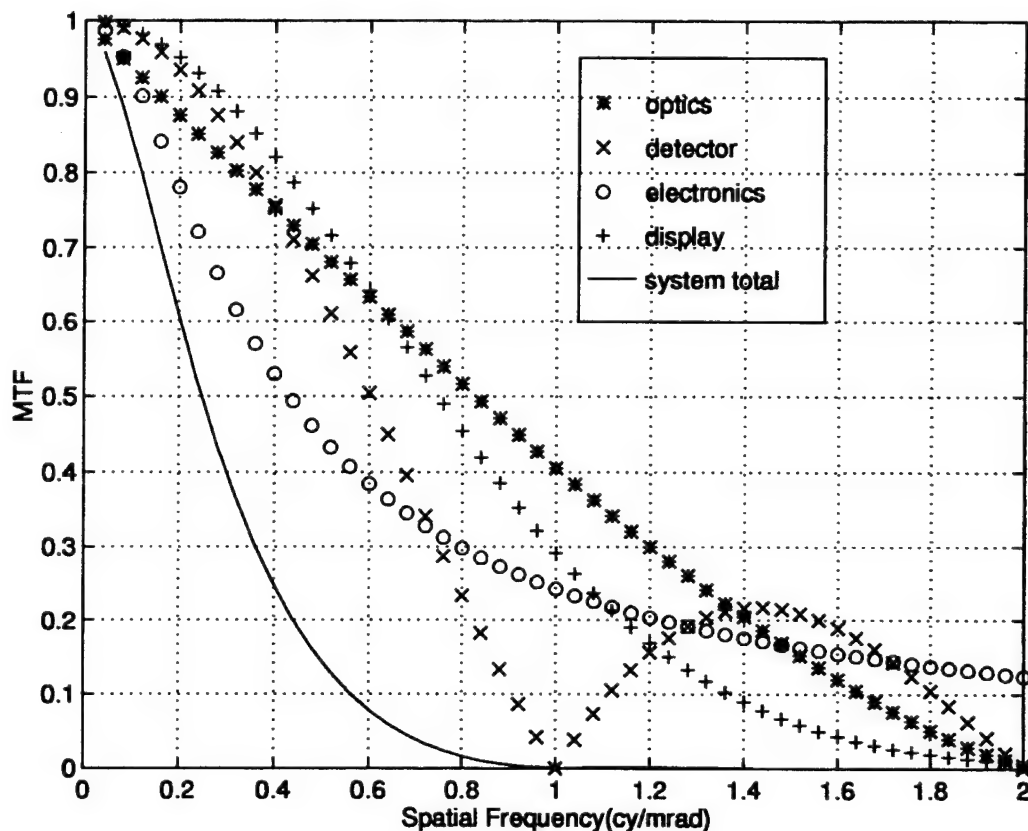


Figure 1.3. Example of a cascaded system transfer function

F. SYSTEM PERFORMANCE FIGURES OF MERIT

There are many system parameters from which the sub-system transfer functions are derived. However, the system transfer function by itself is not a reliable measure of system field performance because it does not include noise effects. Instead, the laboratory

performance of an imaging system is most often stated in terms of its target discrimination capabilities. The modeling of the thermal imaging process is an attempt to predict the ability of a system to provide the requisite degree of resolution for a particular application. Various levels of discrimination are possible, ranging from simple detection to unique target identification [Ref. 7, Chapter 2]. The degree of discrimination required is determined by the TIS application. Three commonly used figures of merit for TIS are based on the discrimination of the target signal from noise, and are derived from the electrical signal to noise ratio (SNR) of the system output. They are, the noise equivalent temperature difference (NETD), the minimum detectable temperature difference (MDTD), and the minimum resolvable temperature difference (MRTD).

1. NETD

Most figures of merit for a TIS are referred to the output signal compared to that of the output noise. Among these is the Noise Equivalent Temperature Difference (NETD). It is defined as the minimum temperature difference between a large black-body target and background that must exist for the output signal to noise ratio, taken just prior to the output display of the system, be equal to one; as measured with a standard reference filter [Ref. 7]. The noise equivalent temperature difference (NETD) for a typical TIS is given by:

$$\text{NETD} = \frac{\Delta T}{\left(\frac{V_s}{V_n} \right)} \quad (1.20)$$

where ΔT is the radiation temperature difference between target and background. When the ratio in the denominator is set to one (i.e. the signal to noise ratio) the temperature difference is defined to be the NETD. NETD derivation takes different forms for different authors, but all can be summarized as finding appropriate expressions for V_s and V_n , setting their ratio equal to one, and solving for the appropriate ΔT . The differences in the various formulations of the NETD are minor, but the assumptions that form the basis of the NETD are basically the same for all derivations. These assumptions include black-body radiation

sources, a standardized electronics transfer function, a large target, and a signal to noise ratio measured prior to the monitor display. The NETD, although valuable, has numerous deficiencies as a figure of merit [Refs. 1,3, and 7]. The fact that the measurement point does not include the display, exclusion of observer perception factors, and the use of a standard reference filter, limits its usefulness in modeling the resolution capability of a system. Nevertheless, the NETD can be a useful indicator of system performance, and is used as a building block to model more sophisticated figures of merit.

2. MDTD and MRTD

The shortcomings in the NETD model made it necessary to identify a better figure of merit. The figure of merit most popularly adopted by the community has been the MRTD and, less commonly, MDTD. These figures have the benefit of referring to the final image displayed by the TIS and interpreted by the observer. MDTD is defined as the minimum temperature difference required for a trained observer to be able to detect the presence of a large target in a displayed image. MRTD is defined as the minimum apparent temperature difference required between target and background in order for a user to resolve a standard four bar target pattern [Ref. 3, Chapter 5]. It is a unified system-observer performance criterion that goes beyond the electrical SNR used by the NETD. Since most military applications of TIS require the detection or resolution of objects in a scene based on the differences in their radiation temperatures, this is a valuable property. A strong correlation between field performance of a TIS and its MRTD has been demonstrated [Refs. 1 and 2]. Properly modeling the dependence of MRTD on spatial frequency and system parameters is a convenient way to evaluate and compare systems, and to predict their suitability for a given task.

The MRTD is measured in the laboratory as a function of the radian spatial frequency of a standard four-bar pattern, which consists of four vertical bars with height seven times their width, with spacing equal to the width of one bar, as pictured in Fig. 1.4. The fundamental spatial frequency (in cy/mrad) of the bar pattern is defined by the width

of a single bar, and the distance from the pattern to the observer. If the width of one bar is W (cm) and the observer distance is R (cm), then the fundamental spatial frequency is given by:

$$f_x = \frac{R}{2W} \left(\frac{\text{cy}}{\text{rad}} \right) = \frac{1 \times 10^3 R}{2W} \left(\frac{\text{cy}}{\text{mrad}} \right). \quad (1.21)$$

The standard four bar pattern currently used in TIS modeling is derived from an earlier three bar resolvability criterion developed for motion picture standards, and adapted to TIS [Ref. 3, Chapter 5]. The assumptions of black-body radiation, large target, and SNR measured prior to the display, still apply to MRTD modeling. In addition, the most common formulations of an MRTD model assume a finite eye-brain spatial integration period (typically about 0.2 seconds), a threshold signal to noise level for target detection (typically about 4.5), and a matched filter response by the eye of the observer [Refs. 1 and 3]. These assumptions are considered to be a minimum set required to approximate the eye's performance [Ref. 3, Chapter 5]. The derivation of an MRTD prediction model, like the NETD model, has taken several different forms since its acceptance as a figure of merit for TIS. Although each derivation has its own distinctive emphasis, the differences tend to be ones of definition and approximation. Three treatments of MRTD in first generation modeling will be presented in the next chapter. The motivation to use the MRTD instead of the NETD as a figure of merit arises because the MRTD includes the frequency dependent blurring effect of the TIS, as well as a link to a human resolvability criterion (Johnson criterion) [Refs. 5 and 7]. However, the MRTD still has some undesirable properties. Unfortunately, the inherent subjectivity of the resolvability criterion gives the MRTD a less than scientific characteristic. The subjectivity of the observer can be minimized through observer training, but the results are mostly unrepeatable, and differ among individual observers. The MRTD also suffers from other drawbacks that are especially relevant to second generation systems. As it is presently formulated, the MRTD cannot account for signal processing effects, image enhancement, image manipulation, and non-uniformity correction in detector arrays [Ref. 8]. Despite these drawbacks, the MRTD remains the principal figure of merit for laboratory performance of thermal imaging

systems. It will remain so until a satisfactory objective resolution figure of merit is adopted by the thermal imaging community.

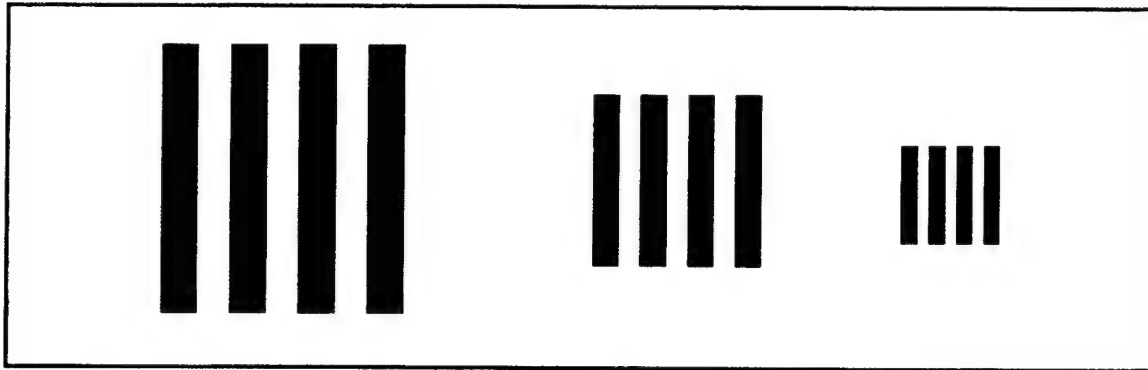


Figure 1.4. Standard four-bar resolvability targets

G. MOTIVATION FOR THIS WORK

For staring FPA based imagers, the principle of operation is significantly different than for first generation systems. Predictive models that have been introduced so far for second generation systems are typically extensions of first generation systems with a correction factor applied to account for directional noise effects. It has been suggested that these models are inadequate for predicting FPA based imager performance [Refs. 8,26, and 39]. FLIR92 is an excellent program to account for three dimensional noise effects, but it does not model sampling effects, and does not provide any evaluation data beyond the system Nyquist frequency. A new second generation model is required that can handle second generation systems that experience severe sampling and scene-phasing effects. This model should make no assumptions about the observation process, so that it can easily be extended to a TIS that uses an ATR device instead of a human observer. The model should extend performance prediction beyond the system Nyquist range. Finally, there is a dearth of published laboratory measurement data for TIS. It is necessary to make some MRTD measurements using the staring FPA systems available in order to better evaluate the performance of the various predictive models.

II. FIRST GENERATION MRTD MODELS

This chapter follows the historical development of TIS modeling, moving beyond basic system characterization to implementation in predictive modeling. An understanding of these older models is necessary in order to understand the second generation modeling refinements addressed in the remaining chapters. The first model considered, the Night Vision Laboratory (NVL) static performance model (SPM), also referred to as the 'Ratches' model for one of its principal authors, was first presented in 1975 [Ref. 1]. The Ratches model predicts NETD, MDTD, and MRTD for scanning thermal imaging systems. It is of particular significance because it was one of the first widely adopted analytical models for TIS performance prediction. The second model reviewed is the Lloyd model. The Lloyd model was similar to Ratches, but had the benefit of being much simplified through some basic assumptions. The Lloyd model also received widespread attention because of the popularity of Lloyd's text on the subject of TIS [Ref. 3]. These first two are considered established first generation reference models by the entire TIS community. Although somewhat dated, they serve as a point of departure for more modern second generation models. The treatment of these two models will be mercifully brief, providing only enough background to enable the reader to better understand the contents of later chapters. A third first generation model discussed is the 'visibility' model, presented in 1994 by R. Pieper and A. Cooper of the U.S. Naval Postgraduate School [Ref. 9]. The visibility method presented is a simplified MRTD prediction model based on a minimum threshold resolvable temperature difference specific to the TIS. This model has better correlation with measured MRTD data than the other two. Additionally, the visibility model serves as a basis for the new second generation visibility model, VISMODII, developed in Chapter V. Because the fundamental concepts of the visibility model apply to second generation modeling with equal validity, it will be treated in greater detail than the Ratches or Lloyd models.

A. NIGHT VISION LABORATORY STATIC PERFORMANCE MODEL

The Ratches model presented in 1975 was a defining work in the modeling community, and served as the standard MRTD prediction model for over a decade. It is also the foundation from which the currently popular FLIR 92, a second generation model, is derived. The Ratches model is a computer based model developed by the U.S. Army's Night Vision Laboratory for the development and evaluation of Army infrared systems for a variety of applications. It is a 'static' performance model since it does not consider target acquisition and positioning concerns for actual field systems. Instead, it was developed as an attempt to analytically predict system performance based on device parameters. One critical assumption of the Ratches model is that laboratory MRTD performance directly correlates with actual field performance [Ref. 1]. The Ratches derivation of MRTD follows the signal to noise ratio (SNR) analysis as described in Chapter I, using linear systems theory.

A key element in the Ratches model is the mathematical representation of the observation process, based on quantification of existing laboratory perception data [Ref. 1]. Ratches models the eye-brain process as a matched filter for a one bar pattern. This implies a hypothetical filtering of both signal and noise with a filter matched to one bar of the target pattern. The consequence of this modeling is the inclusion of two perceived signal-to-noise ratio improvements in the eye-brain process. The matched filter modeling and the finite integration time of the eye each results in improved resolvability performance, and is an important parameter for any TIS with a human observer in the loop. Another eye-brain process included is a perceived SNR threshold for resolution. Recall in the NETD derivation that the signal to noise ratio was set to one. The threshold value for resolution is actually postulated to be 2.25 by the Ratches model, corresponding to a probability of detection of 50 percent. [Ref. 1]

The noise characteristics of the Ratches model are completely specified by the NETD. The Ratches model uses the following formulation for NETD:

$$\text{NETD} = \frac{4F^2(\Delta f_n)^{\frac{1}{2}}}{\pi A_d^{\frac{1}{2}} \tau_a \tau_0 \sqrt{N} \int_{\Delta\lambda} D^*(\lambda) \eta_\lambda d\lambda} [\text{Kelvin}] , \quad (2.1)$$

where F is the system 'F' number (the ratio of focal length to optics diameter), Δf_n is the noise bandwidth, A_d is the detector area, τ_0 is the optics transmission factor, τ_a is the atmospheric transmission factor, N is the number of detectors, and the integral term represents the response of the detector to the incremental change in target radiance for an incremental change in temperature [Ref. 1, Eq. 24]. The η_λ term is a shorthand notation used by Ratches to represent the temperature derivative of the Planck radiation function [Ref. 1, p.12]. An important feature of the NETD derivation is the calculation of a noise bandwidth to be used. In the Ratches model, this bandwidth is fundamentally determined by the measurement filter. The NETD derivation assumes that the filtering action of the electronics prior to measurement conforms to the standard low-pass filter given as Eq. 1.11. If the detector noise can be considered white, then the noise bandwidth is taken to be:

$$\Delta f_n = \frac{\pi}{2} \left(\frac{1}{2\tau_d} \right) \quad (2.2)$$

with τ_d given as the dwell time of the detector [Ref. 1, Eq. 22]. (This does not refer to the 'clock-out' time of a staring array that will be discussed in Chapter III. The detector dwell time is the time for which a given detector element is illuminated by a given scene element. One of the great advantages of staring arrays is that the dwell time is greatly increased, thereby reducing the noise bandwidth.) The Ratches model assumes no sampling artifacts in the scan direction, a subject of great interest in second generation modeling.

The sub-system transfer functions used in the Ratches model were presented in Chapter I. In addition to the cascade of four basic sub-system transfer functions previously described, Ratches includes three additional sub-system transfer functions in the cascaded system MTF. These MTF's are stated here, without derivation, for completeness only. The reader should refer to Ref. 1 if more detail is required. (In the cascade analysis that

follows, the value of these additional factors will be set to '1'.) The first is a transfer function of the eye:

$$H_{\text{eye}} = e^{\frac{-\Gamma f}{M}} \quad (2.3)$$

where the eye MTF exists in both the x and y directions, and Γ and M are light level and magnification parameters respectively [Ref. 1, Eq. 20]. Second, the Ratches model adds a stabilization MTF to account for vibrations in the TIS device:

$$H_{\text{LOS}} = e^{-Pf^2} \quad (2.4)$$

where P is calculated from the variance of device vibration [Ref. 1, Eq. 19]. Third, Ratches includes an electronic boost MTF for systems so configured. The sub-system transfer function is given by:

$$H_B = 1 + \frac{(K - 1)}{2} \left[1 - \cos\left(\pi \frac{f}{f_{\text{max}}}\right) \right] \quad (2.5)$$

where K and f_{max} determine the amplitude and frequency of boost, converted to the appropriate spatial frequency values [Ref. 1, Eq. 16].

The overall system MTF including these additional factors is calculated to predict the signal transfer characteristics of the entire system for spatial frequency components in the horizontal and vertical directions. Horizontal spatial frequency is typically given by f_x , and the vertical by f_y . In the first generation, the horizontal MRTD, corresponding to the spatial frequency established horizontally by the bars in the pattern, was the dominant concern. The overall system MTF's (setting the additional MTF's equal to 1.0) are represented as:

$$H_{\text{sys}}(f_x) = H_{\text{opt}} H_{\text{det}} H_{\text{elec}} H_d \quad (2.6)$$

and,

$$H_{\text{sys}}(f_y) = H_{\text{opt}} H_{\text{det}} H_d \quad (2.7)$$

Ratches formulates the horizontal MRTD from the calculated NETD and MTF as given in Eq. 2.1 and Eq. 2.6. MRTD as a function of spatial frequency is predicted from device parameters. Several formulations of the MRTD are given by Ratches, with the most general form being:

$$\text{MRTD}_R = \frac{\left(\frac{\pi}{8}\right)^2 \text{SNR}_{\text{thr}} \text{NETD}}{H_{\text{sys}}(f_x) L \int_{-\infty}^{\infty} H_L^2 H_{\text{sys}}^2 df_y} \left[\frac{\Delta y_i v}{\Delta f_n F_{\text{dot}} t_e} \int_{-\infty}^{\infty} \int_0^{\infty} \frac{S(f_x)}{S(f_{ox})} H_{\text{elect}}^2 H_{\text{sys}}^2 H_L^2 H_W^2 H_d^2 df_x df_y \right]^{0.5} \quad (2.8)$$

[Ref. 1, Eq. A45]. The variables in the above equation include the threshold signal to noise ratio, SNR_{thr} ; the vertical instantaneous field of view in mrad, Δy_i ; the scan velocity, v ; the frame rate, F_{dot} ; and the eye integration time, t_e . Also, H_L and H_W refer to the Fourier transform of a single bar in the long and short dimension respectively. This formulation of MRTD assumes the bar pattern can be treated as a periodic function in the horizontal direction, and that the signal is obtained by taking the difference between the output of the matched filter when centered over the displayed bars and when centered over the background [Ref. 10, p. 21]. Note that this is a horizontal MRTD. An unvalidated vertical MRTD is also included in the Ratches model [Ref. 1, p. 13]. When plotted for the sample first generation system given in Appendix A, the MRTD prediction curve given by Ratches looks like Fig. 2.1, where it is shown plotted with the Lloyd and visibility model prediction curves. The plots are made on a log scale to better show the differences between the predictions of the three models. The Ratches model gives MRTD predictions that match measured data quite reasonably except for being consistently too pessimistic at low spatial frequencies, and too optimistic at high frequencies.

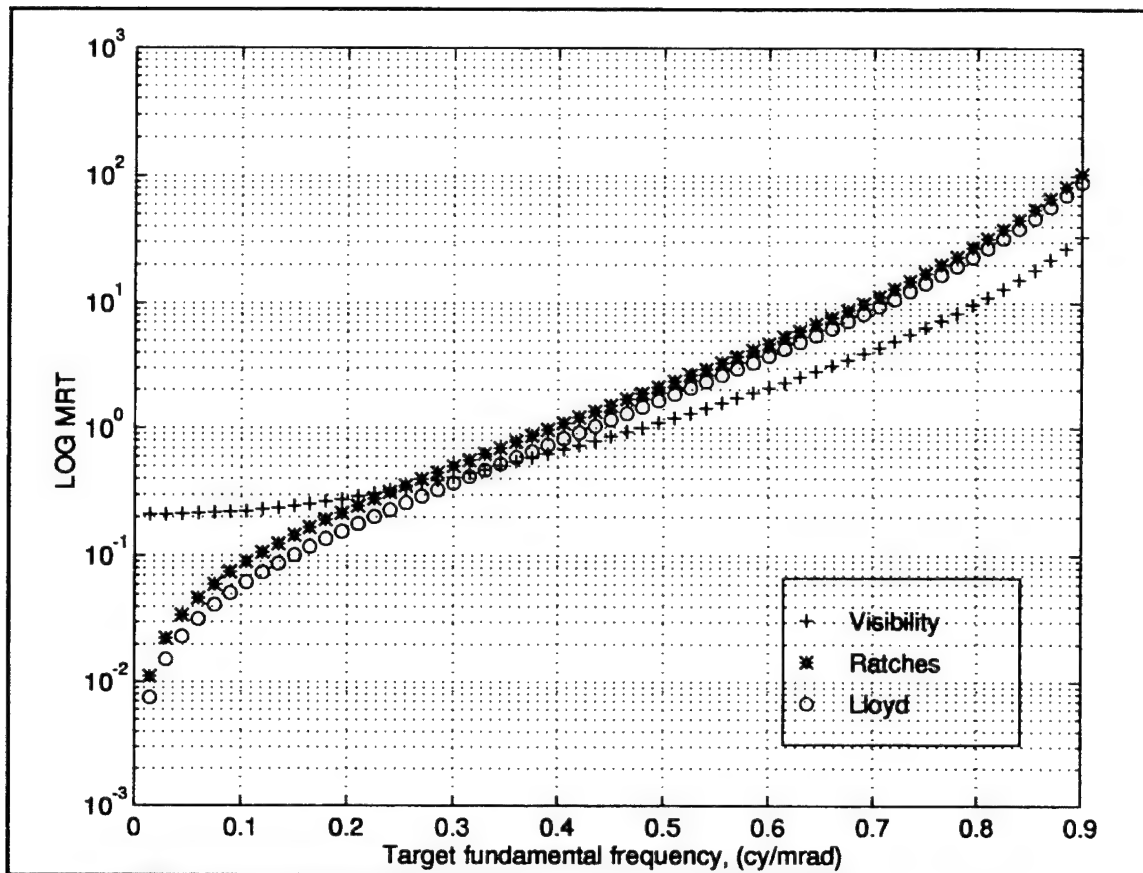


Figure 2.1. MRTD prediction plots from three first generation models

B. THE LLOYD APPROXIMATE MODEL

Lloyd's model for MRTD prediction [Ref. 3, Chapter 5] appeared near the same time that the Ratches model was introduced. Since Lloyd's text served as the main primer for TIS education for many years, his formulation for MRTD remains popular. As with the Ratches model, understanding of the Lloyd model for MRTD prediction requires an understanding of his treatment of noise and the human observer.

Lloyd's definition of NETD is the same as Ratches, but the formulation he uses is different. Lloyd, like Ratches, uses the standard reference filter to define the noise bandwidth of the system:

$$\text{MTF}_{\text{ref}} = \left[1 + \left(\frac{f}{f_R} \right)^2 \right]^{-0.5} \quad (2.9)$$

where,

$$f_R = \frac{1}{2\tau_d}. \quad (2.10)$$

This allows all video output noise to be directly related to the detector, and assumes that no other electronic processing noise is introduced. Atmospheric effects are assumed to be negligible since they operate on both the target and background radiation. Some highlights of Lloyd's derivation are given below to give the reader a sense of the origin of his results. [Ref. 3]

Starting with the spectral radiance received from the target:

$$N_\lambda = \frac{W_\lambda}{\pi} \left(\frac{W}{\text{cm}^2 \mu\text{msr}} \right), \quad (2.11)$$

it is a quick jump to the differential power received at the detector for a differential change in temperature:

$$\frac{\partial P_\lambda}{\partial T} = \alpha \frac{\beta}{\pi} A_o \tau_o(\lambda) \frac{\partial W}{\partial T} \left(\frac{W}{\mu\text{m}^2 \text{K}} \right). \quad (2.12)$$

Including the detectivity to convert this incremental power to signal voltage, and including a system optics transmission parameter, τ_o , gives:

$$\text{NETD} = \frac{\pi \sqrt{A_d \Delta f_n}}{\lambda_2} \quad (2.13)$$

$$\alpha \beta A_o \tau_o D^*(\lambda_p) \int_{\lambda_1}^{\lambda_2} \frac{d}{dT} W(\lambda, T_B) \frac{D^*(\lambda)}{D^*(\lambda_p)} d\lambda$$

where NETD corresponds to a signal to noise ratio of one in the small signal approximation [Ref. 3, Eq. 5.19]. In this case, α and β are the angular subtenses of the detector, and W is the spectral radiance at the detector. This can be shown to be equivalent to Ratches' formulation given as Eq. 2.1 if it is recognized that the F number of a system is the ratio of

the system focal length to the collecting aperture diameter, and that the field of view may be written as,

$$\alpha\beta = \frac{A_d}{F^2}. \quad (2.14)$$

Armed with an equivalent formulation for the NETD, Lloyd proceeds with the derivation of MRTD. Like Ratches, Lloyd seeks to obtain a predictive model which includes all elements of the TIS-observer system. Although noting the many possible considerations that could impact image quality (e.g., random noise, clutter, detector nonuniformities, contrast, among others) Lloyd emphasizes the dominant effect of spatial and thermal resolution on TIS performance. Lloyd assumes both a temporal integration time for the observer eye as 0.2 s, and a matched filter modeling of the eye [Ref. 3, p.183].

A unique characteristic of the Lloyd derivation is the consideration of the system response to a square wave input, as represented by the bar pattern in the scan direction. Lloyd notes that the square wave can be represented as the sum of a Fourier series of components containing the odd harmonics of the square wave fundamental frequency, and argues that the higher harmonics of this series will be removed due to the filtering action of the system MTF. This will leave only the scaled fundamental sinusoidal component. Substituting, the system response to the square wave can be replaced by the system response to the scaled first sinusoidal harmonic:

$$\square H_{\text{sys}}(f) = \frac{4}{\pi} H_{\text{sys}}(f), \quad (2.15)$$

where $\square H_{\text{sys}}(f)$ is the system square wave response, and $H_{\text{sys}}(f)$ is the normal system sinusoidal response.

In addition to the standard SNR derivation, Lloyd includes four SNR improvements he terms 'perception factors' [Ref. 3, p.186]. First, he notes an averaging effect of the eye on the signal received. This results in an SNR improvement by a factor of $2/\pi$. Second, he notes an SNR improvement of $(t_e F_{\text{dot}})^{-5}$ due to temporal integration by the eye. Third, he

notes a vertical integration along the bars of the target giving another perceived SNR improvement of $[7/(2 f_x \beta)]^{0.5}$. Finally, he replaces the noise bandwidth of the standard filter with one accounting for the eye's matched filter action. Setting the new and improved perceived SNR equal to the SNR threshold required for resolution (Lloyd uses 4.5, corresponding to a detection probability of 90%) and combining the perception factor constants, gives:

$$\text{MRTD}_L(f) = \frac{0.66(\text{SNR}_{\text{thr}})(\text{NETD})(f)}{(\Delta f_n)^{0.5} \text{MTF}(f)} \left(\frac{\alpha \beta}{F_{\text{dot}} t_e \tau_d} \right)^{0.5} \quad (2.16)$$

which is equivalent to Ref. 3, Eq. 5.58. As seen in Fig. 2.1, Lloyd's predicted MRTD curve for a sample system has the same shape as the Ratches model curve.

It can be shown that the Lloyd and Ratches models can be related by a frequency dependent conversion factor [Ref. 9]. This factor is obtained by taking the ratio of the two formulations for MRTD, cancelling like terms, and by applying a few low frequency assumptions given in the Ratches model. The derivation of this conversion factor is contained in Appendix B. The final conversion factor is repeated here for reader convenience:

$$\chi(f_x) = \frac{\left[2WL \int_0^\infty H_{\text{elect}}^2 H_W^2 H_d^2 df_x \right]^{0.5}}{L \int_{-\infty}^\infty H_L^2 H_{\text{sys}}^2 df_y}, \quad (2.17)$$

where H_W and H_L are the Fourier transforms of a single bar in the x and y-directions respectively, and L is the vertical dimension of the bar [Ref. 9, Eq. c2]. If the low frequency approximations for low spatial frequencies are applied, this conversion factor goes to one in the low frequency limit [Ref. 1]. This indicates that the Lloyd and Ratches models converge in the low frequency limit. This is also apparent from Fig. 2.1.

C. FIRST GENERATION VISIBILITY MODEL

In spite of the success of both the Ratches model and the Lloyd model, there are notable discrepancies between the MRTD performance that these models predict and actual measured performance. In particular, these models tend to be too optimistic at low spatial frequencies, and too pessimistic at high spatial frequencies. The low frequency trend is particularly disturbing in the limit as the spatial frequency goes to zero. As the target spatial frequency approaches this low frequency limit, the Ratches and Lloyd models both indicate that the expected MRTD would go to zero as well. Clearly, this is counterintuitive, as one would expect a threshold contrast to exist, below which the TIS could not resolve a target. Measured laboratory data also indicates that some threshold level of thermal contrast for perception exists. In addition, the subjectivity of the MRTD measurement process is disturbing. This subjectivity and non-repeatability are the result of the difficulties inherent in including human observers in the loop and modeling the resolution process of the eye-brain. [Ref. 9]

It was also important that an objective MRTD prediction model be derived to support an objective resolvability standard, such as would be required by an automatic target recognition device (ATR). The models in existence prior to the development of the visibility model were inseparably tied to the recognition process of a human observer. As the state of the art of thermal image processing continues to evolve, the human observer's tasks of detecting, resolving, or identifying a target are rapidly being replaced with automatic detection algorithms. The visibility model described is a first generation effort to address these concerns. The visibility model provides a simpler development for MRTD prediction based on a critical system response, and a degraded contrast transference due to spatial frequency limitations of the sub-systems, rather than a subjective 'perceived SNR' criterion. The concept of using a contrast transference instead of a strict MTF analysis is not unique to the visibility model [Ref. 11]. The fundamental arguments that support the

first generation visibility model apply equally well to second generation systems, and are used in the second generation visibility model as well.

1. Visibility Model Origins

In previous first generation models, MRTD performance was modeled as the attainment of a threshold signal to noise ratio. Generally, these derivations first developed the NETD required to achieve an SNR of one from system parameters. Next, the NETD was modified by SNR degradation and improvement factors that corresponded to the particular method used to model the recognition process. Some of these SNR modifications were dependent on the spatial frequency of the four bar pattern, others were not. This suggests a form for the MRTD that can be separated into two factors, one frequency dependent, the other not. The frequency dependent term would be derived from the sub-system MTF's and PTF's. The other term would be a constant for a particular system, and would account for noise performance, eye-brain signal enhancements, and all other factors independent of the target spatial frequency. The second term would represent the MRTD for the system in the low frequency limit. The representation used in the visibility model is:

$$\text{MRTD}(f_x) = [\text{MRTD}(f_x \rightarrow 0)][1/(\alpha(f_x))] \quad (2.18)$$

where the $\alpha(f_x)$ term is a contrast transference parameter that depends on spatial frequency, presumably obtainable from sub-system parameters or by direct measurement. The low frequency limit of the MRTD corresponds to a minimum system-degraded temperature difference that could be recognized by the sensor/observer [Ref. 9]. This representation has intuitive appeal because the MRTD would go to a minimum (non-zero) threshold value in the low frequency limit. Note that this is consistent with, but different from the approach espoused by the Ratches and Lloyd models. The MRTD performance of the TIS can then be obtained from the two factors alone, one of which is a constant. Once the contrast transference parameter is known, either through measurement or calculation, the MRTD is

easily obtained. The low frequency limit term incorporates the eye-brain recognition process, without making any particular assumptions about its nature. It simply represents the input temperature corresponding to the minimum degraded contrast that can be detected for a given system in the low frequency limit where the bar pattern appears as a simple step function. The minimum degraded contrast that can be detected by an ATR device can be a complex function of the device's signal processing characteristics and sensitivity. The definition of the threshold contrast makes no assumptions about either the recognition or the noise processes, nor even the observer. As such, it is consistent with an objective or 'machine' measured MRTD. It has the additional virtue of being simple to understand and to implement. To implement the visibility concept it is necessary only to find the low frequency threshold term, and model the frequency dependent contrast reduction induced by the system. Figure 2.2 portrays the salient features of the visibility model.

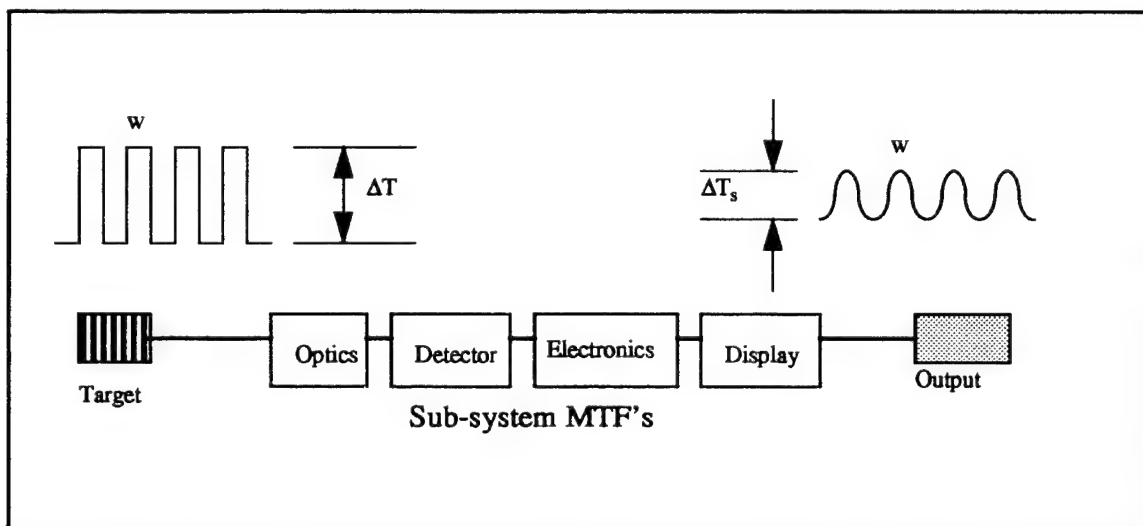


Figure 2.2. Contrast degradation in the visibility model, after Ref. 9

Figure 2.2 clearly demonstrates the visibility model concept of a system degraded contrast transference. The four bar pattern input signal is characterized by the temperature difference between target and background, portrayed as ΔT . This signal is degraded and filtered by the frequency dependent characteristics of the various sub-systems (i.e., transfer

functions). When the image is displayed at the output, the bar pattern still displays the same fundamental frequency corresponding to the bar width, w , but the higher harmonics of the square wave input have been filtered out. The contrast in the output, defined as the dynamic range of the signal, has been reduced to ΔT_s . The premise of the visibility model is that only two parameters are necessary to predict the MRTD for the system. First, the contrast transference parameter as a function of spatial frequency must be calculated from the square wave response of the system. Second, the minimum threshold resolvable contrast in the output must be determined.

2. Contrast Transference Parameter

The frequency dependent contrast transference parameter, as implied by Fig. 2.2, is a function of the sub-system MTF's. The four bar target source is treated as a square wave with amplitude determined by the radiation temperature difference between background and foreground temperature, ΔT . This incident square wave can be represented by a Fourier series of sinusoidal components of amplitude-scaled odd harmonics based on the radian spatial frequency of the bar pattern. It is apparent that the filtering effect of the sub-system transfer functions will eliminate or degrade some or all of the components of the original square wave. As a result, the measured output signal, ΔT_s , will have a reduced dynamic range. For example, Fig. 2.2 shows that all frequency components greater than the fundamental frequency have been filtered out. The result is a contrast reduction in the output. The ratio of the output contrast to the input contrast is defined as:

$$\alpha(f_x) = \frac{\Delta T_s(f)}{\Delta T} \quad (2.19)$$

The $\alpha(f_x)$ parameter is a function of spatial frequency, and relates input to output dynamic range (contrast). In the visibility model, this parameter is obtained by calculating the square wave response of the system using Fourier construction. The parameter is

calculated as the ratio of contrast found in the output signal to that of the input square wave at a particular frequency. In the visibility model, this parameter was evaluated with and without phase artifacts, with the interesting result that MRTD prediction was not affected by the inclusion of the PTF portion of the system OTF. A plot of $\alpha(f_x)$ for the sample system given in Appendix A is plotted in Fig. 2.3.

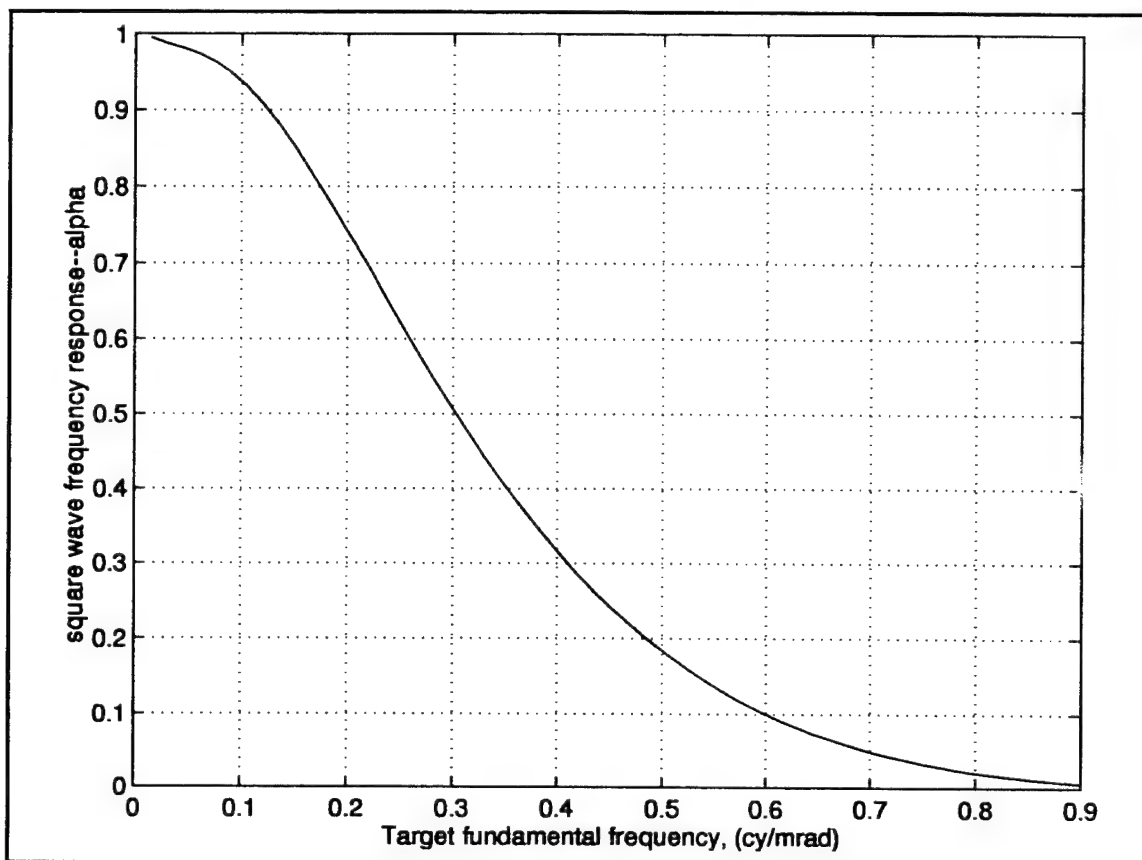


Figure 2.3. Visibility model contrast transference parameter

3. Low Frequency Threshold Contrast

A key assumption of the visibility model is that there is a critical minimum threshold of ΔT_s that can be recognized; either by an ATR device or a human observer. If the expression in Eq. 2.19 is evaluated in the low frequency limit, the threshold output contrast, ΔT_{sc} , and the corresponding input temperature difference, ΔT_{min} , can be found:

$$\Delta T_{sc} = \Delta T_{min} \cdot \alpha(f_x = 0) \quad (2.20)$$

This represents the minimum degraded contrast in the output signal that can be resolved. The bar pattern, in the low frequency limit, is treated as a step function. The great advantage of the visibility model is that the threshold output contrast does not make any assumptions about the observer. A given system could have one threshold value for a human observer, and another for an ATR device. The visibility model, then, could be useful in the formulation of an objective measure that replaces the MRTD. A heuristic treatment for finding the critical temperature, ΔT_{sc} , is presented in the visibility model. The proposed expression is:

$$\Delta T_{sc} = \text{SNR}_{thr} \text{NETD} \left[\frac{\Delta f_{TOT}}{\Delta f_n(t_e F_{dot})} \right]^{0.5} \quad (2.21)$$

where Δf_{TOT} effectively adjusts the bandwidth used in the NETD to a true system bandwidth rather than a bandwidth based on a reference filter [Ref. 9, Eq. 7]. The true system bandwidth is given by:

$$\Delta f_{TOT} = \int_0^{\infty} H_{elect}^2 H_d^2 H_{eye}^2 df \quad (2.22)$$

where the MTF's that determine the true system bandwidth are all of the post-detector subsystem MTF's. This formulation could include a more detailed or a greater number of subsystem MTF's, but this would not affect the salient features of the visibility model. This parameter could likewise be determined by direct measurement using a human or ATR observer.

4. Visibility Model MRTD

The spatial frequency dependent MRTD curve is easily obtained for the visibility model by recognizing that ΔT_{min} used in Eq. 2.20 corresponds to the MRTD. The MRTD is then given by:

$$\text{MRTD}(f_x) = \frac{\Delta T_{sc}}{\alpha(f_x)} \quad (2.23)$$

The low frequency limit of MRTD now corresponds to the minimum threshold system degraded contrast observable. The only information required to obtain the MRTD are the ΔT_{sc} and the $\alpha(f_x)$ term. Figure 2.1 shows that the low and high frequency trends for the visibility model are different from the MRTD prediction curves for the Ratches and Lloyd models. In these cases, the visibility model appears to correlate better with measured laboratory results [Ref. 9]. The MRTD results of the visibility model do not go to zero in the low frequency limit, nor do they require the addition of an artificial correction term. Since no explicit assumptions regarding the nature of the observer or observation process have been made, the visibility model MRTD formulation shows great potential as an objective MRTD framework. Likewise, since no explicit assumptions are made as to the type of TIS employed, the visibility model concepts should apply equally well to second generation systems. The application of these concepts to second generation modeling is presented in Chapter V, following a discussion of some other second generation modeling concepts.

III. SECOND GENERATION MODELING TOPICS

The development of second generation thermal imaging system technology, especially the widespread utilization of focal plane arrays (FPA's) has changed the requirements for complete system modeling. This chapter is a review of many of the modeling artifacts that must be included in order to predict the performance of second generation systems. The development of these modeling concepts and the efforts to quantify their effects represent the state of the art in thermal imaging system modeling development. The specific second generation topics covered in detail include; three dimensional noise analysis, sampling, aliasing, sample scene phasing, and clock-out frequency conversion. Other effects are discussed qualitatively in the last section of this chapter.

A. THREE DIMENSIONAL NOISE EFFECTS

The advent of the second generation of thermal imaging systems has necessarily changed the way noise is modeled in these systems. First generation systems were typically dominated by detector noise. Detector noise was modeled as a white noise process and quantified by the NETD [Ref. 1]. The NETD is inadequate for modeling second generation systems for a number of reasons [Refs. 12, 13, and 14]. As explained in Chapter I, the NETD measurement requires a standard reference filter to simulate the post-electronics system processing. This is not applicable to second generation systems in which data from the detectors may be already digitally processed to some degree prior to this measurement point. The single-pole reference filter characteristic is also not representative of the multi-pole, high Q-factor filtering characteristics of actual systems. Another reason for the inadequacy of the NETD is the presence of significant directional noise components in second generation systems. These directional noise components exhibit noise patterns in the displayed imagery, and may overshadow the effects of simple detector noise. The directional noise components arise from such diverse sources as signal processing, focal plane non-uniformities, $1/f$ noise, and other 'fixed-pattern' defects in the imaging system.

These additional noise factors can be temporal or spatial in nature, and typically represent recurrent noise phenomena that cause fixed patterns of degradation in the displayed image. The frequency spectra of the directional noise components have, typically, predominantly low frequency characteristics whose effect is to change the nature of the total system noise from a white gaussian expectation to a highly directional characteristic. This modified system noise can no longer be neatly characterized by a single parameter such as NETD. Directionality of noise was not as obvious in first generation systems, where emphasis was placed on quantifying temporal white detector noise [Ref. 13]. In second generation systems, however, these fixed-pattern type noise sources are present and their effect on the output spectrum cannot be ignored.

A three dimensional noise model using a directionally dependent coordinate system has been developed by the U.S. Army Night Vision and Electronic Sensors Directorate (NVESD) [Refs. 13 through 16]. In this new methodology, the total noise present is analyzed in terms of eight components, corresponding to the directional combinations defined by the three-dimensional (3-D) coordinate system. Figure 3.1 depicts the composite data set, and the directional axes. Each successive frame contains the individual output signal of each element in the rows and columns of the detector array for that frame.

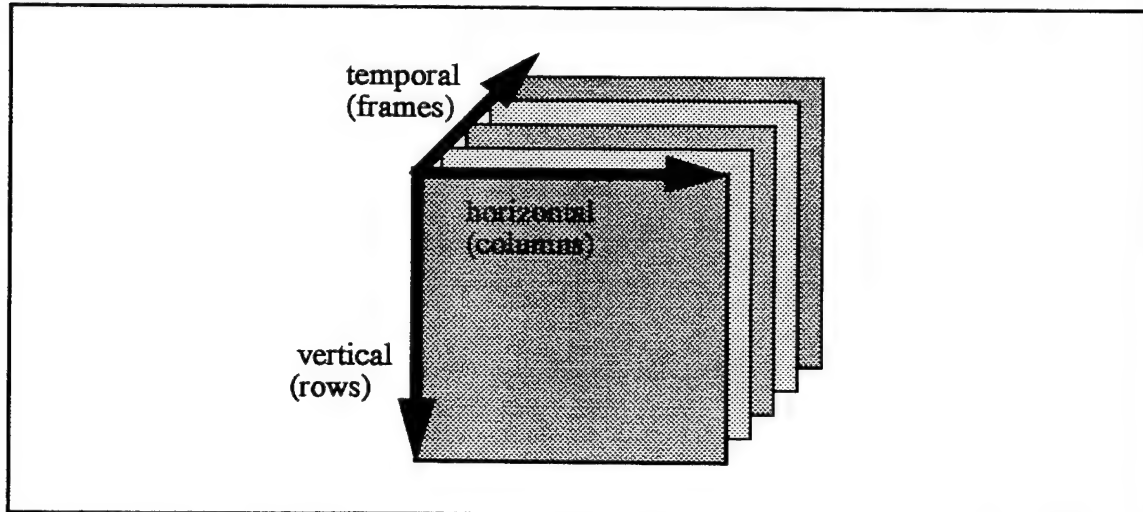


Figure 3.1. Three dimensional noise directional coordinate axes

The three dimensional noise analysis coordinate system includes temporal, horizontal, and vertical axes to represent directional noise phenomena. Noise types are characterized by directional subscripts (t,v, and h) corresponding to temporal, vertical and horizontal directions, or combinations of these. The directional noise components are considered to be ergodic, and each has zero mean [Refs. 13 and 14]. Their statistical independence allows the characterization of each type of noise from a composite set of sequential digitized output frames of the imaging system. The frames consist of the global average (output signal corresponding to the scene), plus the effects of the seven directional noise types. The total magnitude of one frame of the detector output composite data set can be represented by:

$$U(t, v, h) = S + N_t + N_v + N_h + N_{th} + N_{tv} + N_{vh} + N_{tvh}, \quad (3.1)$$

where S is the global average (signal), and N represents the noise component in the subscripted direction. For example, N_t represents 'frame-to-frame' noise that varies between successive frames, but is not correlated in the vertical or horizontal directions. Another example is N_{vh} which represents pixel non-uniformities in an array. These pixel non-uniformities cause spurious outputs from individual 'bad' pixels, independent of their row or column affiliated trends, and independent of time.

The noise quantization process uses a directional averaging image processing technique on the rows, columns, and frames of the composite data set to determine the statistical characteristics of the noise as measured in the various directions defined by the coordinate system. The ergodicity of directional noise components allows each directional component to be isolated from the others as the directional statistics are measured. A complete discussion of the directional noise averaging process is contained in Ref. 14. After the statistical processing of the composite data set is complete, each noise type is characterized by its standard deviation about a mean of zero. The characteristic standard deviations are used to determine directional noise correction factors that incorporate these second generation noise effects into the predictive model for the MRTD.

The 3-D noise components are described in Table 3.1, where each noise component is represented by its standard deviation, σ , with the appropriate subscripts. The seven types

TABLE 3.1. 3-D Noise Components

noise component	description	source
σ_{tvh}	temporal pixel noise	shot and thermal noise
σ_{vh}	fixed pixel noise	pixel non-uniformity
σ_{tv}	temporal row noise	readout line processing
σ_v	row noise	line to line non-uniformity
σ_{th}	temporal column noise	readout column processing
σ_h	column noise	columnar non-uniformity
σ_t	frame-to-frame noise	frame bounce

of directional noise are most usefully described in terms of their underlying phenomena [Ref. 12]. Temporal pixel noise is that white detector noise caused by random temporal fluctuations of detector output about a mean of zero. This was the only noise component considered in first generation models, and is an unavoidable consequence of the photon arrival and current flow processes (Johnson and Shot noise). The object of good TIS design is to reduce all other noise components so that this unavoidable noise is all that remains. Row, column, and fixed pixel noise are the three temporally independent noise components. They arise from detector non-uniformities in the vertical, horizontal, and two-dimensional directions. The source of these non-uniformities can be a lack of precision in offset, gain, or manufacture of the individual detector elements that make up an array. These noise types, although variant along the rows and columns of the composite data set, are consistent from frame to frame. This is often referred to as 'fixed pattern' noise, because there is a fixed pattern of degradation in the displayed image. For example, a particular row may be consistently 'brighter', on average, than its neighbor rows, causing a fixed pattern of degradation that doesn't depend on the particular column or frame in the

composite data set. The temporally variant noise components, temporal row noise, temporal column noise, and frame-to-frame noise, are most prevalent in scanning type systems. This noise component can arise from low frequency or 1/f noise in the offset level of the combined detector outputs. These temporal types of noise may also be present for a slowly changing scene. The temporal noise components can usually be reduced or eliminated by good design.

Because of the ergodicity assumption, the total system noise standard deviation can be written as the root sum square of the noise components [Ref. 15]:

$$\sigma_{\text{total}} = (\sigma_t^2 + \sigma_v^2 + \sigma_h^2 + \sigma_{tv}^2 + \sigma_{th}^2 + \sigma_{vh}^2 + \sigma_{tvh}^2)^{0.5} \quad (3.2)$$

Once the directional noise components have been determined for a particular imaging system, they can be used to modify the prediction of MRTD from that based on temporal pixel noise alone (as was done in first generation models). The total system noise contains all the random noise effects that will degrade imaging system performance. The ergodicity assumption implies that horizontal MRTD (bars oriented vertically, but spaced horizontally) and vertical MRTD (vice-versa) measurements are only degraded by noise components that contain that direction. For example, horizontal MRTD prediction will include spatial column noise, but not spatial row noise. [Ref. 13]

Each of the directional coordinate axes has unique eye/brain integration factors, E_t , E_v , or E_h . These factors are model specific, and describe the way the eye/brain process acts on the signal and noise in the given direction. These eye/brain integration effects are analogous to the SNR enhancing 'perception factors' cited by Lloyd [Ref. 3, Chapter 5]. They differ from model to model, and depend to a great extent on the method used to model the eye/brain process. Each integration factor will tend to increase or decrease the signal to directional noise ratio when the noise component direction and integration direction coincide. When the noise and integration effects are applied to each of the horizontal and vertical directions, the appropriate composite noise terms can be described by:

$$\Omega_h = (\sigma_{tvh}^2 E_t E_v(f) E_h(f) + \sigma_{vth}^2 E_v(f) E_h(f) + \sigma_{th}^2 E_t E_h(f) + \sigma_h^2 E_h(f))^{0.5} \quad (3.3)$$

and,

$$\Omega_v = (\sigma_{tvh}^2 E_t E_v(f) E_h(f) + \sigma_{vth}^2 E_v(f) E_h(f) + \sigma_{tv}^2 E_t E_v(f) + \sigma_v^2 E_v(f))^{0.5} \quad (3.4)$$

The composite system noise terms are then used to calculate MRTD noise correction factors, that modify the original formulation of NETD to include all 3-D noise components. The analysis usually infers an initial representation of MRTD in the form:

$$\text{MRTD}_z = C_s \times \text{NETD} \times k_z(f_z), \quad (3.5)$$

where the 'z' subscript refers to either the horizontal or vertical direction as appropriate. 'C_s' is a frequency dependent numerical constant that includes the MTF characteristics of the system, NETD is the first generation noise factor due to temporal pixel noise only, and k_z is the appropriate directional correction factor calculated according to the second generation model used. The formulation of all three of the terms appearing on the right hand side of Eq. 3.5 will differ according to the unique aspects of the second generation model employed. To illustrate the concept, the 3-D noise formulation used in the FLIR92 model is presented in the next section.

The 3-D noise analysis is a step forward from simple first generation modeling methods. It has the advantage of being measured from hard laboratory data, and more accurately represents some of the noise effects found in second generation imagers. However, although the methodology is easily incorporated into a wide variety of models, the physical difficulties realized in actually quantifying the individual directional noise components limits the implementation of a 3-D noise analysis in some applications.

B. 3-D NOISE IN FLIR92

The FLIR92 model produced by the NVESD has become the de facto standard in second generation modeling. A complete discussion of the FLIR92 model is appropriate to this document for completeness, and has been included as Appendix C. This section will focus on the way FLIR92 implements a 3-D noise analysis as an illustration of the topics presented in the preceding section. The ideas and equations of this section are adaptations of those found in the original FLIR92 documentation [Refs. 13 through 16].

The updated treatment of noise to include 3-D noise concepts is one of the new features of the FLIR92 model. Recall that the total 3-D noise standard deviation was expressed in terms of the standard deviations along the combinations of temporal, vertical, and horizontal directions as:

$$\sigma_{\text{total}} = (\sigma_t^2 + \sigma_v^2 + \sigma_h^2 + \sigma_{tv}^2 + \sigma_{th}^2 + \sigma_{vh}^2 + \sigma_{tvh}^2)^{0.5}, \quad (3.6)$$

where the noise descriptions are the same as those presented in Table 3.1.

In FLIR92, the modeling of each of the seven noise components is implemented by either scaling each of the noise components to σ_{tvh} , or by inputting actual measured values. Currently, σ_{tvh} is the only noise component that can be predicted from system parameters. The value for σ_{tvh} is calculated in a manner similar to the method used by first generation models to calculate the NETD. FLIR92, however, calculates σ_{tvh} based on the actual bandwidth of the system, not the artificial reference bandwidth used by NETD. The value for σ_{tvh} is given by:

$$\sigma_{tvh} = \text{NETD} \times \frac{\sqrt{\Delta f_{\text{sys}}}}{\sqrt{\Delta f_n}} \quad (3.7)$$

where Δf_n is the noise bandwidth for the NETD calculation, and Δf_{sys} is the actual bandwidth of the system. FLIR92 uses the calculated value of σ_{tvh} , the formulation of the system MTF (Appendix C), a directional noise correction factor, and eye/brain spatial and

temporal integration factors to calculate the predicted MRTD. The FLIR92 MRTD formulation matches the general form given in Eq. 3.5, and is given by:

$$\text{MRTD}_z(f_z) = \left(\frac{\frac{\pi^2}{8} \text{SNR}_{\text{thr}} \sigma_{\text{tvh}} k_z(f_z)}{H_{\text{sys}}(f_z)} \right) [E_t E_{h_z}(f_z) E_{v_z}(f_z)]^{0.5} . \quad (3.8)$$

Recall the 'z' subscript implies that the variable is to be evaluated in either the horizontal or vertical direction as appropriate. Most of the terms in Eq. 3.8 can be recognized as 'carry-overs' from the original Ratches MRTD formulation, given as Eq. 2.8. The remaining terms are calculated by FLIR92 in the manner described below. For convenience, the MRTD parameters are summarized in the Table 3.2.

TABLE 3.2. MRTD equation parameters

parameter	description
SNR_{thr}	threshold SNR for resolution
σ_{tvh}	random pixel noise
k_z	3-D noise correction factor
H_{sys}	system MTF as described in Appendix C
E_z	directional eye/brain integration factor

Although Eq. 3.8 appears complex, it is most easily interpreted as a modification of noise temperature by system parameters and psycho-physical effects to give an MRTD. The only term with units is the σ_{tvh} term, given in degrees Celsius. The remainder of the terms are dimensionless factors that either increase or decrease this 'temperature' as a function of target spatial frequency. The numerical constant, threshold SNR, and system MTF, are defined as they were for first generation models. FLIR92 recommends a value of 2.5 as a reasonable average value for threshold SNR, and an eye integration time of 0.1 sec. Recall that the σ_{tvh} term represents temporal pixel noise, like the NETD term of the 1975 model, but modified by the system bandwidth. In general form, it is given by:

$$\sigma_{tvh} = \frac{4F^2 \sqrt{\Delta f_{sys}}}{\pi \tau_o \sqrt{A_d} \left(\int_{\lambda_1}^{\lambda_2} D^*(\lambda, 300) \frac{\partial W}{\partial T}(\lambda) d\lambda \right)} \quad (3.9)$$

The 3-D directional noise components enter the equation via the $k_z(f_s)$ term. This term includes the seven 3-D noise components to the extent they are applicable to the type of system being modeled. The term is derived from the general noise term forms given as Eq. 3.3 and Eq. 3.4. The σ_{tvh} term and the eye/brain integration terms appear explicitly in the MRTD equation Eq. 3.8, so these terms are divided out of the correction factors. The resulting horizontal and vertical correction factors are given by:

$$k_h(f_x) = \left(1 + \frac{\sigma_{vh}^2}{\sigma_{tvh}^2 E_t} + \frac{\sigma_{th}^2}{\sigma_{tvh}^2 E_{v_h}(f_x)} + \frac{\sigma_h^2}{\sigma_{tvh}^2 E_t E_{v_h}(f_x)} \right)^{0.5} \quad (3.10)$$

and,

$$k_v(f_y) = \left(1 + \frac{\sigma_{vh}^2}{\sigma_{tvh}^2 E_t} + \frac{\sigma_{th}^2}{\sigma_{tvh}^2 E_{h_v}(f_y)} + \frac{\sigma_v^2}{\sigma_{tvh}^2 E_t E_{h_v}(f_y)} \right)^{0.5} \quad (3.11)$$

Each directional correction factor (vertical or horizontal) contains the noise components and integration factors appropriate to it. (Recall that by popular convention the 'x' subscript is used for horizontal parameters and the 'y' subscript is used for vertical parameters.)

The final terms of the MRTD formulation that require elaboration are the spatial and temporal integration factors themselves. For staring second generation imagers, there are five eye/brain integration factors required. The factors are described in Table 3.3. Their formulation in FLIR92 is given by the equations that follow.

TABLE 3.3. Eye/brain integration factors

Factor	Description
E_t	eye/brain temporal integration
E_{vv}	eye/brain vertical integration, vertical direction
E_{hh}	eye/brain horizontal integration, horizontal direction
E_{vh}	eye/brain vertical integration, horizontal direction
E_{hv}	eye/brain horizontal integration, vertical direction

The eye/brain temporal integration factor is given as:

$$E_t = \frac{\alpha_t}{F_{\text{dot}} t_e}, \quad (3.12)$$

where α_t is a frame to frame correlation factor, usually set to one. This temporal integration factor is identical to that given by Lloyd [Ref. 3, Chapter 5].

The spatial directional integration factors used in FLIR92 are more complex, and attempt to model the eye/brain integration along the bars in both directions. They are given in the FLIR92 reference guide [Ref. 16] as:

$$E_{z_z}(f_z) = \frac{\alpha}{s_z} \left[\int_{-\infty}^{\infty} H_{\text{NF}_z}^2(f) \left(\frac{\sin\left(\frac{\pi f}{2f_s}\right)}{\frac{\pi f}{2f_s}} \right)^2 df \right] \quad (3.13)$$

and,

$$E_{z_z}(f_z) = \frac{\alpha}{s_z} \left[\int_{-\infty}^{\infty} H_{\text{NF}_z}^2(f) \left(\frac{\sin\left(\frac{7\pi f}{2(f_s)}\right)}{\frac{7\pi f}{2f_s}} \right)^2 df \right], \quad (3.14)$$

where the \bar{z} term indicates the direction perpendicular to z (e.g., 'y' in the case of horizontal where $z=x$). The H_{NF}^2 term is a system noise filter MTF given in Appendix C. An approximate form of these integration factors is given:

$$E_h(f_z) \approx \frac{\alpha_h}{R_h L_h(f_z)} \quad (3.15)$$

and,

$$E_v(f_z) \approx \frac{\alpha_v}{R_v L_v(f_z)}, \quad (3.16)$$

where α_h and α_v , the horizontal and vertical correlation factors, are usually set to one; and R_z and L_z are the spatial sampling rates (samples/mrad) and bar target long dimension (cycles/mrad) respectively [Ref. 15]. These can be shown to be analogous to Lloyd's vertical integration 'perception factor' described for first generation horizontal MRTD.

The FLIR92 model calculates a separate value for $MRTD_h$ and $MRTD_v$. The implied ergodicity of the two allows the geometric mean of the horizontal and vertical MRTD values to give a 2-D MRTD value. Sample outputs from the FLIR92 program are contained in Appendix C.

C. SAMPLING AND ALIASING

The 3-D noise analysis presented in Section A is based on a linear MTF analysis of a given system. This linear degradation that occurs in the reconstruction of an image because of the filtering out of high spatial frequency components of the target scene is referred to as 'blurring' [Ref. 17]. This problem is adequately explained in terms of the generally low-pass nature of the system MTF, and linear systems theory. There are other noise effects which cannot be appropriately modeled using linear systems theory. In particular, the problem of representing a sampled imaging system and aliasing effects caused by undersampling cannot be modeled by the conventional concept of an OTF. Sampling is inherent to almost all real imaging systems, and can occur in several dimensions due to scanning, multiplexing, digitization, or the finite discrete nature of the

detector elements and the detector array geometry. This second type of image degradation, caused by the masking of spatial detail by the 'folding over' of high frequency components into the pass band of the system by undersampling, is referred to as 'aliasing' [Ref. 17]. Aliasing occurs in sampled imaging systems when the sampling frequency is below the Nyquist rate for the highest spatial frequency content in the imaged scene. This situation violates the premises of isoplanatism and linearity that allow the application of linear systems theory to 'blurring' type noise [Ref. 4]. Specifically, an input at a high frequency can cause a spurious output at a lower spatial frequency if the system is undersampled. Also, the response of the detector array is not spatially invariant, as it depends on where the image falls on the detector plane in relation to the active area of the detector elements and the dead space between them. Sampling is an unavoidable consequence, even in first generation TIS, but its effects were largely ignored in first generation modeling. Subsequent to the development of first generation models, considerable effort was expended on quantifying the effects of sampling and aliasing on displayed imagery [Refs. 17 through 22]. In the study of sampling and aliasing effects and their effect on displayed imagery, it has been found that most significant aliasing effects are caused by the finite active area and spacing of the detector elements in an array [Ref. 18]. Other sampling artifacts certainly exist in the spatial and temporal domains, but these may be eliminated or reduced through proper system design. By convention, rectangular geometry for detector elements is usually assumed for the analysis of aliasing effects. This is the most common geometry encountered because it is the most practical for FPA construction. Other detector geometries are in use, and may be substituted as required. Figure 3.2 portrays the salient features of the spatial sampling process defined by the detectors.

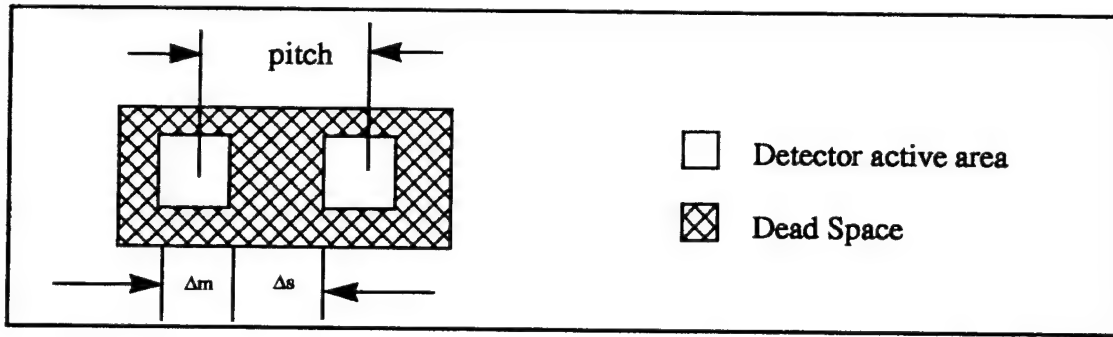


Figure 3.2. Spatial sampling by a rectangular detector array

The spatial sampling period in mrad is given by:

$$\Lambda = \frac{\Delta m + \Delta s}{f_{ocal}} \quad (3.17)$$

where f_{ocal} is the focal length of the system optics. The sampling frequency is defined as:

$$f_s = \frac{1}{\Lambda} \quad (3.18)$$

Because of the sampling process, there is a characteristic maximum frequency above which the system will no longer reproduce input frequencies accurately. The limiting spatial frequency for undersampled systems is the Nyquist frequency of the signal [Ref. 25]. This represents the highest spatial frequency content of the scene that can be reproduced without aliasing,

$$f_N = \frac{f_s}{2}. \quad (3.19)$$

Staring systems are usually undersampled because of the small dimension of the FPA. The characteristic maximum frequency is based on the center to center spacing or 'pitch' and the size of the detector elements as shown in Fig. 3.2. For square detectors with equal pitch in both horizontal and vertical directions, this frequency is the same in both directions.

The fact that aliasing is predominantly a high frequency phenomenon suggests that aliasing may not be significant for natural scenes of a generally aperiodic nature. However, while it is true that aliasing effects are most readily apparent for high frequency periodic images, it is not true that natural aperiodic scenes do not suffer from significant image degradation as well. Aliasing present in aperiodic scenes may not be recognized as such in the presence of 3-D noise, because it is indistinguishable from other types of noise in the final image displayed. Thus, for the purposes of TIS modeling, aliasing is often treated as signal dependent additive noise. [Ref. 18]

The spatial domain description of the sampling process is shown in Fig. 3.3.

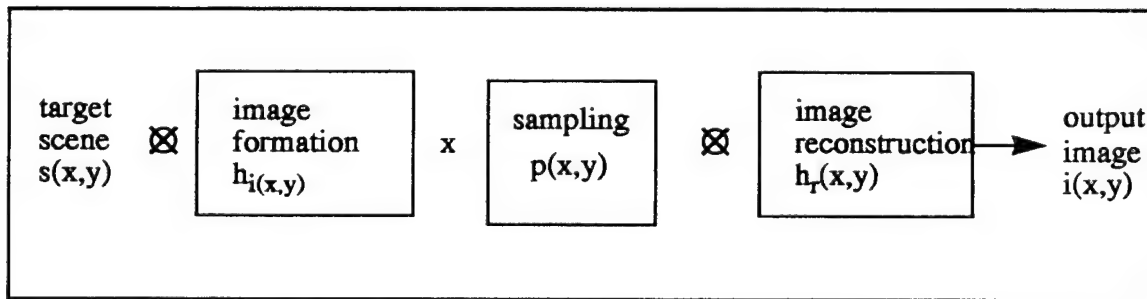


Figure 3.3. Spatial domain sampling process, after Ref. 18

In Fig. 3.3, the effects of the entire thermal imaging system are broken down into three components. The input spatial target scene is described by a band-limited two dimensional spatial pattern, $s(x,y)$, representing the projection of the scene onto the detector array, free of any degradation. All filtering effects up to and including the detector are lumped together in an 'image formation' point spread function, $h_i(x,y)$. This is followed by a sampling function, and an 'image reconstruction' point spread function, $h_r(x,y)$, which includes all post-detector electronic and display effects. The imaging process can be described mathematically as a convolution/multiplication:

$$i(x, y) = [(s(x, y) \otimes h_i(x, y)) \times p(x, y)] \otimes h_r(x, y) \quad . \quad (3.20)$$

The application of the Fourier transform allows a convenient description of the process. Figure 3.4 shows the process in the transformed domain. Note the convolutions

are replaced by multiplication and the sampling process has become a convolution. This is identical to the separation of the averaging and sampling process described in Chapter I.

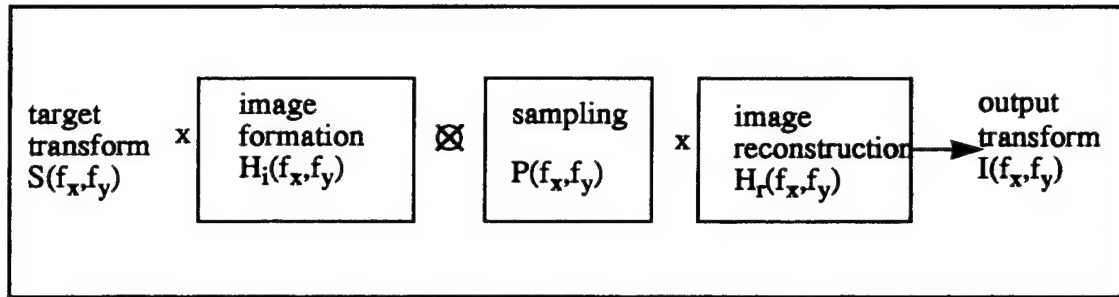


Figure 3.4. Spatial frequency domain representation, after Ref. 18

The input scene is now represented by the complex-valued Fourier transform, $S(f_x, f_y)$. The target transform will typically be band-limited and symmetric for real target scenes. The output transform is now given by:

$$I(f_x, f_y) = [(S(f_x, f_y) \times H_i(f_x, f_y)) \otimes P(f_x, f_y)] \times H_r(f_x, f_y) \quad (3.21)$$

where both H_i and H_r will be the two dimensional cascaded MTF's both covering the horizontal and vertical dimensions. These cascaded functions will typically be Gaussian as described by the central limit theorem of probability [Ref. 6]. The interesting effect comes from the sampling term. In the spatial frequency domain, this process is represented by a two dimensional array of sampling delta functions, spaced at integer multiples of the sampling frequency. If an infinite array of sampling delta functions is assumed, the sampling transfer function can be represented as an infinite series of delta functions:

$$P(f_x, f_y) = \sum_{-\infty}^{\infty} \sum_{-\infty}^{\infty} \delta(f_x - kf_s) \delta(f_y - kf_s) \quad (3.22)$$

For real imaging systems, the sampling array is not infinite. This will cause the spreading of the individual frequency domain delta functions by the fourier transform of the detector shape (they are no longer strictly delta functions). The sampling MTF is convolved with

the image transform and the image formation MTF. the result is a periodic repetition of the filtered image in the frequency domain, at intervals corresponding to the sampling frequency of the array. This is depicted in one dimension as Fig. 3.5, where f_c is the highest spatial frequency present in the filtered image.

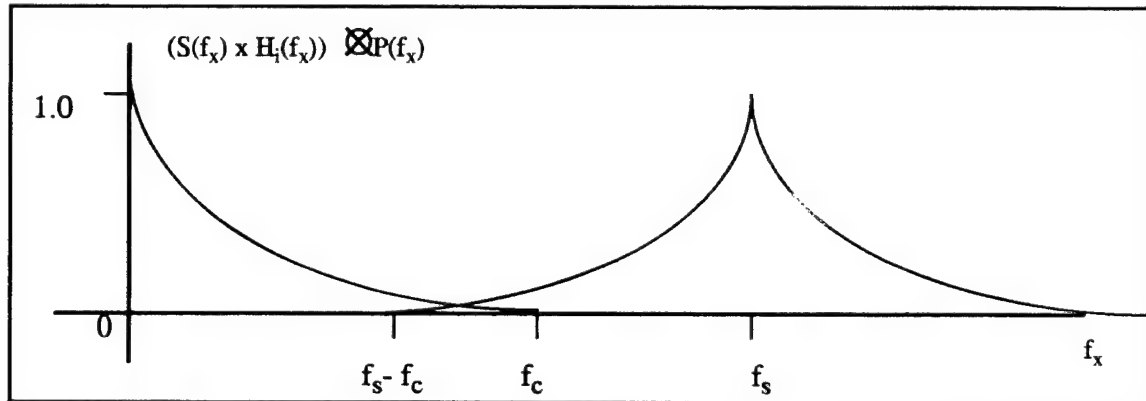


Figure 3.5. One dimensional representation of sampling process

If the system is undersampled, i.e. $f_s < 2f_c$, there will be an overlap in the resultant spectra. This overlap will exist in both the horizontal and vertical spatial frequency directions, and is the source of aliasing. The output spectrum is no longer linear because a frequency input near the cutoff is no longer faithfully reproduced. Frequencies above the cutoff have been 'folded over' onto the original spectrum due to undersampling. This periodic spectrum is then filtered by the reconstruction filter. Figure 3.6 portrays the frequency domain effect of the image reconstruction filtering of the image for a case where the reconstruction filter has a greater bandwidth than the image formation filter.

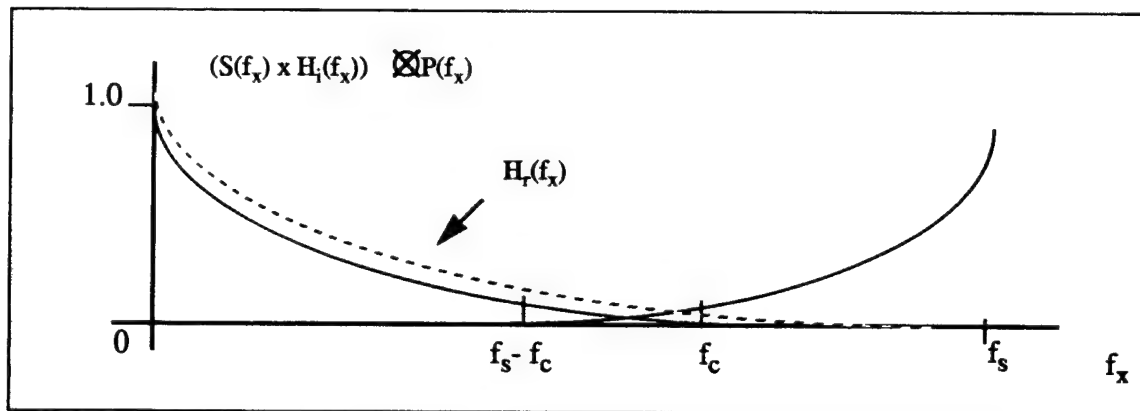


Figure 3.6. Application of a wide bandwidth reconstruction filter

The product of the two functions will contain a vestige of the overlapping portion of the filtered image spectrum, as appears in Fig. 3.7.

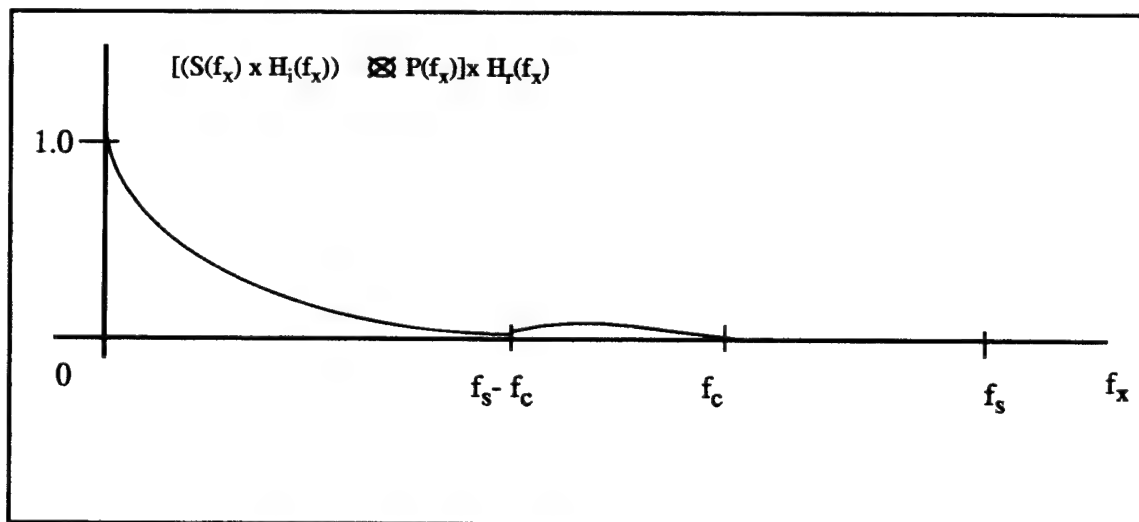


Figure 3.7. Resulting spectrum with aliased component

The vestige of the overlap will survive the image reconstruction filtering, and will have a spurious high frequency aliasing effect when the spectrum of Fig. 3.7 is inverse transformed back into the spatial domain. This spurious high frequency term can be treated as additive noise [Ref. 18]. Figure 3.7 suggests that the output spectrum can be divided into two components. The image spectrum is represented as:

$$I(f_x, f_y) = I_{\text{correct}}(f_x, f_y) + A(f_x, f_y) \quad (3.23)$$

where I_{correct} , the ‘good’ part of the spectrum that represents the properly filtered (no aliasing) output spectrum, is given by:

$$I_{\text{correct}} = S(f_x, f_y)H_i(f_x, f_y)H_r(f_x, f_y); \quad (3.24)$$

and the aliasing term, defined as the spurious response due to the vestige of the overlapping spectra, is given by

$$A(f_x, f_y) = \left[\sum_{\substack{n=-\infty \\ n \neq 0}}^{\infty} \sum_{\substack{m=-\infty \\ m \neq 0}}^{\infty} S(f_x - nf_{sx}, f_y - mf_{sy})H_i(f_x - nf_{sx}, f_y - mf_{sy}) \right] \times H_r(f_x, f_y) \quad (3.25)$$

The second term has an obvious negative impact on image quality. As Fig. 3.6 implies, the most significant aliasing terms are those immediately adjacent to the original spectrum and the nearest cross-terms (i.e., combinations of $A(nf_x, mf_y)$ where $m=-1,0,1$ and $n=-1,0,1$). These immediately adjacent terms are the only ones included in the VISMOLDII model presented in Chapter V. If the inverse Fourier transform of Eq. 3.23 is taken, the resulting form motivates the representation of aliasing as additive noise:

$$i(x, y) = i_{\text{correct}}(x, y) + a(x, y) . \quad (3.26)$$

It is important to note that the aliasing term contains all frequencies that are effected by the overlapping spectra. The correct image output corresponds to the properly filtered image ignoring the sampling. The aliased component represents a ‘correction’ factor that must be added to the correct image in order to match the image actually displayed. If this correction factor is interpreted as noise, then it is both additive and scene dependent [Ref. 18]. The effects of this aliasing noise have been studied in the context of TV and motion picture images for many years [Ref. 19]. The application of this effect to TIS modeling is a natural extension, and has been shown to have a measurable impact on MRTD [Ref. 20]. In fact, in some scenarios, aliasing effects may be considerably more degrading than spatial noise effects [Ref. 17].

Several approaches have been presented to minimize the effects of aliasing. One method that is suggested by Fig. 3.6 is the trade-off incurred in the design of the reconstruction filter. If the bandwidth of the reconstruction filter is decreased, less of the sideband of the overlapping second periodic image is allowed into the final output spectrum. Unfortunately, this has the obvious negative effect of filtering out some of the high frequency detail of the original image as well [Ref. 18]. Another method involves the proper processing of the reconstructed image by certain digital signal processing techniques to remove the spurious component [Ref. 21]. Still a third method is the careful control of the shape of the detector element and the resulting image formation filter [Ref. 17]. The use of microscanned imagery is another method to reduce aliasing effects by effectively increasing the sampling frequency. In this method, the image is shifted around on the detector plane in half detector-sized increments. This process increases the effective sampling frequency, thus it is less susceptible to aliasing and sample scene phasing [Ref. 22].

Proper design to eliminate or reduce the effects of aliasing is certainly desirable, but the challenge of incorporating aliasing effects into TIS MRTD prediction models remains. Most current models deal with the modeling difficulties by ignoring aliasing entirely. Others do not provide outputs for frequencies above the Nyquist frequency. Neither approach is optimal, indicating that further work is required in this area. The second generation visibility model, VISMODII, incorporates the aliasing effect as part of a contrast transference parameter, as will be discussed in Chapter IV.

D. SAMPLE SCENE PHASING EFFECTS

Because scene phasing effects and aliasing effects are inextricably linked, they must be considered together. Aliasing, as discussed in the previous section, arises from undersampling of the target image by the detector array. Scene phasing is a measurable effect of displacement of the target image from the center of the detector elements on the focal plane of the imager. Both of these effects can be significant, especially for

undersampled systems. A mathematical treatment of the process is provided here to demonstrate the validity of the aliasing/scene phasing characterization used in VISMODII.

The sampling process can be described as a two dimensional array of delta functions as shown in Fig. 3.8. Each delta function is positioned at the center of an individual detector element in the FPA.

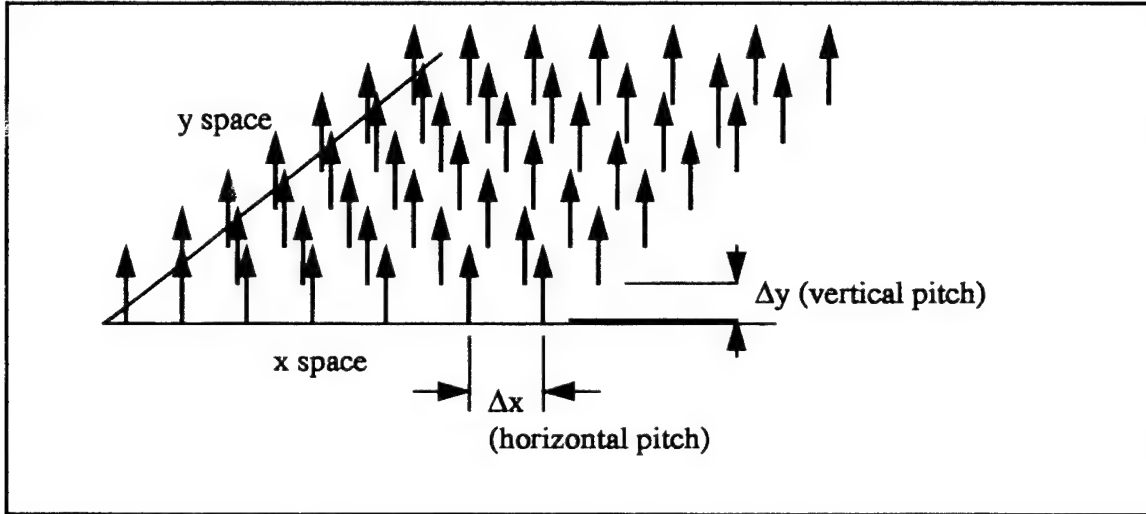


Figure 3.8. Two dimensional sampling array

The effects of scene phasing are felt in two dimensions. The mathematical discussion of this effect is greatly simplified, however, if reduced to one dimension. The discussion here is given in one dimension but is easily extended to a two dimensional sampling array. In one dimension, the sampling array looks like a line of delta functions spaced by the detector pitch. If the image to be sampled and the sampling elements are misaligned, the effect may be modeled as a spatial shift for the sampling array. This effect is obviously most troublesome for severely undersampled systems.

To represent the detector plane image/detector center misalignment, the sampling function is displaced from the origin a distance 'b' as shown in Fig. 3.9. The sampling function is described by the comb function:

$$\text{comb}\left(\frac{x-b}{\Delta x}\right) = \sum_{-\infty}^{\infty} \delta(x-b-n\Delta x) \quad (3.27)$$

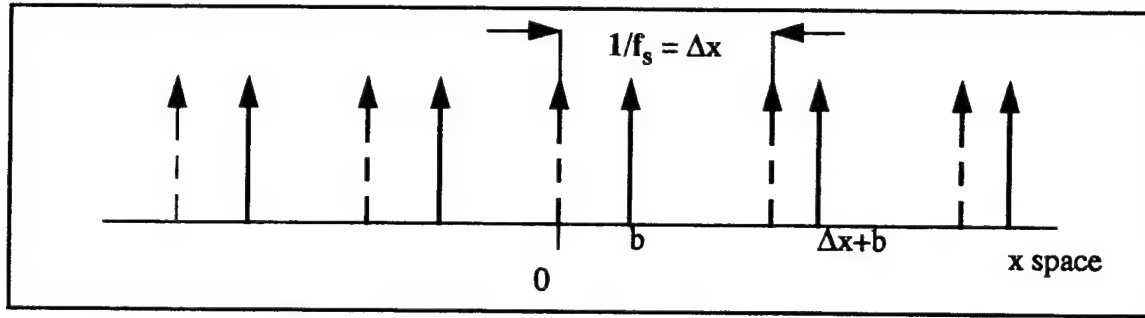


Figure 3.9. Displaced sampling function in one dimension

From Fourier theory, if the Fourier transform of a spatial function is denoted by:

$$\mathfrak{F}\{g(x)\} = G(f), \quad (3.28)$$

then the Fourier transform of the shifted function is given by:

$$\mathfrak{F}\{g(x - b)\} = G(f)e^{j2\pi bf}. \quad (3.29)$$

Sampling is a spatial domain multiplication process. In the frequency domain, then it requires the convolution of the Fourier transform of the filtered spectrum and the Fourier transform of the sampling function itself. By Eq. 3.29, The Fourier transform of the shifted train of delta functions is given by:

$$\mathfrak{F}\left\{\text{comb}\left(\frac{x - b}{\Delta x}\right)\right\} = \text{comb}\left(\frac{f}{f_s}\right)e^{j2\pi bf} = e^{j2\pi bf} \sum_{-\infty}^{\infty} \delta(f - nf_s) \quad (3.30)$$

The convolution integral for two functions u and v may be described as:

$$u \otimes v = \int_{-\infty}^{\infty} u(\tau)v(x_0 - \tau)d\tau \quad (3.31)$$

The frequency domain convolution of the filtered image spectrum, $S(f)$, with the Fourier transform of the sampling function is then given by:

$$\text{Sampled spectrum} = \int_{-\infty}^{\infty} S(v)\delta(f - nf_s - v)e^{j2\pi b(f - v)}dv \quad (3.32)$$

Since the convolution of a function with a delta function is exactly that function repeated at the location of the delta function, the output of the integration gives:

$$\text{Sampled spectrum} = S(f - nf_s)e^{j2\pi b(nf_s)} \quad (3.33)$$

where n is the order of replication, $n = 0, +1, -1, +2, -2, \dots$. Thus, the sampled spectrum is the original filtered spectrum repeated at integer multiples of the sampling frequency, and multiplied by an exponential due to the original scene phasing. The sampled spectrum is illustrated in Fig. 3.10.

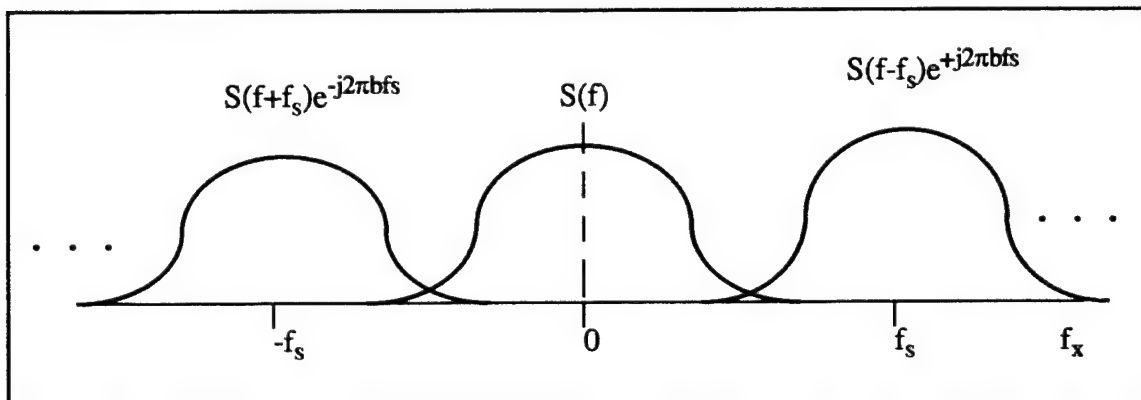


Figure 3.10. Sampled target spectrum in spatial frequency domain

The value of 'b', causes a periodic phase distortion in the output that is zero whenever b is zero or a multiple of the detector pitch. Intuitively, the value of b that would cause the greatest distortion would be exactly one half the detector pitch, corresponding to exact misalignment between the target image and the detector array. The effect of scene-phasing on MRTD prediction will be explored in Chapter VI.

E. CLOCK-OUT FREQUENCY CONVERSION EFFECTS

In Chapter I, a simple equation relating the spatial and temporal frequency for scanning first generation systems was presented as Eq. 1.8. In this section it will be demonstrated that this simple relationship does not apply to staring FPA's. This topic has been ignored by most second generation models. In FLIR92, the electrical system is not considered to be a limiting factor for FLIR MRTD performance [Ref. 16]. In fact, this effect can be significant for electrically bandwidth-limited systems. An ATR device may fall into this category. As discussed in Chapter I, the electrical system components act on a

temporal rather than a spatial signal. The way in which the detector FPA converts the spatial image received into an electrical signal becomes an important consideration. For first generation scanning systems, this was a rather simple procedure. In these systems, the image shifted every interval of the dwell time, and there was a serial output from the single detector clocked-out at the same interval. In FPA's, however, the 'clock-out' process can be more complicated. Figure 3.11 portrays two possible clock-out configurations.

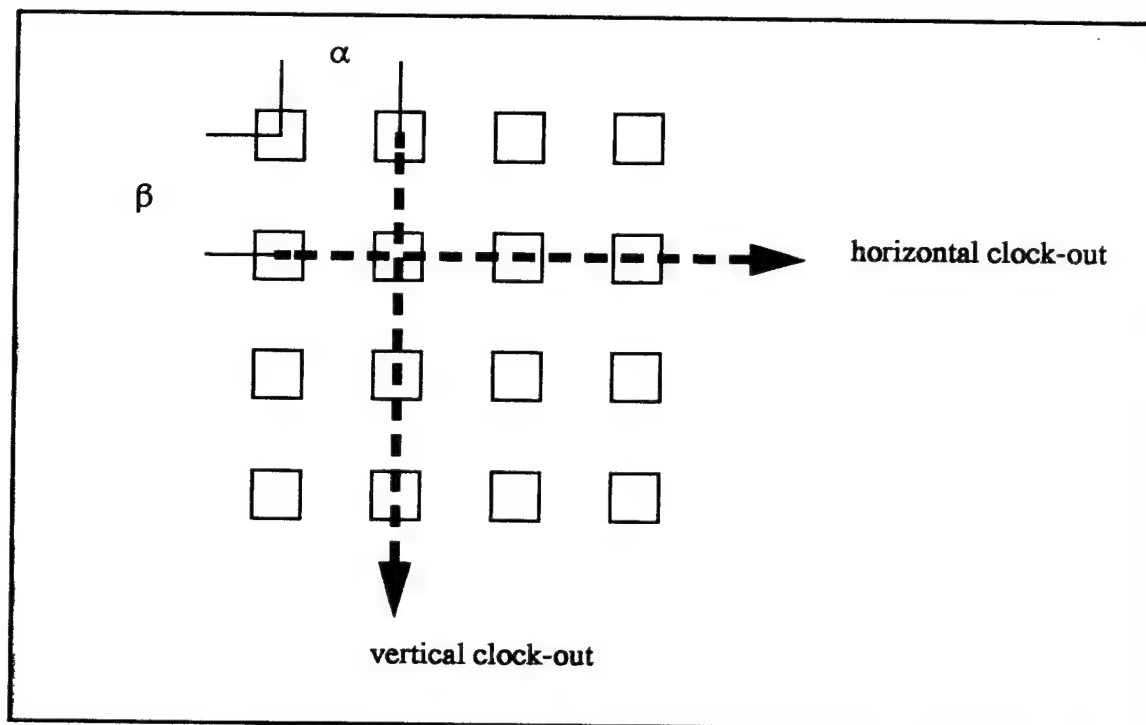


Figure 3.11. Two possible clock-out patterns for an FPA

In both clock-out patterns, the dwell time for an individual detector is the entire frame period. If the image is converted to an analog video signal, then the outputs of the detectors must be converted to a serial analog signal based on a clock-out interval between elements. Whereas in first generation systems the clock-out interval was equal to the dwell time, in FPA systems the clock out interval between adjacent detector elements is a more complex function of the clock-out geometry, number of elements, and the frame rate. It is also seen from the figure that the clock-out interval between horizontally adjacent elements may be different from the clock-out interval between vertically adjacent elements.

As an example, consider the representative horizontal clock-out geometry depicted in Fig. 3.11. In this typical case, the individual detector element outputs are clocked-out in a sequential fashion along a row, with the clock-out then proceeding down to the next row. This can be visualized as a reverse raster scan type process, where the clock-out direction and the scan direction are analogous. To relate a spatial frequency in the 'in-scan' direction (in this case a row) to a temporal frequency, it is necessary to relate the physical detector pitch (in mrad) to the scan time interval between adjacent detector elements in this direction.

The number of pixels subtended by one cycle of the bar pattern horizontally on the image plane corresponds to:

$$\text{number horizontal pixels} = \frac{2W}{\alpha} \quad (3.34)$$

The in-scan clock-out interval, τ_{cis} , is a function of the number of detectors in the (n row by m column) array and the frame rate given by:

$$\tau_{\text{cis}} = \frac{1}{F_{\text{dot}} \cdot n \cdot m} \quad (3.35)$$

To determine the total time it takes for a complete cycle of the bar to be clocked out, it is necessary to multiply the number of pixels by the clock-out interval per pixel:

$$\tau_{\text{cycle}} = \frac{2W}{\alpha} \times \frac{1}{F_{\text{dot}} \cdot n \cdot m} \quad (3.36)$$

The corresponding temporal frequency is the inverse of this quantity:

$$f_t = \frac{1}{\tau_{\text{cycle}}} = \frac{\alpha \cdot F_{\text{dot}} \cdot n \cdot m}{2W} \text{ Hz} \quad (3.37)$$

If the bar pattern fundamental spatial frequency, f_x , is defined to be $1/2W$ cy/mrad, then relating the two frequencies gives the conversion factor for the 'in-scan' direction:

$$f_t = \left(\frac{\alpha}{\tau_{\text{cis}}} \right) f_x \quad (3.38)$$

In the cross-scan or 'out-scan' direction, the clock-out time interval between adjacent elements is increased by the number of detectors in a row (n). Thus, the number of vertical pixels subtended by an image in the focal plane is:

$$\text{number vertical pixels} = \frac{2W}{\beta} , \quad (3.39)$$

and the clock-out interval between adjacent detectors is:

$$\tau_{\text{cos}} = \frac{1}{F_{\text{dot}} \cdot n} , \quad (3.40)$$

giving rise to the 'out-scan' conversion factor:

$$f_t = \left(\frac{\beta}{\tau_{\text{cos}}} \right) f_y . \quad (3.41)$$

Generalizing Eqs. 3.38 and 3.41 to include systems that may clock-out along the columns instead of the rows, and putting them in terms of TIS parameters, the general form of the conversion factors becomes:

$$\text{In - scan } f_t = f_{\text{in-scan}} \left(\frac{F_{\text{dot}} \cdot n \cdot m \cdot \Delta z}{f_{\text{ocal}}} \right) , \text{and} \quad (3.42)$$

$$\text{Cross - scan } f_t = f_{\text{cross-scan}} \left(\frac{F_{\text{dot}} \cdot n \cdot \Delta z}{f_{\text{ocal}}} \right) , \quad (3.43)$$

where the in-scan spatial frequencies, detector pitch, Δz , and number of elements refer to either the horizontal or vertical direction as appropriate for the clock-out pattern used.

This conversion is important in determining the difference in MRTD predictions for the horizontal and vertical directions, especially for electronic bandwidth limited systems. A quick glance at Eq. 3.42 and Eq. 3.43 reveal that the electrical frequencies in the in-scan direction will be greater by a factor corresponding to the number of detector elements in an in-scan row or column. This factor is typically between 128 and 512, so the effect is significant. Because the frequencies are higher, the electronic MTF will have a more severe filtering effect in the in-scan direction. One would expect, then, better MRTD

results in the cross-scan direction than the in-scan direction for electrically bandwidth limited systems that use such a clock-out procedure. Remember, the in-scan direction does not refer to either the horizontal or vertical MRTD in particular. In some systems, the in-scan direction will correspond to the horizontal. In others, it will correspond to the vertical, as determined by the clock-out pattern of the TIS.

Of course, this simple analysis is only applicable to systems that have a clock-out pattern similar to the one shown in Fig. 3.11. The concept, however, applies to all FPA systems that produce a serial output, such as analog video. The incorporation of this effect may be critical in some scenarios, for example, an electrically bandwidth-limited ATR device.

F. OTHER EFFECTS

Although modeling 3-D directional noise and aliasing are the largest second generation modeling concerns, they are not the only important ones. The consideration of sample scene-phasing and clock-out frequency conversion effects are also important. Some other effects that could be critical to some applications include detector signal processing, display enhancements, non-linear electronic signal processing, and display/observer interaction effects [Ref. 23]. These second generation concerns may or may not be included in a given second generation model, but should be kept in mind by system modelers and users. Each is briefly discussed in the following paragraphs.

Second generation detector arrays, unlike their predecessors, make use of some degree of signal processing in the detector array itself. This changes the nature of the output signal from the detector array. In first generation systems, the output signal was a continuous analog signal representing a spatial averaging across the detector's active dimensions. With second generation systems, the nature of this output may be such that it is a series of multiplexed digital outputs representing a serial combination of samples from several detector elements. Because of this multiplexing, it may not be possible to isolate noise and desired signals in some systems to be able to predict signal to noise performance.

Display enhancements have also changed the way images are presented to the user. These effects are not covered by standard linear systems theory. The display enhancements utilized in second generation systems include pseudo-color enhancement, discrete element LED or LCD displays, and the like. These display enhancements are not amenable to simple MTF analysis as is the standard CRT of first generation systems. Modeling research must be conducted to ensure proper interpretation of display enhancements on MRTD measurements.

Electronic signal processing of system outputs is a natural consequence of the growing sophistication of imaging systems. Electronic signal processing in first generation systems usually consisted of linear amplification, offsetting, and filtering. In second generation systems, signal processing takes the form of digitization, image enhancement, and image interpolation in addition to the basic processes. These developments can dramatically change the resolvability of a target, and so may change the MRTD performance of an imaging system. This type of electronic processing has accompanied the increased use of automatic target recognition (ATR) devices, and may eventually require a different and more objective figure of merit than MRTD to evaluate the performance of imaging systems. However, until MRTD is superseded, the modeling of electronically processed data remains a difficult proposition.

A final and continuing concern for second generation MRTD modelers is the performance of the eye/brain system. The various methods used to date, i.e. the matched filter response, or the synchronous integrator model, should be brought into question. This aspect of the entire image resolution process seems to be the most important, yet the least understood. Without an accurate and precise model of the display/observer interaction, the accuracy of the entire system model is compromised.

IV. EXPERIMENTAL DESIGN AND MEASUREMENTS

The literature contains several experimentally measured MRTD curves [Refs. 1,15,16, and 28]. Additionally, many papers presenting models give an MRTD 'trend' curve, used to predict MRTD trend performance as a function of spatial frequency [Refs. 3,9,10,14, and 28]. Unfortunately, many of the MRTD measurement curves differ by as much as an order of magnitude [Refs. 3,15, and 28]; and many of the trend curves do not include scaled axes [Refs. 14,15, and 16]. To measure the success of the VISMODII model developed in Chapter V, and compare its results to the other MRTD prediction models available, it was desirable that a set of measurements be taken in our own laboratory. These measurements would not only give a set of data to compare to the predictive results of the various models, but also would give a better 'feel' for the accuracy and reliability of MRTD measurement data reported in the literature. A second purpose for the laboratory measurements was to perform a set of objective signal to noise ratio measurements that could be used in the development of an objective MRTD. These 'objective' measurements would simulate a simple ATR system. This data is incorporated in the VISMODII model in the next chapter.

Although conducted in a laboratory environment, these tests may be more appropriately termed 'field tests' because of the limited precision of measurement equipment available and the lack of positive control over the laboratory environment. Two staring focal plane array imaging systems were utilized. The first, an Amber Engineering AE4128, was a 128x128 staring focal plane array of InSb detectors. The second imaging system used was a Mitsubishi Electronics IR-M500 model, incorporating a 512x512 staring PtSi array. The first objective of these laboratory measurements was to measure the MRTD for the two systems, and compare the results to those predicted by the FLIR92 and VISMODII models. This chapter describes the experimental setup and methodologies, describes the imaging systems used, and gives the measured MRTD data. The MRTD results are compared to predictions obtained from the FLIR92 and VISMODII models in

Chapter VI. The second objective was to conduct the objective signal to noise data. The data measured is presented in this chapter, and discussed at greater length in Chapter V.

A. EXPERIMENTAL SETUP

The experimental setup is shown in Fig. 4.1. The target scene consisted of a correctly scaled standard four bar test pattern against a uniform background. The target apparatus is shown in more detail in Fig. 4.2. The target apparatus consisted of a heated back plate and a cooled front plate. The four bar pattern was cut through the front plate, allowing the imager to view the heated back plate through the four bar pattern. To the imager, the front plate provided the uniform (cool) background, while the back plate, viewed through the pattern represented the (hot) target. Thermocouples mounted on the front surface of both allowed the temperature difference to be read directly. Both plates were made of shot-blasted aluminum, painted in a non-reflective flat black to ensure uniform emissivity. The back plate was heated by means of an electrical current passing through resistive heating elements mounted on its back surface.

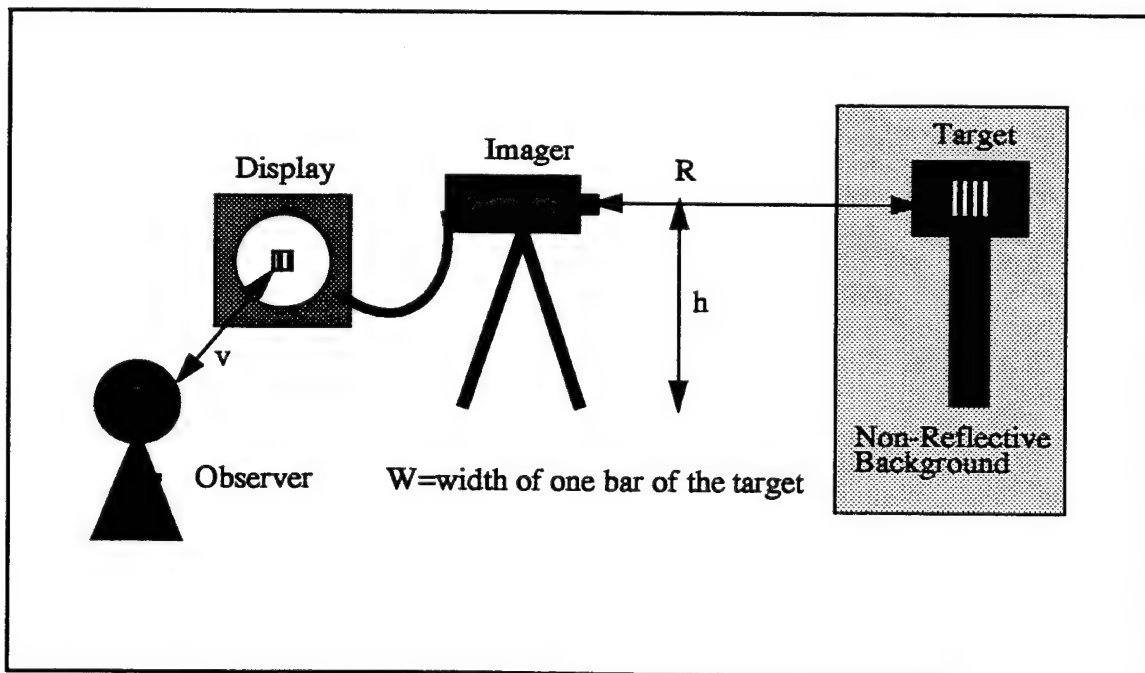


Figure 4.1. Laboratory setup for MRTD measurements

Back plate temperature was controlled by adjusting the amount of current provided to the resistive heating elements. Front and back plates were separated by 10 cm so that the front plate temperature remained near the ambient temperature. Both front and back plates were made of aluminum to provide high thermal conductivity and temperature uniformity on the surface visible to the imager. The target platform was placed at the prescribed distance from the imager in a non-reflective environment in order to minimize reflected radiation from other emitting objects in the room. All measurements were made at an ambient room temperature of approximately 295K.

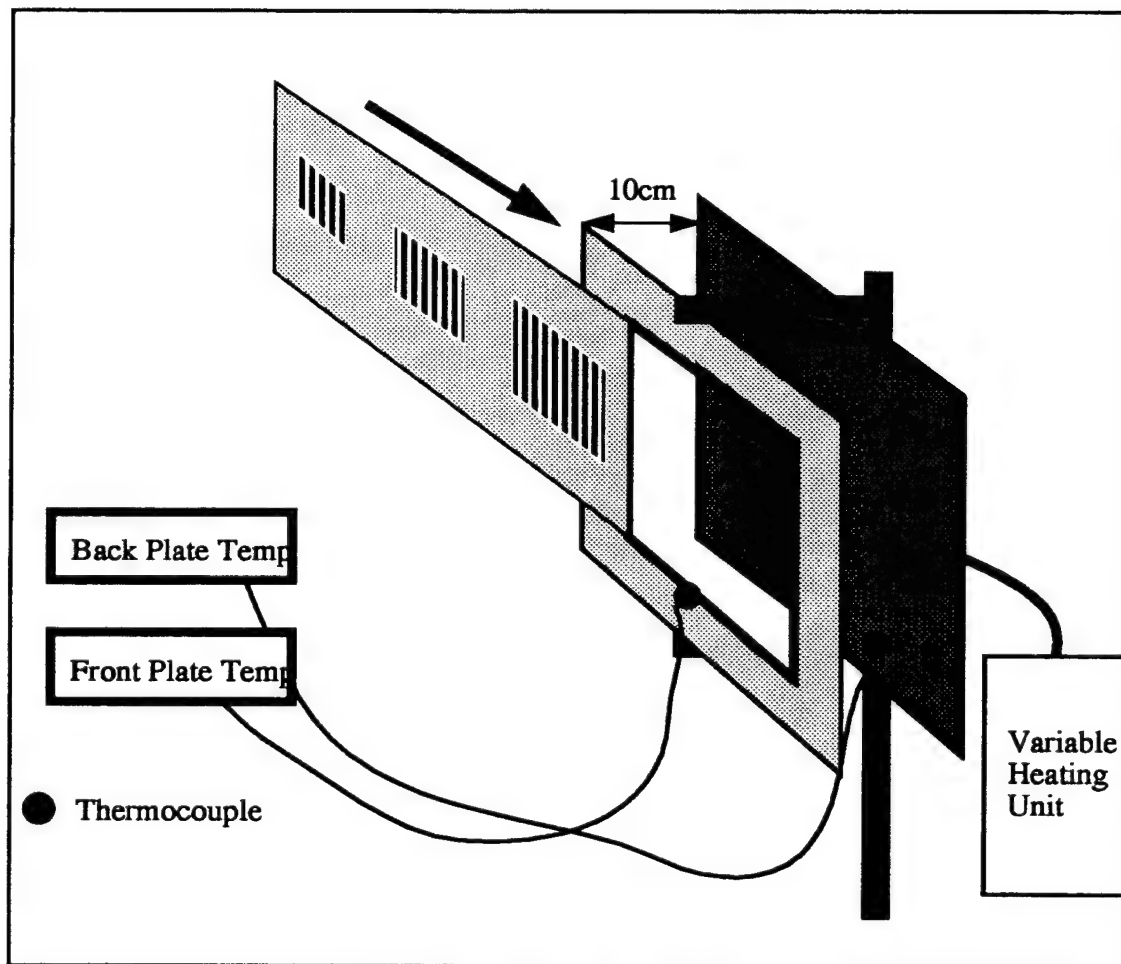


Figure 4.2. Target apparatus

Nominal spatial frequencies were determined by the size of the four-bar pattern, and the distance from the imager to the target. As shown in Fig. 4.2, the front plate set consisted of a fixed template, over which a second plate with several different size patterns was slid. In each case, the bar height was seven times the width of one bar (i.e., $7W$), corresponding to the accepted standard. Referring to the dimensions illustrated in Fig. 4.1, nominal spatial frequency is given by:

$$f_x = \frac{R}{2W} \quad (4.1)$$

where W is the measured width of one bar and R is the distance from the target to the imager. The imager input aperture lens was placed at target height, h , and the target plate fronts were aligned perpendicular to the front plane of the imager. Proper alignment eliminated off-axis effects, and ensured a 'clean' image was viewable by the imager. Since the measurement apparatus and the imager were necessarily static, camera and target motion effects could not be included in this set of data. The MRTD measurements thus obtained are static performance measurements, implying that the observer knows where and when to look for the pattern. This is consistent with the static nature of most laboratory models presented in the literature.

B. EXPERIMENTAL METHOD

The actual measurement process was conducted as follows. Prior to data measurement, the observers were trained in the recognition criteria. For these measurements, the target was called 'resolved' when it could be discerned that it consisted of four bars. This requirement that all four bars could be fully discerned corresponds to a probability of correct identification of 100%. This differs slightly from some other test methodologies in which a 50% detection probability is used in measuring the MRTD [Refs. 1,16]. In the 50% methodology tests, the MRTD is taken to be the temperature at which half of the observers could resolve the pattern and half could not. The 100% detection methodology has intuitive appeal because it reduces the great variance in

measurements obtained from several observers when the 50% methodology is used in the presence of noise [Ref. 28]. Standard measurements indicate that a 50% probability of detection corresponds to an SNR threshold of about 3.0; while a 100% detection probability corresponds to an SNR of about 6.0 [Ref. 28]. The validity of these values is confirmed by Lloyd, who places a 90% detection SNR threshold at 4.5 [Ref. 3]. These differences in detection methodologies, then, can be easily incorporated in predictive models by adjusting the threshold SNR used in the MRTD calculations.

Preparations for measurements included optimizing the imager's f-stop, focus, and alignment to ensure optimal response. The pixel non-uniformity correction process for the imager was then run, followed by a calibration. The room was darkened, and the monitor adjusted by the observer to optimize viewing conditions.

Measurements were conducted in both directions of the heating/cooling cycle. One set of data was taken as the back plate was heated up from below to above the resolvable threshold. The second set was taken as the back plate was cooled from above to below the resolution threshold. In each case, the observer watched the display until he could resolve the four bar pattern (in the first set) or could no longer resolve the pattern (in the second set). At the minimum resolution point, the surface temperatures of the back and front plate were recorded. The difference between the temperatures is the MRTD. The spatial frequency of the test pattern was then changed, and the process repeated. The measurements were then averaged between observers, trials, and heating/cooling cycles to give one set of data points of MRTD as a function of spatial frequency.

In order to obtain a complete evaluation of available models, the process was repeated in both the horizontal (bars oriented vertically and spaced horizontally) and vertical (bars oriented horizontally and spaced vertically) directions. The results were analyzed separately and also added in quadrature to give a composite two dimensional MRTD figure in the same manner that is accomplished in the FLIR92 model given in Appendix C.

C. SYSTEM PARAMETERS

The two different imaging systems used had unique properties that changed the nature of the measurement data sets. In both cases, the goal was to optimize the MRTD performance of the imager/observer system without introducing processing artifacts that could not be included in the predictive models. Complete system parameters are contained in Appendix A, and a brief description of each system is provided in this section.

1. AMBER System

The AE4128 consists of a camera assembly and a supporting electronics assembly. It operates in the 3-5 μm wavelength band, with a 128x128 InSb staring array. Display is made on a standard computer monitor, which can provide gray-scale shading or pseudo-color. The system is shown in Fig. 4.3.

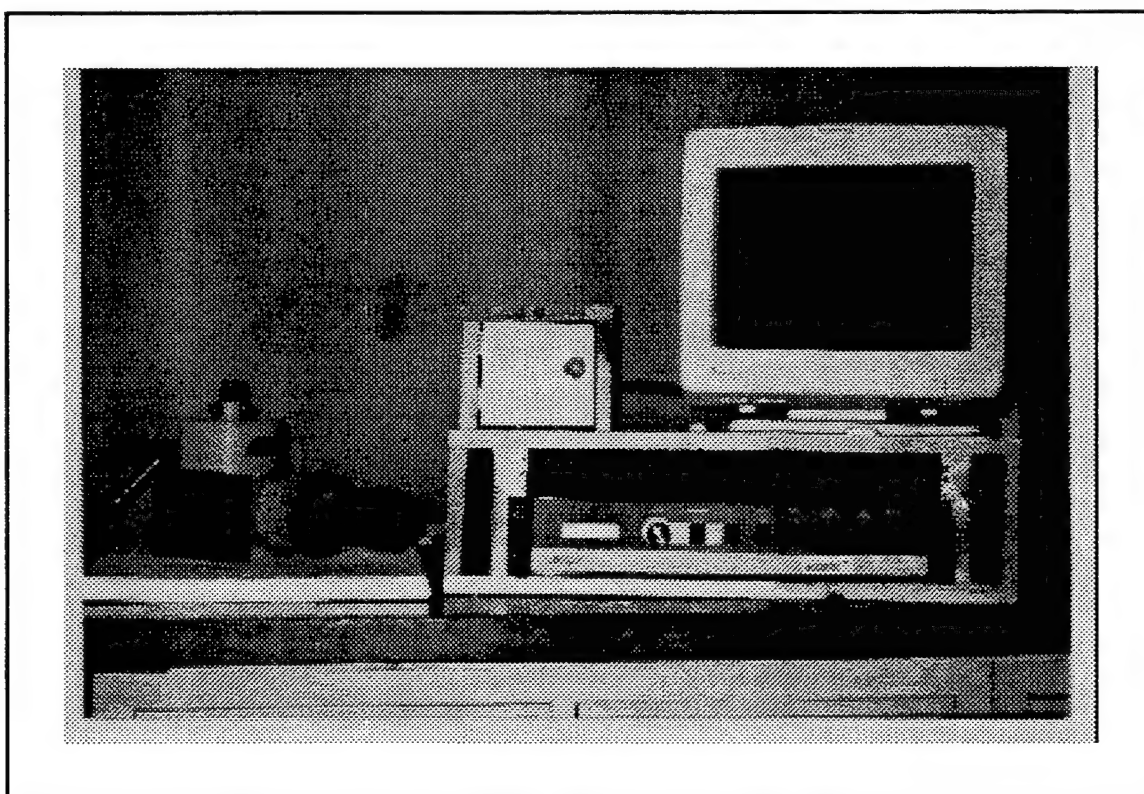


Figure 4.3. The AMBER Engineering AE4128 system

The camera assembly contains the imaging optics, the detector array, and a cryogenic dewer which must be filled with liquid nitrogen to maintain a detector temperature of around 77 K. The dewer must be evacuated to less than 10^{-4} torr in order to prevent condensation on the detector and to prevent rapid loss of liquid nitrogen. The imaging optics include a 2 inch CaF_2 optical window that provides 95% transmittance in the 3-5 μm band. Although the requirement to provide a vacuum enclosure and cryogenic cooling of the camera assembly is somewhat cumbersome, the electronic processing unit gives the system a great deal of flexibility. The electronics assembly includes the necessary drive electronics, as well as a pixel non-uniformity correction circuit, scalable amplifiers, and a micro-controller. The device has the capability to provide RS-170 analog video output, perform two-point nonuniformity correction on the individual detectors that make up the array, and (optionally) auto-calibrate global gain and offset. Additionally, it gives the operator the ability to control all clocks, frame rates, and integration times. A parallel digital interface for real time external processing of the FPA outputs is also available [Ref. 38]. In addition, the monitor itself has the standard brightness and contrast controls. To eliminate as many artificial processing artifacts as possible, these capabilities were manually controlled when possible. Global gain was set to one. Global offset, which is analogous to AC coupling of a scanning system, was adjusted to give optimal contrast between target and background. Frame rate and integration time are expressly accounted for in the predictive MRTD models. The two point calibration capability was utilized in order to automatically minimize pixel non-uniformities. This routine takes measurements at two uniform temperatures (a hot lens cap and a cold lens cap) and adjusts pixel nonuniformities by gain compensating the output of individual detectors. The observer was allowed to adjust display brightness controls to optimize viewing. The observer was also allowed to adjust his position in order to optimize viewing angle, and eliminate any sample scene phasing due to eye position.

2. Mitsubishi Electronics System

This system is a conveniently packaged unit that does not require an evacuated chamber or external cryogenic cooling. The Mitsubishi camera contains a cryogenic Stirling cycle cooler to provide detector temperature control, operating at around 80 K. It also operates in the 3-5 μm band, with a 512x512 PtSi array. This unit contains many of the automatic features of the AMBER system, but does not allow for operator manual control. Instead, the unit is almost completely automatic and self-contained, with only a palm-sized wired remote controller. The system is pictured in Fig. 4.4. Although some information is provided in the user's manual [Ref. 40], most of the technical specifications listed in Appendix A were obtained from Mitsubishi America in Cypress, CA [Ref. 41].

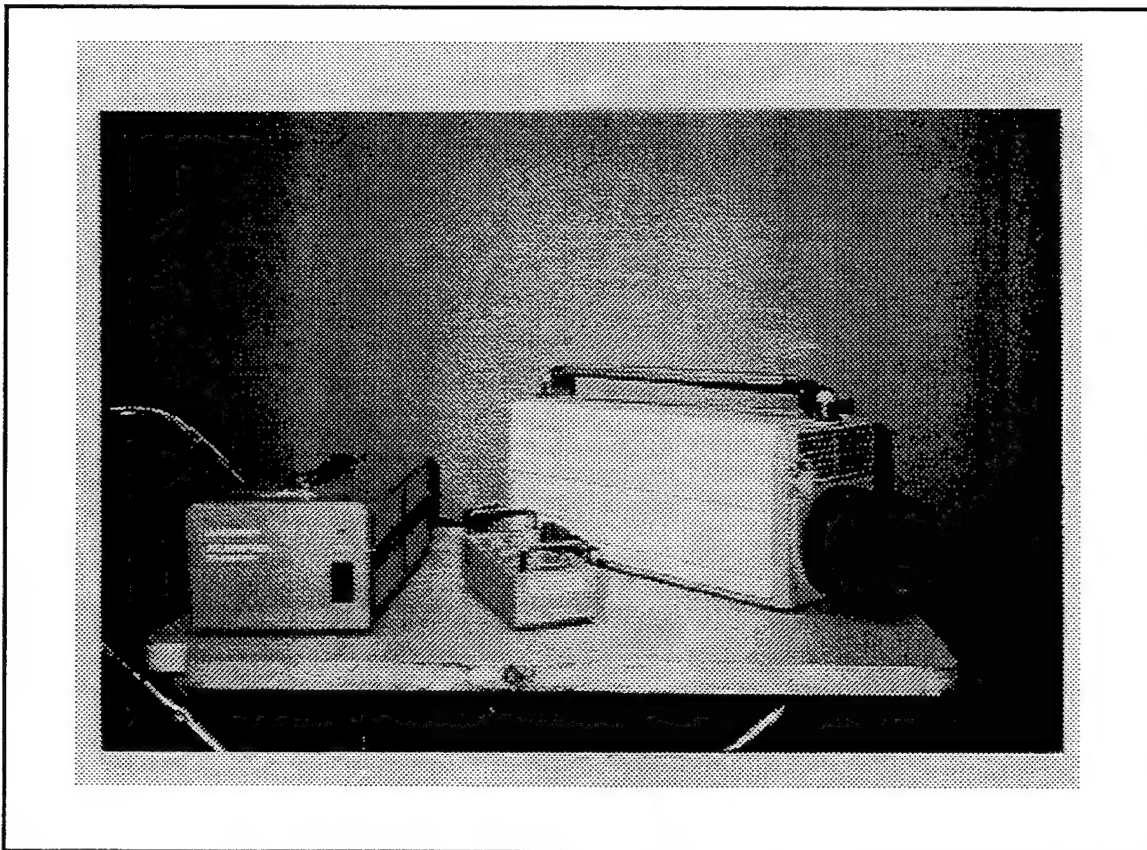


Figure 4.4. The Mitsubishi IR-M500 system

D. MRTD MEASUREMENT RESULTS

The average MRTD measurement data is provided here in graphical form for both horizontal and vertical MRTD's for both the Amber and Mitsubishi systems. Complete measurement results are provided in Appendix D in tabular and graphical form. Figure 4.5 portrays the average measured MRTD's for the Amber system. Figure 4.6 shows the average measured MRTD's for the Mitsubishi system. Figures 4.7 and 4.8 present the same data on a logarithmic scale. This data is compared to predictions from FLIR92 and VISMODII in Chapter VI. There are several trends notable from these results, and each is discussed in the paragraphs that follow.

First, each system MRTD seems to approach the low frequency limit at an asymptotic value that is greater than zero. This trend serves as the motivation for the visibility method used in VISMODII, described in the next chapter.

Second, there is a measurable difference in recorded values for the horizontal and vertical MRTD values. This is attributable to the different values of system MTF in the two directions, and possibly to the difference in converted temporal frequency between vertical and horizontal cells caused by the clock-out process, as described in Chapter I.

Third, there is a marked difference between measurements taken as the back plate is heated up past the MRTD and measurements taken when the back plate is cooled down below the MRTD. This trend is noticeable in both the Amber and Mitsubishi tests conducted, and may indicate a perception factor or eye/brain process whereby an image is easier to track as it fades after it has already been resolved by the observer than it is to recognize a new image appearing out of noise.

Fourth, there is the obvious trend that the MRTD rapidly increases above a particular value of spatial frequency. This matches the trend present in most measured and predicted data [Refs. 1,3,15, and 28].

Fifth, the Mitsubishi system performance was approximately twice as good as the Amber, even more so at low spatial frequencies. This is probably because of the larger array size and greater resolution of the Mitsubishi system.

Sixth, for the Mitsubishi imager, the vertical MRTD is higher than the horizontal MRTD. This is noticeable in the Amber system as well, to a lesser extent. This suggests a difference in the array clock out process which manifests itself as a contrast degradation in one direction more than the other.

Finally, the low frequency asymptotic value is different for the two systems, suggesting a system dependent threshold temperature difference that can be resolved in the low frequency limit. This threshold could conceivably be predicted from device parameters.

Measurement precision for these tests was unavoidably poor, and is valid to within 0.0556 Celsius (0.1 degrees F). This was the tolerance of the thermocouples used to measure the plate temperatures and the thermocouple read out displays.

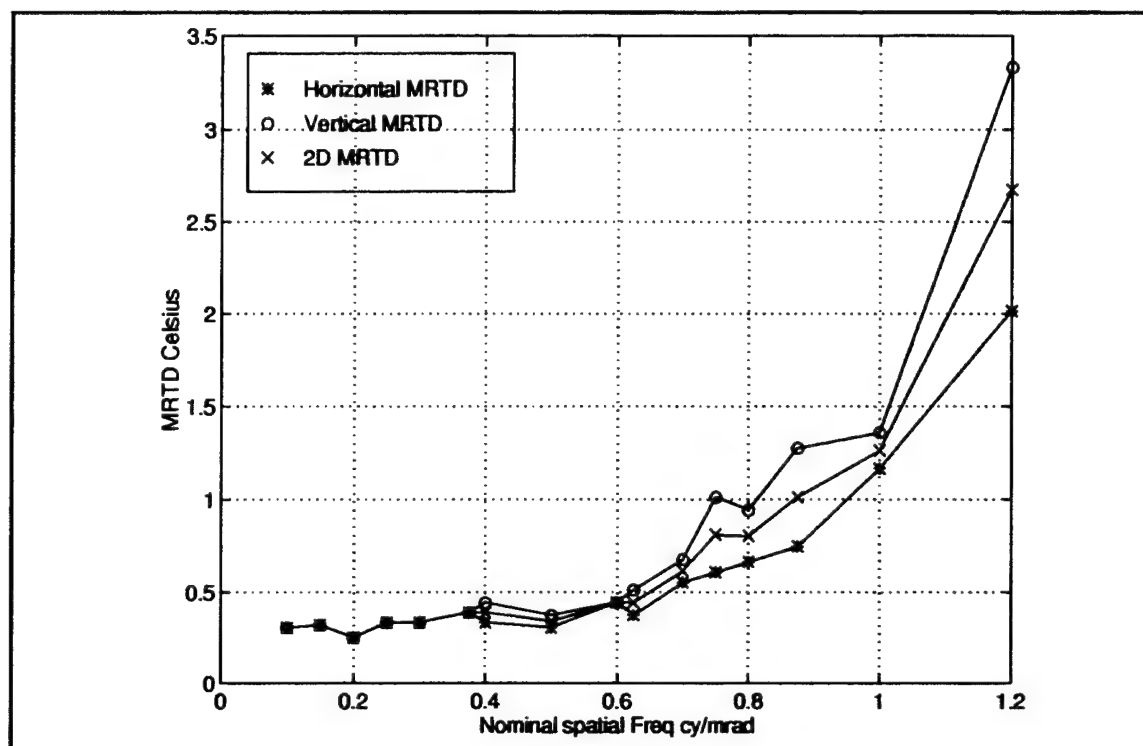


Figure 4.5. Average MRTD measurements for the AMBER system

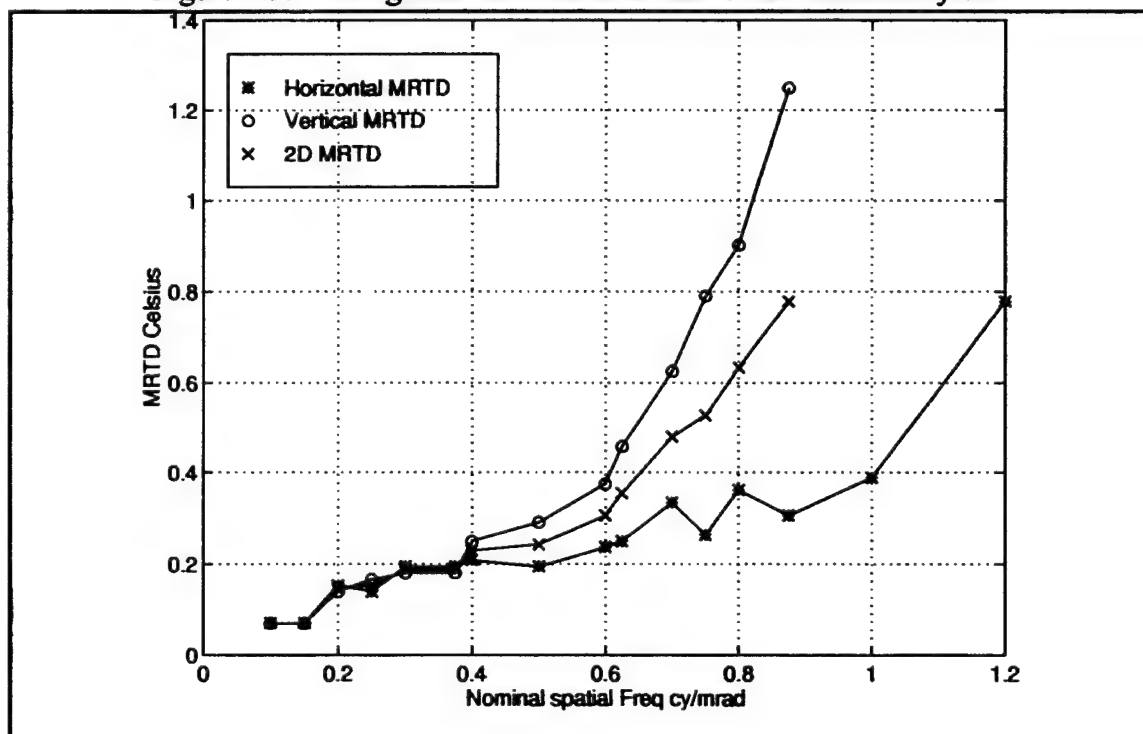


Figure 4.6. Average MRTD measurements for the Mitsubishi system

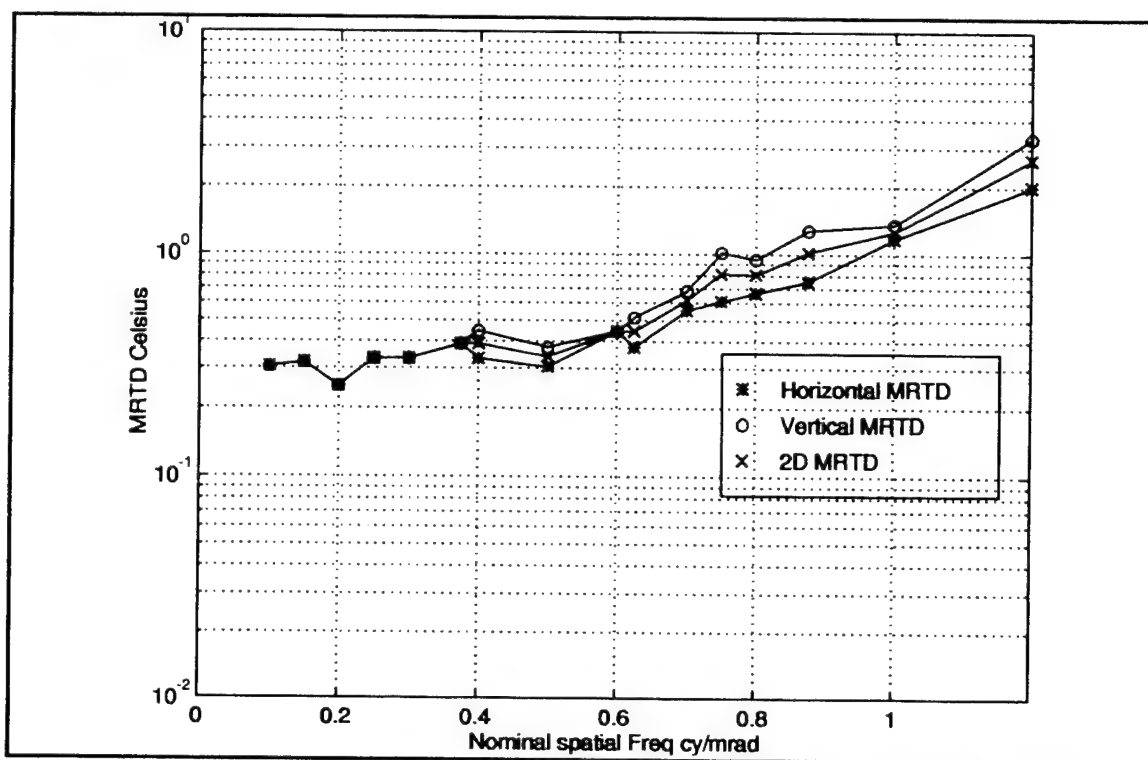


Figure 4.7. Average MRTD results for the AMBER system, logarithmic scale

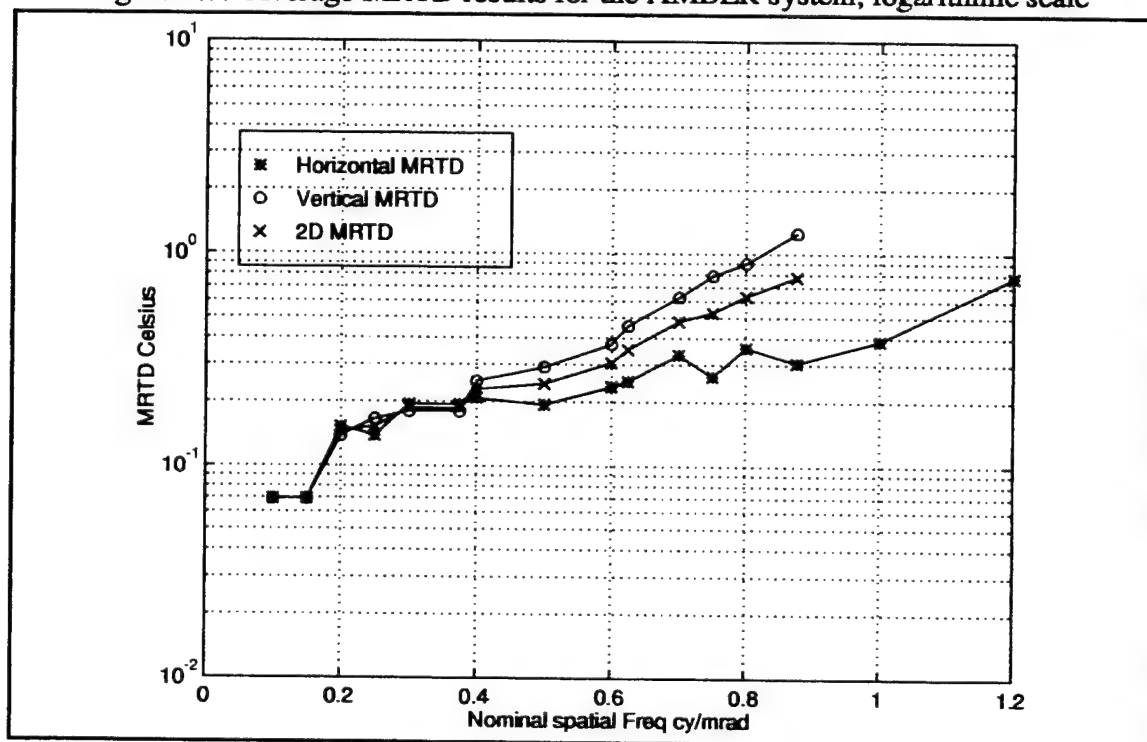


Figure 4.8. Average MRTD results for the Mitsubishi system, logarithmic scale

E. OBJECTIVE MRTD MEASUREMENTS

As discussed in Chapters I and III, there are several concerns regarding the continued use of the MRTD as a figure of merit for second generation systems. The fundamental drawback of the MRTD is its dependence on a human observer to subjectively interpret the 'resolvability' of a given scene. The lack of objectivity and repeatability of this type of measurement was clearly demonstrated in our own MRTD measurements as well. In order to explore the feasibility of an objective measurement of resolvability, some additional measurements were made. It is hoped that this data, although very simple in nature, can motivate the development of an objective MRTD standard.

The use of an electronic ATR device implies that the resolvability of the target must be objectively discernible from the electronic signal and noise of the target scene. To simulate a simple ATR system, an oscilloscope (Tektronix model number 468) was inserted into the measurement process as shown in Fig. 4.9. The oscilloscope serves as the simplest of ATR devices, measuring only the SNR of the imager's output signal. The Mitsubishi system was used for these measurements.

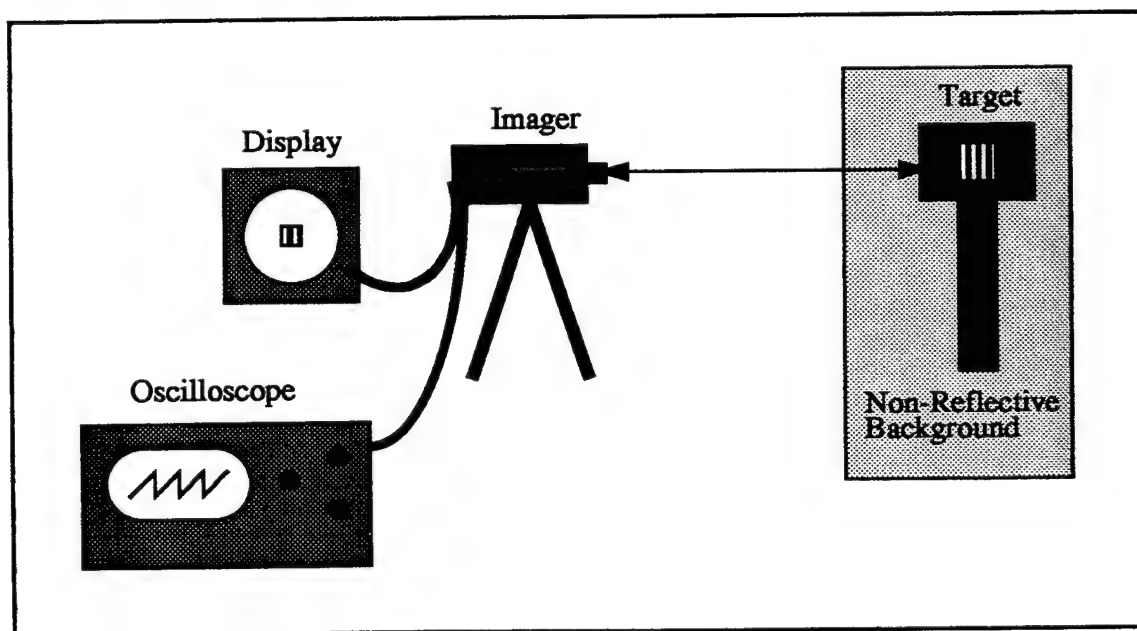


Figure 4.9. Automatic target recognition simulation setup

Three simple measurement tasks were accomplished with this setup. First, the SNR measured by the oscilloscope was held constant as the spatial frequency of the target was varied and the temperature difference between target and background was measured. An SNR of 6.0 was chosen, corresponding to a 100% probability of detection, and matching that of the previous MRTD measurement tests. The SNR measurement is demonstrated in Fig. 4.10. In the figure, the signal corresponding to the four bars of the target pattern is clearly visible. The oscilloscope display was synchronized to one line of video that passed through the bar pattern. Figure 4.10 shows one tenth of the length of a single scan line, the portion that contained the bar pattern. The variance of the noise present in the system output is apparent as well.

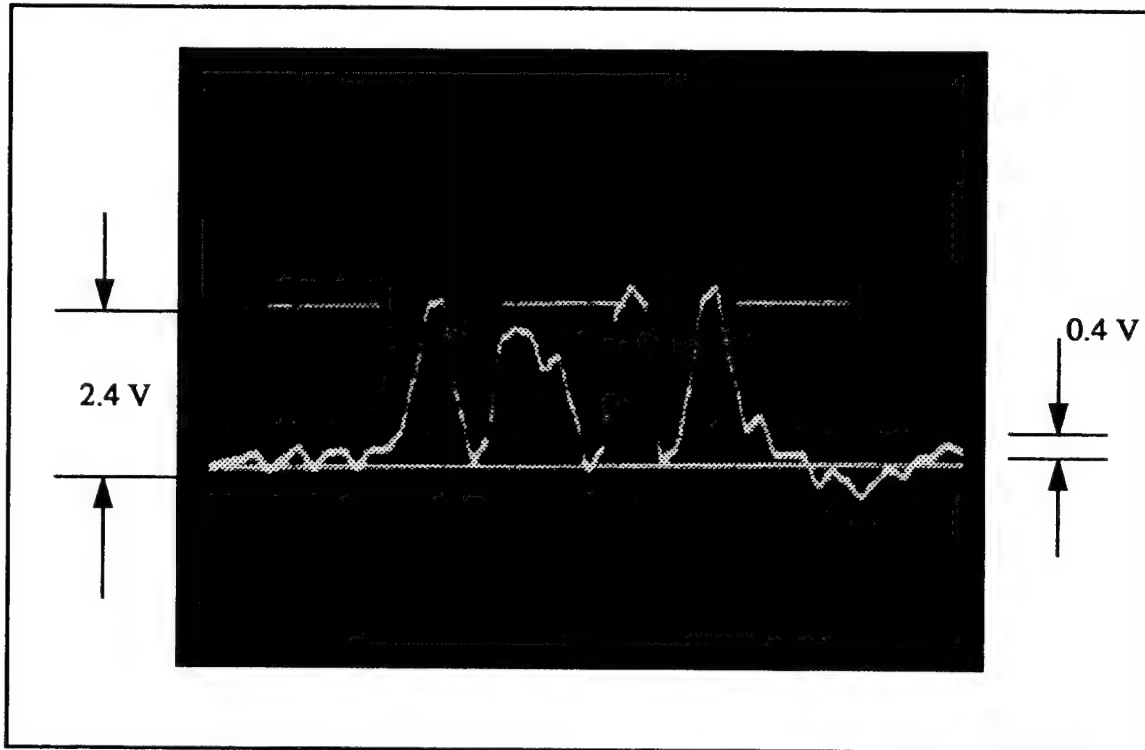


Figure 4.10. Measurement of SNR from oscilloscope data

Second, the temperature difference between target and background was held constant as the spatial frequency was varied and the SNR was measured. The temperature difference used was 3.5 Celsius, to ensure adequate signal levels for the full range of spatial

frequencies used. Third, the spatial frequency of the target pattern was held constant, as the SNR was varied and the temperature difference was measured. A mid-range spatial frequency of 0.5 cy/mrad was used.

The three sets of measurement data are plotted as Figs. 4.11, 4.12, and 4.13. The data is presented in tabular form in Appendix D. It was clear from these measurements that the human eye is a fantastic device for picking a signal out of noise. To achieve an objectively measured SNR of 6.0, which corresponded to MRTD in the subjective measurement case, it was necessary to increase the temperature difference a great deal beyond that required to resolve the four bars on the monitor. In this case, the signal was not discernible in the oscilloscope display until it was well past minimum resolvability on the monitor display. This perhaps explains the reluctance to let go of the human perception element in a resolvability standard, as an ATR that can match human performance would be difficult to build. The use of this data in the development of an objective MRTD is discussed in the next chapter.

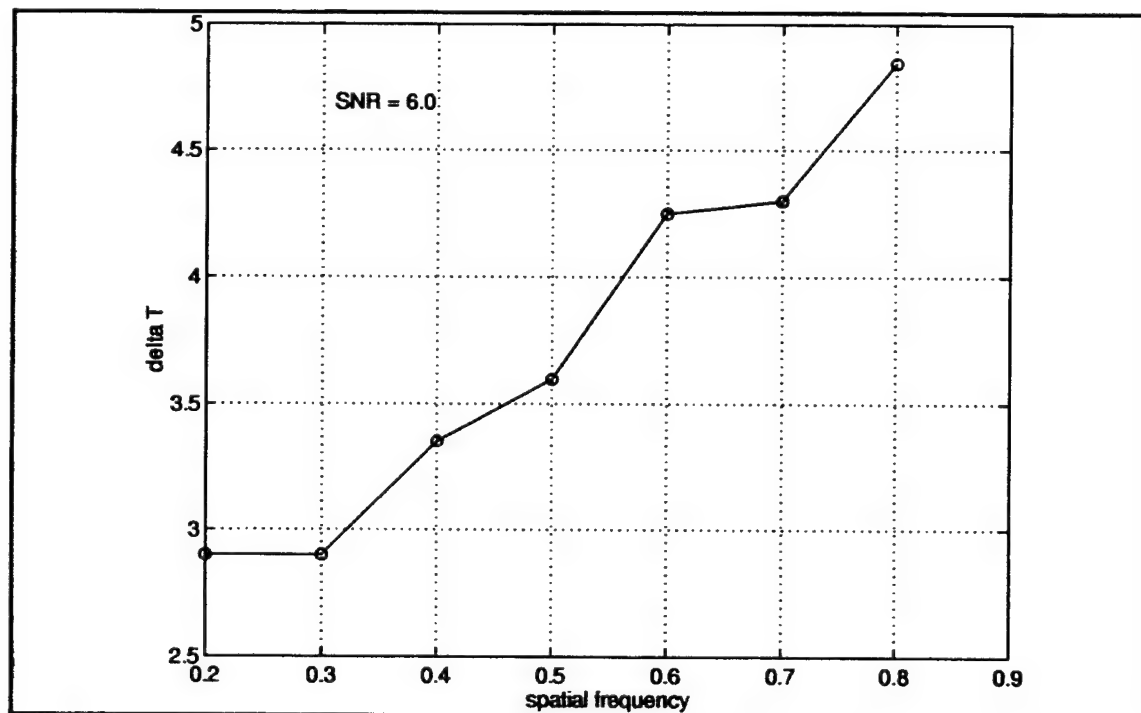


Figure 4.11. Temperature difference vs. spatial frequency for constant SNR

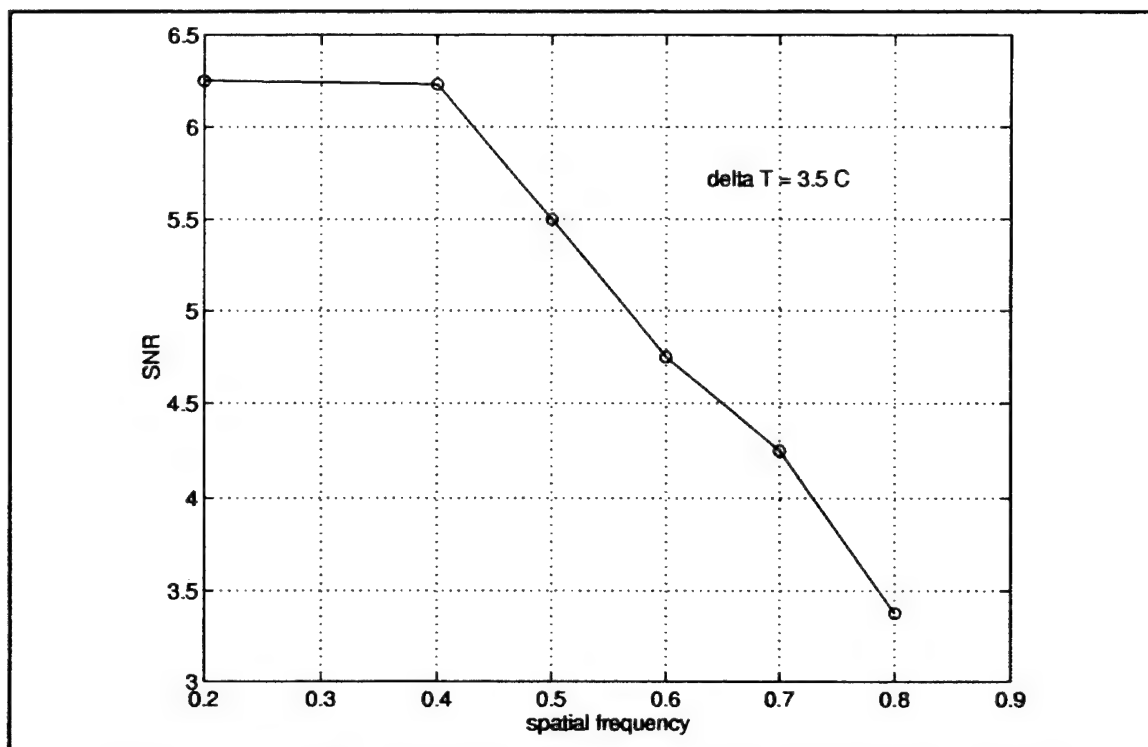


Figure 4.12. SNR vs. spatial frequency for a constant temperature difference

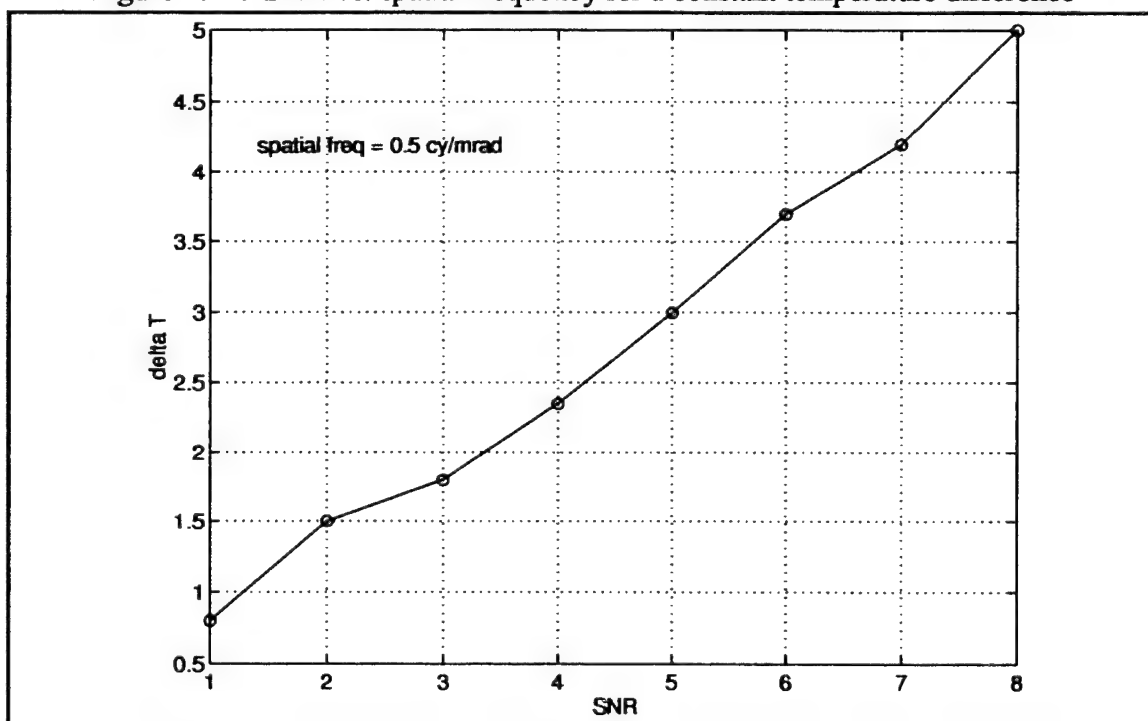


Figure 4.13. Temperature difference vs. SNR for constant spatial frequency

V. SECOND GENERATION VISIBILITY MODEL

The proper modeling of second generation staring arrays is an elusive task.

Although second generation models exist, they are mainly direct descendants of first generation linear models with the addition of a correction factor to account for directional noise effects. Staring array imagers are so different in their operation that it is optimistic to expect these first generation models to produce accurate MRTD predictions [Ref. 39]. One of the disadvantages of a second generation model derived from the first generation is its dependence on a subjective MRTD. As discussed in the literature [Refs. 8,25,39] and measured in the laboratory (Appendix D), the subjective MRTD has disadvantages as a figure of merit. In particular, the unrepeatability and wide variance in measurement results of the MRTD, and the widespread development of automatic target recognition (ATR) devices make it desirable that a model could incorporate an objective measure of resolvability [Ref. 9]. However, because current state of the art ATR devices cannot match the performance of the human eye in resolution tasks, the new model should also be able to make subjective MRTD predictions for human observer systems.

The concepts that serve as the foundation for the first generation visibility model, presented in Chapter II, are compatible with the goal of supporting both an objective and subjective MRTD. Since the visibility model makes no assumptions about the observation process, it is applicable to the case where the observer is not a human being at all. Applying the visibility concepts to the unique problem posed by staring array imagers is the basis for the second generation visibility model, VISMODII. The VISMODII has been developed to allow the incorporation of directional noise effects, sampling/aliasing effects, scene phasing effects, and non-zero PTF's, within the framework the visibility model provides. The model developed extends the applicability of an MRTD predictive model into the region beyond the nominal system Nyquist frequency, includes fixed pattern noise effects inherent in staring array systems, and supports both subjective and objective resolvability criteria. Because of the simplicity of concept but completeness of the model, it could serve

as a valuable predictive model for a wide range of thermal imaging systems, and as a platform for the further development of an objective resolvability standard.

A. VISMODII OVERVIEW

The first generation visibility model presented a new method for prediction of MRTD performance based on a threshold resolvable contrast, and a one-dimensional contrast reduction parameter derived from the spatial frequency limited performance of TIS sub-systems. The motivation for this concept was provided by both measured MRTD results, and by the standard mathematical formulation of MRTD as given by Eq. 3.5. These two items suggest the formulation of MRTD as the product of two factors; one frequency dependent, the other not; as in Eq. 2.18. The visibility model had three distinct advantages over other first generation predictive models. First, it was much simpler and had intuitive appeal because it did not rely on a precise modeling of the eye/brain resolution process. The conflict of matched filter response versus synchronous integrator response for the eye/brain system was avoided. Second, it could readily incorporate non-zero phase transfer functions (PTF's) in the MRTD prediction. Finally, it had better correlation with measured results than other first generation models.

The problems of fixed pattern directional noise, aliasing, and scene phasing, as presented in Chapter III, must also be addressed in predictive models for staring arrays. Other second generation models have addressed these problems by 'patching up' first generation models with one or more directional correction factors. These attempts appear to be inadequate for accurate prediction of performance for staring FPA's, because they discount the unique aspects of second generation imaging systems [Refs. 4,23,39]. These unique aspects include sampling effects in two dimensions, useful resolution information provided beyond the nominal system Nyquist frequency, and scene phasing effects. In addition to not including the above effects, the accuracy of the various ad-hoc perception factors, eye/brain models, and spatial/temporal integration factors has been called into question [Refs. 9,16,39]. The very simplicity of the visibility model concept serves well

in this regard. The second generation modeling considerations of Chapter III can easily be incorporated into the concepts of the visibility model without including elaborate underlying assumptions.

1. VISMODOII Modeling Concepts

This sub-section provides a brief overview of the VISMODOII. The derivations of the quantities that appear here are found in later sections of this chapter. As in the first generation visibility model, VISMODOII suggests a form for MRTD such as:

$$\text{MRTD}(f_z) = \text{MRTD}(f_z \rightarrow 0) \times \frac{1}{\alpha(f_z)}, \quad (5.1)$$

which includes a low frequency limit term for MRTD, modified by the $\alpha(f_z)$ term which is defined as the contrast transference parameter. As indicated by the subscript 'z', this representation can be applied in either horizontal or vertical directions. In the low frequency limit, the bar pattern is assumed to appear as a step function within the field of view. Ultimately, in the low frequency limit, the application of resolution enhancing perception factors is inappropriate as integration over the entire bar pattern does not take place [Ref. 9]. The VISMODOII, in consonance with measured data, but unlike other predictive models, assumes that there is a non-zero threshold minimum input contrast that can be resolved in the low frequency limit. This value, denoted as ΔT_{sc} , is system and observer dependent. It could, as appropriate, denote the minimum contrast resolvable by a human observer or, separately, the minimum contrast resolvable by an ATR device. This term inherently contains all of the observer and system noise effects without making assumptions about their nature. So, one imaging system could have multiple thresholds for different types of observers.

The contrast transference parameter, $\alpha(f)$, includes all frequency dependent contrast degradation of the system. VISMODOII includes two dimensional aliasing and scene phasing effects for sampled imaging systems such as FPA's in the formulation of the

contrast transference parameter. Thus, the two dimensional effects of aliasing and blurring are included in this one parameter.

Figure 5.1 shows the salient features of VISMODII. As shown in the figure, a two dimensional four bar spatial image input will experience a contrast degradation in both dimensions due to the blurring effects of the TIS sub-systems and an aliasing effect due to sampling by the detector array geometry. The net result is that a rectangular, high contrast input function appears at the display point as a 'smoothed-out' image with degraded contrast. Referring to the quantities shown in Fig. 5.1, the contrast transference for a particular target spatial frequency is defined as:

$$\alpha(f) = \frac{\Delta T_s(f)}{\Delta T} . \quad (5.2)$$

It is the proposition of VISMODII that the relationship between MRTD and ΔT_{sc} for a range of target spatial frequencies can be given by:

$$\text{MRTD}(f) = \frac{\Delta T_{sc}}{\alpha(f)} . \quad (5.3)$$

The particular formulation of both the threshold input contrast and the contrast transference parameter are provided in subsequent sections of this chapter.

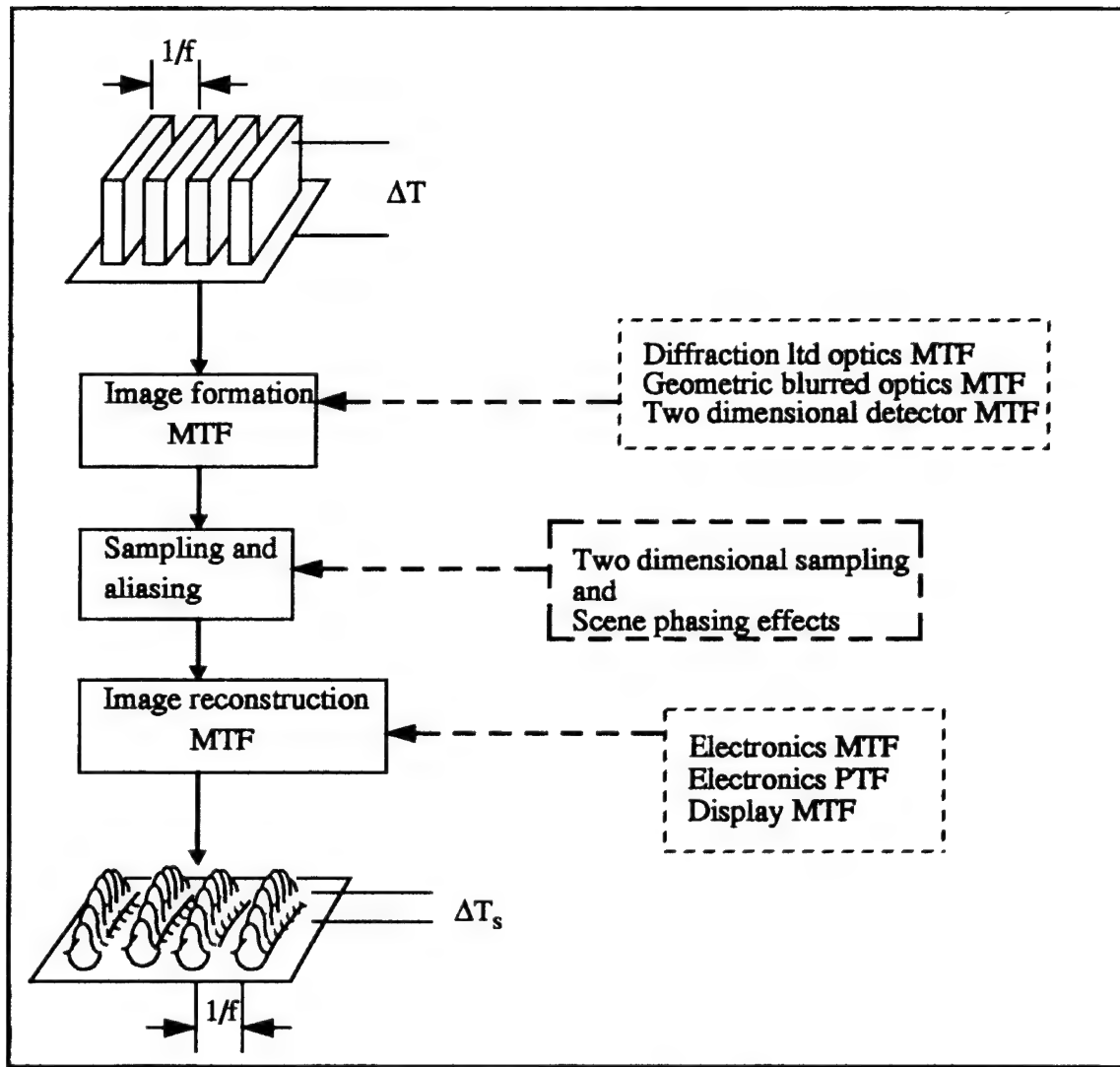


Figure 5.1. Salient features of VISMODOII

2. Second Generation Visibility Model Enhancements

Figure 5.1 also makes clear some of the differences between the first and second generation visibility models. The most obvious difference is that VISMODOII operates on an exact two dimensional fast Fourier transform (FFT) of the four bar target. The first generation visibility model approximated the target pattern as a one dimensional square wave, that was further divided into individual sinusoidal components. Since the spectrum used in VISMODOII is exact, there is no estimation error introduced.

Formulation of the various MTF's and PTF's also differ between the two models. VISMODII contains some more sophisticated sub-system transfer functions. This change may enable more precise modeling of actual sub-systems, but does not change any of the salient features of the model.

Two dimensional sampling and aliasing effects are included in VISMODII. In real systems, significant resolution information is often available even in the presence of aliasing effects. VISMODII uses system specific sampling information to extend the concept of resolvable contrast beyond the Nyquist limit of the system.

Sample scene phasing effects are properly included in the analysis as part of the aliasing subroutine. This is possible because the complex values of spatial frequency domain quantities are retained in the analysis, allowing the easy introduction of scene phasing effects.

The heuristic prediction for a subjective ΔT_{sc} incorporates directional noise effects, modifying the simple NETD used in the first generation model. Also, an objective ΔT_{sc} is provided based on an ATR simulation as described in Chapter IV. Threshold input contrast can be directly input into the model if it is available by measurement or other means.

Since VISMODII operates in the two dimensional spatial frequency domain, it can include contrast degradation effects in both dimensions of the four bar pattern. It easily calculates both vertical and horizontal MRTD's by rotating the four bar pattern 90 degrees in the analysis. The model could also be upgraded to predict performance at any target angle.

3. VISMODII Programming and Logical Flow

VISMODII is written using the MATLAB high-performance computational software. TIS input parameters for a particular device are loaded at the front end. VISMODII operates primarily in the two dimensional spatial frequency domain where most relevant effects are most easily implemented. The logical flow of the program, and

the domain in which particular calculations take place are shown in Fig. 5.2. The actual MATLAB code used is included in Appendix E.

As previously stated, VISMODII incorporates all frequency dependent effects including aliasing and scene phasing into the contrast transference parameter. The program works on one spatial frequency at a time, and loops through all spatial frequencies of interest to obtain the contrast transference parameter as a function of spatial frequency. Calculating $\alpha(f)$ involves both a linear MTF/PTF analysis and a simulated sampling process, both of which are accomplished in the spatial frequency domain. VISMODII works by creating a four bar target pattern in the spatial domain, and taking its exact two dimensional FFT. As the various spatial frequencies are analyzed, the four bar pattern remains the same, but the axes, MTF/PTF's, and the sampling process are scaled appropriately. VISMODII calculates an image formation MTF which is applied to the FFT of the bar target by multiplication in the frequency domain. Sampling, a two dimensional multiplication process in the spatial domain, is simulated by the convolution of the filtered target spectrum with the FFT of the sampling array. The net result of this process is that the resulting spectrum is repeated at multiples of the sampling frequency in both the horizontal and vertical directions. A second result is the inclusion of an appropriate scene phasing complex exponential which models any misalignment of the target image on the FPA. This aliasing/scene phasing term, and the original spectrum, are multiplied by the image reconstruction filter. The resulting filtered spectrum is then inverse transformed into the spatial domain by the inverse two dimensional FFT. A contrast value is found by a directional averaging process across the bars and troughs of the reconstructed image. This contrast value is modified by an aliasing term calculated by comparing aliased and non-aliased reconstructed images. The contrast value is then combined with the ΔT_{sc} term to give a predicted MRTD curve for the device.

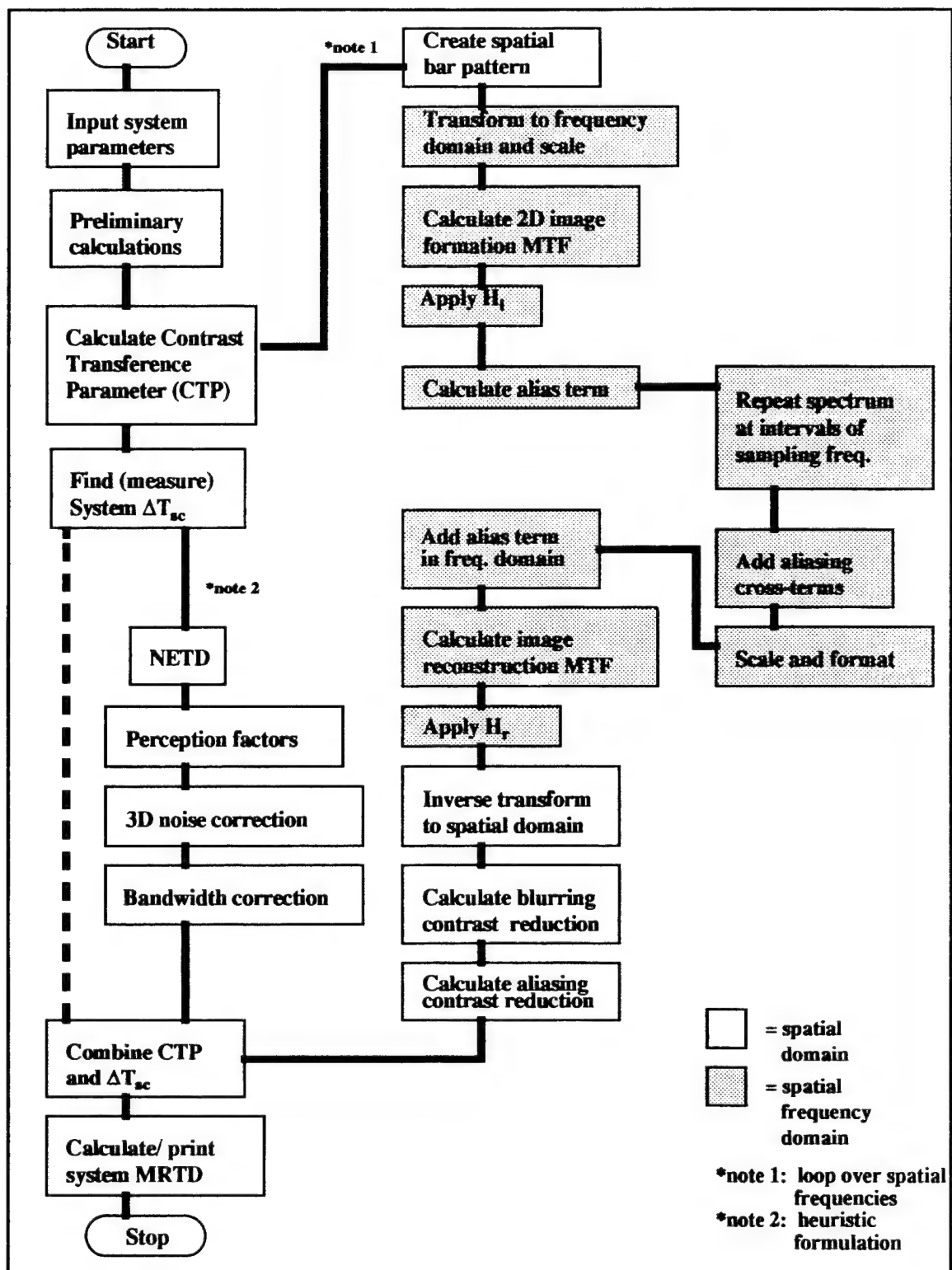


Figure 5.2. VISMODII logical diagram

B. CONTRAST TRANSFERANCE PARAMETER

The most computationally intensive portion of VISMODII is the calculation of the contrast transference parameter. The parameter given by Eq. 5.2 contains all of the frequency dependent contrast degradation effects of the imaging system. In VISMODII it includes both blurring and aliasing type degradations. The blurring effect, caused by the spatial frequency filtering effects of the individual sub-systems, are treated by a linear analysis much like that accomplished in other MRTD models. The sampling/aliasing and scene phasing effects are not common to other predictive models, and will be treated in greater detail in this section.

The determination of a contrast transference necessarily begins with a two dimensional four bar target pattern, a reproduction of which is shown in Fig. 5.3 (resolution of figure reduced for display purposes). An exact two dimensional FFT of the pattern is taken to allow the remaining MTF analysis and sampling simulation to be accomplished in the spatial frequency domain.

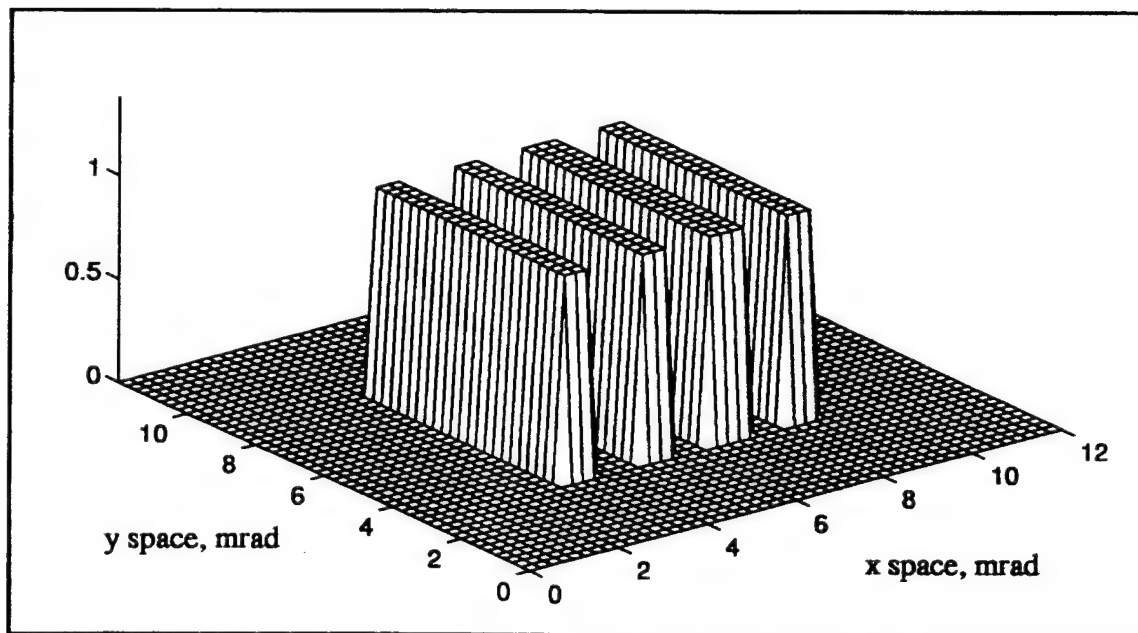


Figure 5.3. Four bar target pattern ($f_x = 0.6$ cy/mrad)

1. MTF/PTF Analysis in VISMODII

The MTF/PTF analysis of VISMODII is accomplished by means of a cascade of sub-system transfer functions. It was desirable to include sophisticated MTF's in the analysis for precision, but not clutter the analysis with multiple complex MTF equations that are nominally set to one in almost every case. Additional MTF's are easily incorporated into the model without changing the salient features. Additional PTF's are also easily introduced because the real and imaginary parts of all variables are retained. Additional MTF's simply accelerate the trend toward a Gaussian system response [Refs. 3,6]. No target/imager relative motion MTF's are included in VISMODII, making it a static performance model. Following the organization of MTF/PTF's presented in the aliasing portion of Chapter III, the sub-systems are divided into two groups. The image formation MTF includes diffraction limited optics, geometric blurred optics, and the detector spatial MTF's. The equations for the four MTF's are given below. Note that because of assumed circular optical geometry, both of the optical MTF's are symmetric in two dimensions, while the detector spatial MTF's may be asymmetrical if the detector geometry is not square.

$$H_{opt}(f) = \frac{2}{\pi} \left(\arccos\left(\frac{\lambda f}{D_o}\right) - \left(\frac{\lambda f}{D_o}\right) \left(1 - \left(\frac{\lambda f}{D_o}\right)^2\right)^{0.5} \right) \quad (5.4)$$

$$H_{ogb}(f) = \exp(-2\pi^2 \sigma_g^2 f^2) \quad (5.5)$$

$$H_{det}(f_x) = \frac{\sin(\pi \Delta x f_x)}{\pi \Delta x f_x} \quad (5.6)$$

$$H_{det}(f_y) = \frac{\sin(\pi \Delta y f_y)}{\pi \Delta y f_y} \quad (5.7)$$

The H_{opt} and H_{det} transfer functions are defined previously. H_{ogb} is a geometric blur MTF used to describe serious aberrations in the system optics. The net image formation filter is given by:

$$H_i = H_{\text{opt}}(f)H_{\text{ogb}}(f)H_{\text{det}}(f_x)H_{\text{det}}(f_y) . \quad (5.8)$$

In the frequency domain, the cascaded MTF's of the image formation filter take a two dimensional shape, centered at spatial frequency coordinates (0,0). The image formation filter for the Mitsubishi system is shown in Fig. 5.4. The familiar 'sinc' function pattern arising from the rectangular detector geometry is clearly seen in the figure.

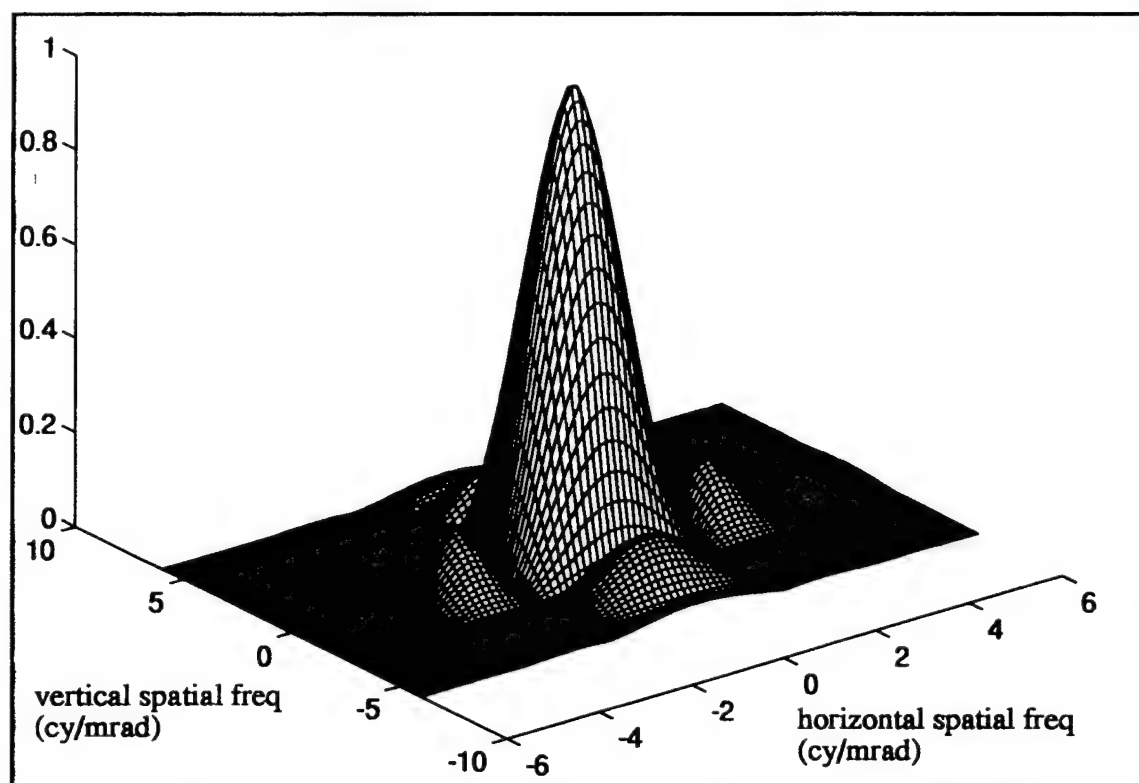


Figure 5.4. Image formation filter for Mitsubishi system

The image reconstruction filter contains all post-sampling processing of the image. The image signal has now been converted to a one-dimensional electrical signal by the detectors. Phase transfer functions may now be introduced by the electronic processing of the post-detector sub-systems. For simplicity, VISMODII includes only the three most significant effects in the reconstruction filter. An electronics MTF, electronics PTF, and display MTF are included. These sub-system filtering characteristics are given by:

$$H_{\text{elect}}(f) = \left(1 + \left(\frac{f}{f_0}\right)^2\right)^{-0.5} \quad (5.9)$$

$$\text{PTF}_{\text{elect}} = -\text{atan}\left(\frac{f}{f_0}\right) \quad (5.10)$$

$$H_d(f) = \exp(-2\pi^2 \sigma^2 f^2) \quad (5.11)$$

The net image reconstruction filter is given by:

$$H_r(f) = H_{\text{elect}}(f)H_d(f)\exp(j\text{PTF}_{\text{elect}}(f))$$

The image reconstruction filter for the Mitsubishi system is shown in Fig. 5.5.

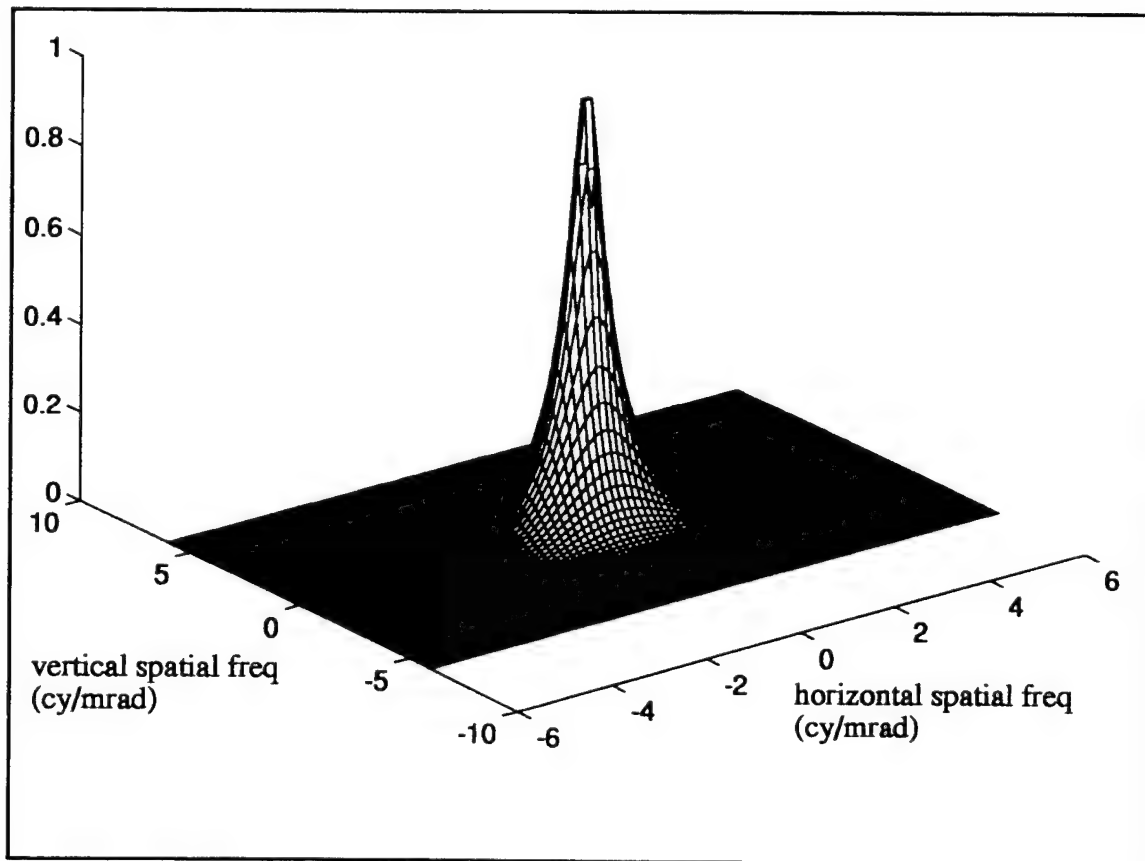


Figure 5.5. Image reconstruction filter for Mitsubishi system

2. Aliasing and Scene Phasing in VISMODII

VISMODII includes aliasing and scene phasing in the predictive model by repeating the filtered target spectrum at intervals of the sampling frequency in both horizontal and vertical directions. Since these spectra retain their complex nature, multiplication by a complex exponential corresponding to scene phasing is easily accomplished if desired. The resulting frequency domain pattern is quite complex. It contains the original filtered spectrum plus copies of the original repeated at horizontal and vertical spatial sampling frequencies. This resultant spectrum is then multiplied by the image reconstruction MTF and PTF. Since the image reconstruction filter is centered at coordinates (0,0) and quickly drops to zero (see Fig. 5.5), most of the repeated aliasing spectra are filtered out almost entirely. The original filtered image also has some high frequency content filtered out. The final spectrum resulting has all of the blurring and aliasing effects of the device included. It contains the reconstruction filtered original image, and a vestige of the alias terms. This spectrum is then used to calculate the contrast transference parameter. As an alternative, VISMODII also implements an optional sample scene phase MTF, just as implemented in FLIR92. The feasibility of neglecting both aliasing and scene phasing effects are studied in the next chapter.

3. Contrast Transference Parameter Calculation

In VISMODII, the filtered and aliased target spectrum, and a copy of the filtered un-aliased target spectrum are retained for the output contrast determination. Both of these spectra are inverse transformed back into the spatial domain by the inverse two dimensional FFT. The output image corresponding to the unaliased version, as expected, is a 'smoothed' out version of the input four bar pattern, with a noticeably reduced contrast. The contrast reduction is a function of the input spatial frequency of the bar pattern, as shown in Fig. 5.6 and Fig. 5.7. Comparing the two figures illustrates the dramatic difference in contrast transference as a function of the target spatial frequency. The pattern at the higher spatial frequency has had its contrast reduced to a much greater extent.

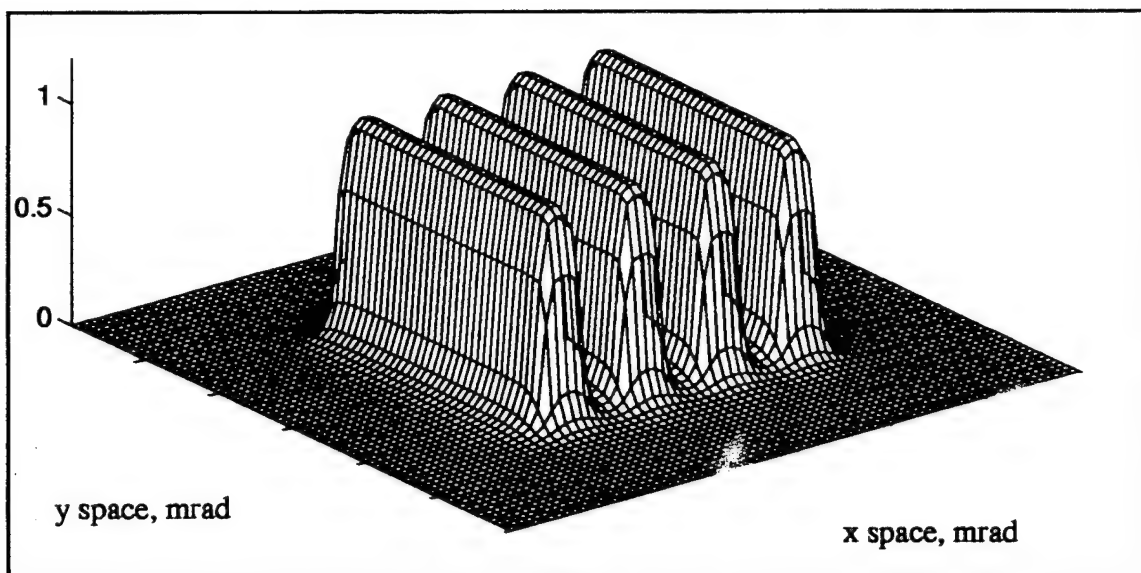


Figure 5.6. Filtered output target image, spatial frequency = 0.1 cy/mrad

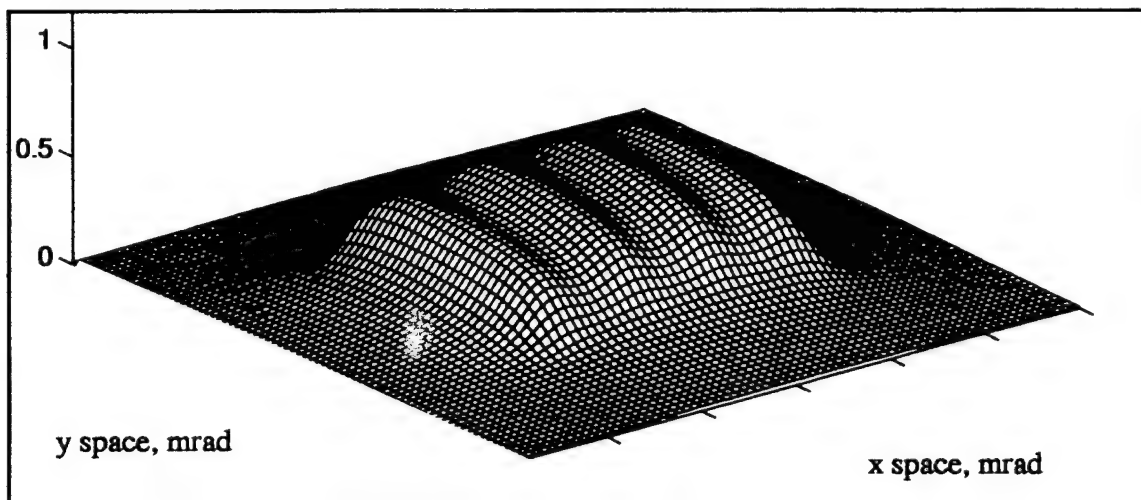


Figure 5.7. Filtered output target image, spatial frequency = 1.1 cy/mrad

To determine the contrast present in the final image, a two dimensional averaging process is applied to the portions of the output image corresponding to the peaks of the bars and the troughs in between them. The average over the peaks is denoted as T_p , and the average over the troughs is denoted T_t . The averaging process for each occurs in two dimensions to account for contrast degradation along the long dimension of the bars as well

as the nominal pattern direction described by the bar width. The difference between the two averages represents the unaliased output contrast. This value is modified by the subtraction of an alias noise value.

The alias noise value is determined by subtracting the unaliased output image from the aliased one. The variance of this zero-mean random noise over the target area is taken to be the 'alias noise', denoted σ_{alias} . This value is subtracted from the unaliased output contrast to give a final, aliased contrast transference parameter. For a given target spatial frequency, the output contrast value is given by:

$$\Delta T_s(f) = T_p(f) - T_t(f) - \sigma_{\text{alias}}(f) \quad (5.13)$$

The nominal input contrast is set to one for all spatial frequencies, so the contrast transference parameter is effectively given by:

$$\alpha(f) = \Delta T_s(f) \quad (5.14)$$

To obtain a contrast transference parameter as a function of spatial frequency, this process is repeated over the range of spatial frequencies of interest. The contrast transference parameter for the Mitsubishi system, for horizontal MRTD, is shown in Fig. 5.8.

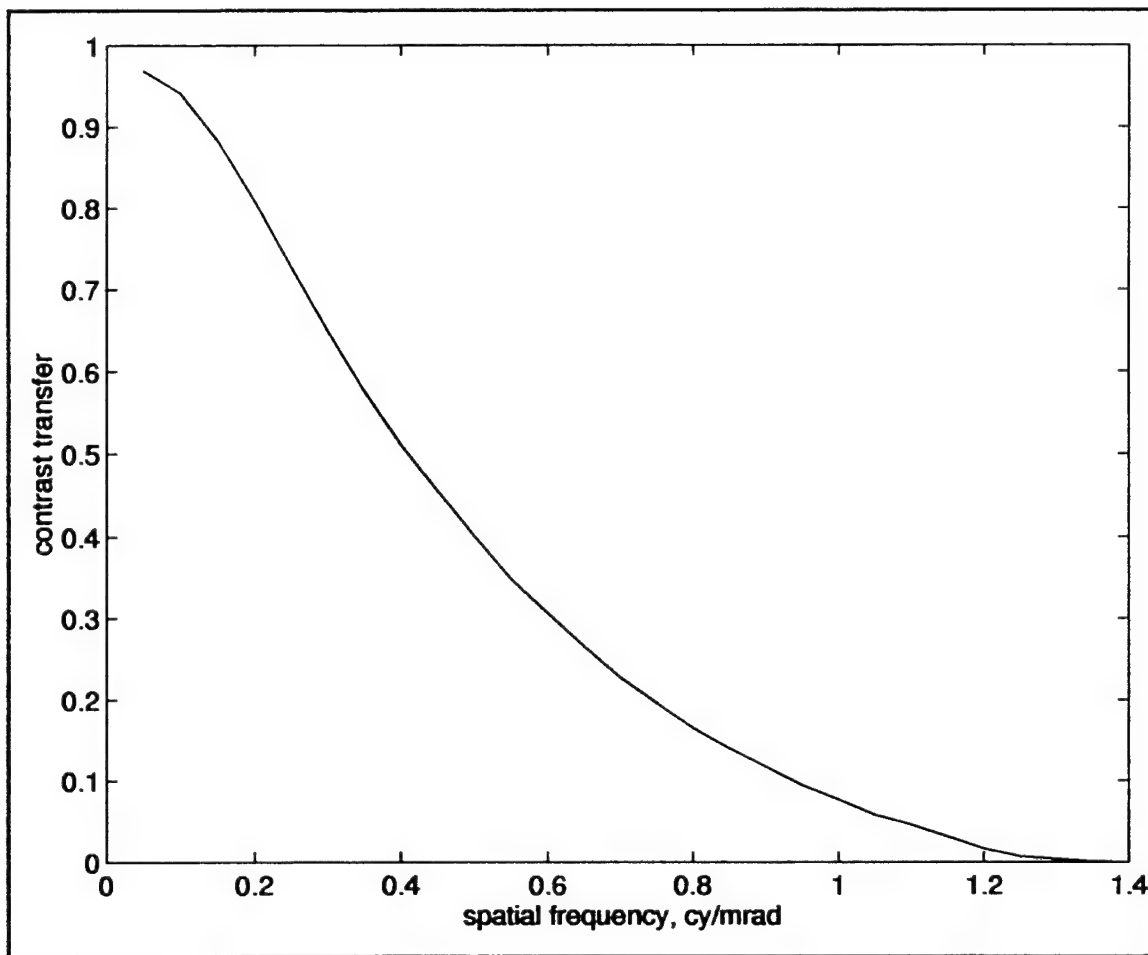


Figure 5.8. Contrast Transference parameter, Mitsubishi system

C. THRESHOLD INPUT CONTRAST

The determination of a critical input contrast threshold for a particular TIS/observer system is difficult. Of course, the best way to determine this value is to measure the TIS/observer system's response to a step function. The TIS/observer system implies that there may be more than one type of observer, and therefore more than one ΔT_{sc} for a single TIS. The advantage of the simplified visibility concept is that no a priori assumptions about the observer are made. For the two TIS used in the laboratory measurements of Chapter IV,

there is a clear low frequency trend toward a non-zero threshold input contrast. The values, as measured in the laboratory, and taken from Fig. 4.5 and Fig. 4.6, are given in Table 5.1.

TABLE 5.1. Subjective threshold input contrast

System	ΔT_{sc} (Celsius)
Amber	0.4
Mitsubishi	0.07

If this parameter cannot be obtained by measurement, the threshold input contrast may be predicted from device parameters. For a subjective human observer based system this requires the incorporation of directional noise effects, ad hoc perception factors, and eye/brain process modeling. For the objective ATR observed system the value could, presumably, be derived from objective data. Each type of threshold input contrast value is discussed in greater detail in the following sub-sections.

1. Analysis for Subjective Minimum Threshold Contrast

To be of value as a predictive model, it is desirable that a human observer based, subjective ΔT_{sc} be predictable from device parameters. A heuristic analysis for calculation of the minimum threshold contrast is presented here. Although this requires the inclusion of perception factors, integration factors, etc.; most of these factors are postulated as having no significant effect in the low spatial frequency limit. In the low frequency limit the treatment of the bar pattern as a periodic function is questionable. Instead, it can be treated as a step function [Ref. 9]. In the first generation visibility model, the formulation of ΔT_{sc} was given by Eq. 2.21. This formulation effectively replaces the reference bandwidth with an actual noise bandwidth for the system, and incorporates a temporal integration factor for the eye [Ref. 9]. For the sample system of Appendix A this yielded a value of 0.208 Celsius for a system with an NETD of 0.36 Celsius [Ref. 9].

In FLIR92, the incorporation of directional noise concepts resulted in the re-formulation of the noise term in the MRTD analysis. The temporal pixel noise, σ_{tvh} , was based on the NETD as given by Eq. 3.7. In FLIR92, the NETD was modified by a system noise bandwidth, similar to the actual noise bandwidth term given in the first generation visibility model. The FLIR92 formulation for MRTD also included temporal and spatial eye integration effects and directional noise correction factors.

Consistent with the concepts presented in each of the above models, the heuristic formulation for a subjective ΔT_{sc} includes three-dimensional noise correction, temporal integration, and a bandwidth correction term. Comparing the first generation visibility model formulation for ΔT_{sc} with the FLIR92 formulation for MRTD suggests the second generation ΔT_{sc} could be found by replacing the NETD in the first generation formulation with the σ_{tvh} term and the appropriate directional noise components. The heuristic formulation is:

$$\Delta T_{sc} = \frac{\pi^2}{8} \text{SNR}_{thr}(\sigma_{tvh}) \left(1 + \frac{\sigma_{vh}^2}{\sigma_{tvh}^2} \right)^{0.5} (E_t)^{0.5} \quad , \quad (5.15)$$

where the σ_{tvh} term is formulated as in Eq. 3.7. In this formulation, the E_t term represents the SNR enhancement brought about by the temporal integration of the eye over the displayed signal, since the signal is correlated from frame to frame but the noise is not. It is given by:

$$E_t = \frac{1}{t_e F_{dot}} \quad . \quad (5.16)$$

The threshold SNR can be set to give the desired probability of resolution [Ref. 7]. The σ_{tvh} term is the random pixel noise associated with the device as measured, or as predicted by Eq. 3.7 [Ref. 16]. For most staring systems the only directional noise factor of consequence is the spatial noise, σ_{vh} [Ref. 16, ARG-10]. The remaining directional noise effects are not included in the analysis. The default value for the spatial noise is postulated

to be $0.40 \sigma_{tvh}$ as given in Appendix C. Perception factors for the horizontal and vertical directions are postulated to be not applicable in the low frequency limit [Ref. 9]. If the values of σ_{tvh} and σ_{vh} are available from measurement data, Eq. 5.15 can be evaluated directly. If this data is not available, σ_{tvh} can be estimated using Eq. 3.9, and the default value can be used for σ_{vh} .

Using this formulation, the minimum threshold contrast for the Mitsubishi system is calculated to be 0.0381 Celsius. For the Amber system, the heuristic calculation yields 0.00857 Celsius. Comparing these values to the ones given in Table 5.1 reveals that the lab measured values do not agree with this formulation. The heuristic formulation of Eq. 5.15 gives threshold values well below those measured. It is postulated that the error is introduced in the bandwidth correction factor, because this is not easy to define for second generation staring systems. The noise characteristics of the two dimensional staring array with its associated sampling, clock-out, and aliasing problems are apparently more complicated than is given in the simple heuristic formulation. A more complete prediction for the minimum threshold contrast value is a potential subject for further analysis.

2. Analysis for Objective Minimum Threshold Contrast

The objective formulation for ΔT_{sc} is required for systems without a human observer in the loop. A device such as an ATR will have its own value of threshold input contrast, even when the same TIS is used. As the data presented in Figs. 4.11, 4.12, and 4.13 suggest, the ATR system experiences a degradation in contrast, as measured by the SNR, with increased spatial frequency in a manner similar to that experienced by a human observer. This suggests that the model can be applied equally well to an ATR system, if the appropriate minimum threshold contrast value could be found.

The most reliable means to determine the minimum threshold input contrast value for an ATR device is, of course, to measure it. As Fig. 4.11 demonstrates, this value can be much higher than the threshold input contrast resolvable by a human observer for the same nominal output signal to noise ratio. As observed in the laboratory measurements, in

order to achieve an SNR of 6.0 as measured on the oscilloscope, the temperature difference had to be greatly increased above that required for a human to detect the pattern in the display. The SNR value of 6.0 was chosen arbitrarily because it is nominally the SNR required for 100% probability of detection for a human observer [Ref. 28]. As indicated by Fig. 4.10, the ATR used in the simulation probably could have resolved the target well before this SNR was achieved. It is possible, however, that a given device may require an input SNR as high as this to meet its recognition performance parameters (e.g., low false alarm rate.) The fact that the human observer can resolve a target when the oscilloscope measured output SNR is much less than 6.0 implies either that the actual human resolvable SNR is a great deal less than 6.0, or the oscilloscope itself significantly degrades the output signal. For example, at a spatial frequency of 0.5 cy/mrad, the human observer could resolve the four bars with 100% probability of resolution at an MRTD of about 0.25 Celsius (Fig. 4.6). To achieve an SNR (nominal) corresponding to the same detection probability, the ATR device required an MRTD of about 3.75 Celsius (Fig. 4.13). However, regardless of the actual threshold values of output SNR required for the human and ATR to resolve the target, the fact that these threshold values may be different is an essential element of VISMODII. Once a resolution threshold for an ATR device has been established, performance prediction can be easily obtained using the visibility model concepts.

Figure 4.11 implies an objective ΔT_{sc} in the low frequency limit for the simple ATR simulation conducted to be about 4 to 5 degrees Celsius, about 65 times larger than the subjective ΔT_{sc} of around 0.07 Celsius. This demonstrates the difficulty in developing an ATR system that can rival a human observer for resolution tasks. Figure 4.13 demonstrates an almost linear falling off in SNR measured as ΔT is decreased. This suggests an additional MTF parameter may be required for the electronics of the ATR device itself. Figure 4.12 confirms that in the low frequency limit the SNR approaches a threshold value for a given temperature. If the threshold SNR for the device could be determined by measurement, perhaps of some electronic test signal, then perhaps this data could be used

in the heuristic formulation of an objective ΔT_{sc} . Once this formulation is completed for an individual ATR device, perhaps the results could be extended to entire classes of systems.

The process of finding the appropriate threshold input contrast value for an ATR device is an interesting question, and deserves further analysis. Since the framework of the VISMODII is already in place, this could open the door to an objective measure of resolution.

D. RESULTS

Based on laboratory measured subjective ΔT_{sc} for the TIS systems used (Table 5.1), and the contrast transference parameters calculated by VISMODII, the following MRTD plots were obtained. Horizontal and vertical MRTD curves were generated by the model, then the values were geometrically averaged to produce a two dimensional MRTD. These plots are compared to FLIR92 predictions and measured laboratory results in the next chapter.

Figure 5.9 shows the VISMODII predicted MRTD curve for the Amber system. Figure 5.10 shows the VISMODII prediction for the Mitsubishi system. The vertical MRTD for these two systems was calculated by rotating the target pattern by 90 degrees. In each case, the measured value of ΔT_{sc} was used. The Amber MRTD prediction is very similar in both vertical and horizontal directions because of the symmetry in the detector elements and the detector array. The slight difference that does exist may arise from the assumed clock-out pattern for the device. In the Mitsubishi system, the difference between the vertical and horizontal predictions is larger. For both systems, VISMODII predicts a severe cut-off at approximately 1 cy/mrad. Near this point, the resolution limit of both systems is reached. As is shown in the next chapter, this corresponds well with observed results.

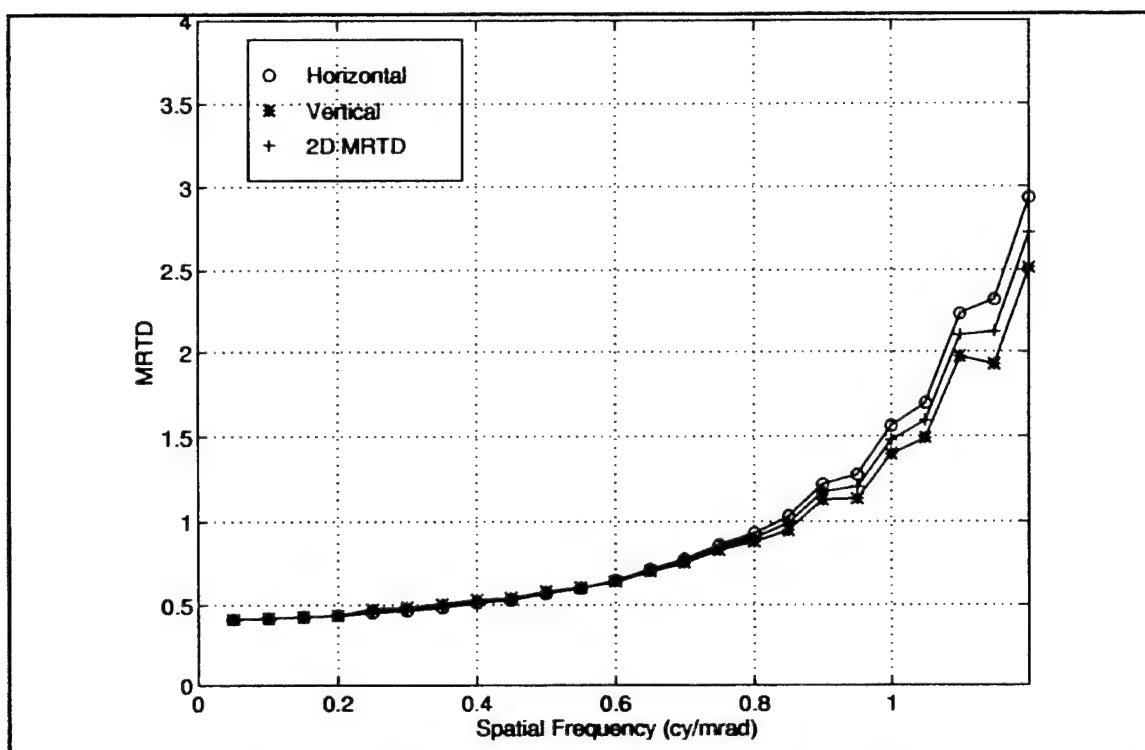


Figure 5.9. VISM0DII predictions for Amber system MRTD

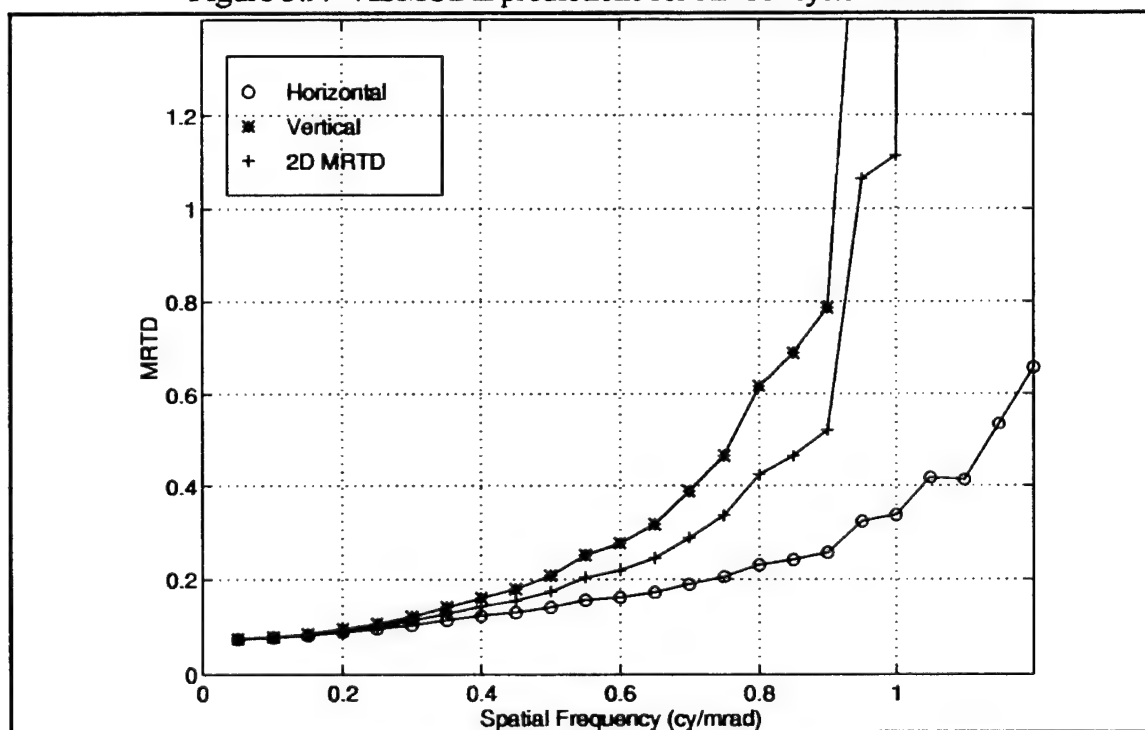


Figure 5.10. VISM0DII predictions for Mitsubishi system MRTD

VI. DATA ANALYSIS AND CONCLUSIONS

This chapter is a comparative analysis of the VISMODII model. The model is compared to the actual laboratory measurement data recorded in Chapter IV and Appendix D; and the predictions of the FLIR92 model presented in Appendix C. This comparative analysis demonstrates the validity of the visibility model concepts applied to second generation systems. Since the two systems used in the laboratory are quite different in their capabilities and parameters, the comparison also demonstrates the suitability of VISMODII for a wide range of FPA imagers.

After VISMODII predictions are validated against FLIR92 and measured data, an exploration of the effects of various second generation modeling considerations is accomplished. In this second section, VISMODII is modified to study the result of including or neglecting various of the effects presented in Chapter III. The model's predictions with and without aliasing, for example, are compared to measured data. These comparisons demonstrate the degree of significance these effects have on the predicted and measured performance of the device. The chapter closes with some conclusions, and suggested directions for further research.

A. COMPARISON OF PREDICTIVE RESULTS TO MEASUREMENT

The following predictive plots were generated for horizontal, vertical, and two dimensional MRTD by VISMODII and by FLIR92 from the data contained in Appendix A. The VISMODII predictions also use the laboratory measured subjective ΔT_{sc} for the TIS systems used (Table 5.1). The lab data two dimensional MRTD figure is calculated by geometrically averaging the measured horizontal and vertical results, in the same manner that the other two dimensional MRTD performance curves were obtained. All three plots appear together for comparison purposes for each of the systems used.

Figure 6.1 compares the VISMODII predicted MRTD curve for the Amber system with the measured results and the FLIR92 predicted curve. Figure 6.2 shows the

VISMODII prediction for the Mitsubishi system, compared to measured results and FLIR92 predictions for that system.

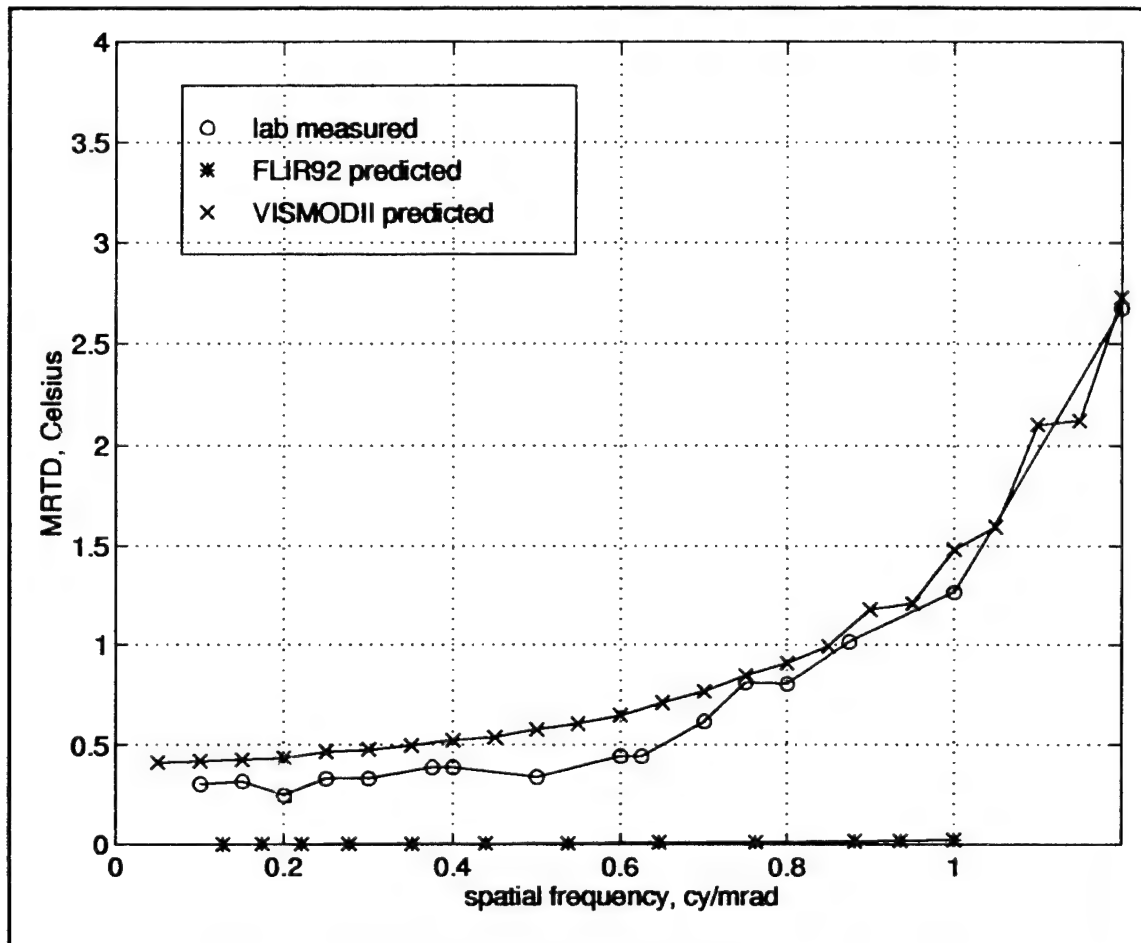


Figure 6.1. Amber system two dimensional MRTD predictions

In Fig. 6.1, it is shown that the predictive models give quite different performance predictions for this device. The FLIR92 model appears quite optimistic compared to measured results. The primary cause of this mismatch is conjectured to be the D^* parameter for other than PtSi detectors. Since FLIR92 is designed primarily for PtSi detector arrays, it may be somewhat less reliable for predictions for devices that use other materials. The Amber system is an InSb array, with a D^* an order of magnitude higher than most PtSi arrays.

As explained in Appendix C, the FLIR92 predictions also stop at the calculated system Nyquist frequency (about 1 cy/mrad). The actual laboratory measurements suggest, however, that resolution is still possible beyond this frequency. VISMODII extends prediction beyond this point by incorporating aliasing effects in the model. Figure 6.1 does indicate that the VISMODII model provides MRTD predictions that are at least as good as FLIR92 for the Amber system.

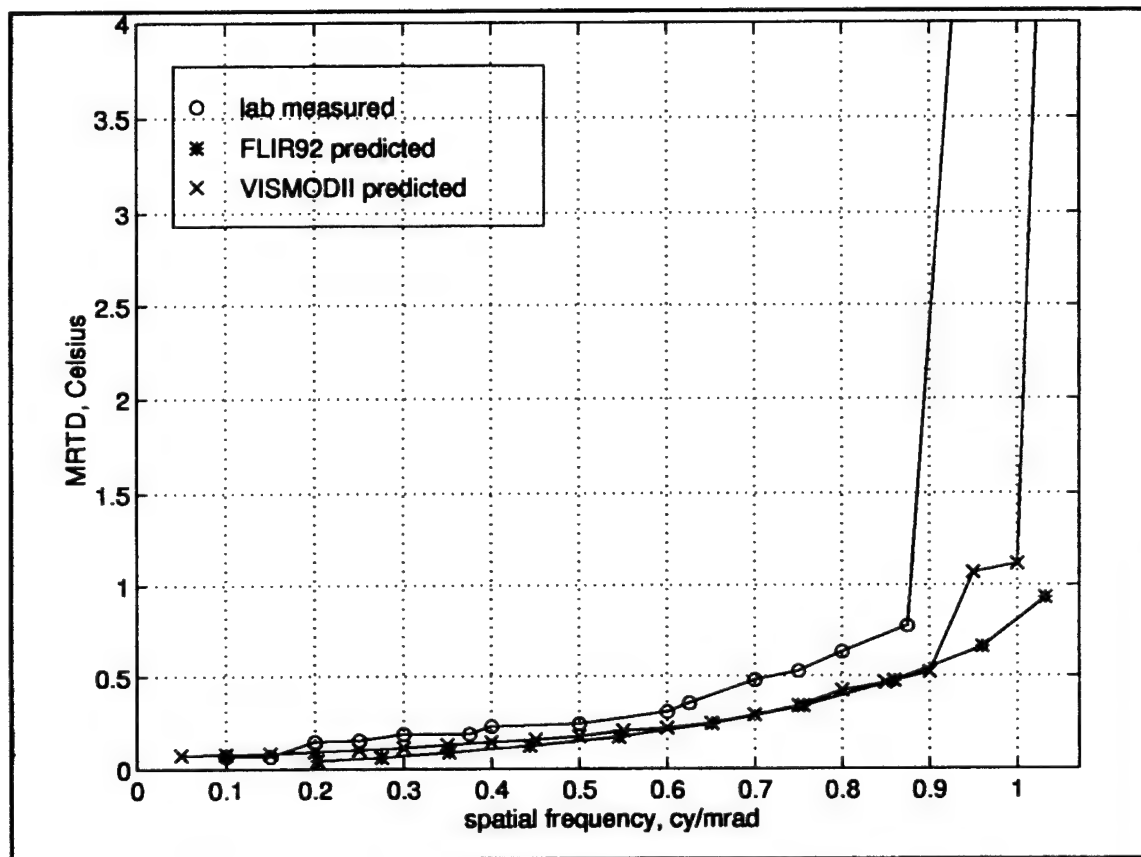


Figure 6.2. Mitsubishi system two dimensional MRTD predictions

As shown in Fig. 6.2, the predictions of the two models are much closer for the PtSi array used in the Mitsubishi system. This gives credence to the idea that FLIR92 is more reliable for predicting performance for PtSi arrays than for other types. Both models give quite reasonable predictions for low spatial frequencies. The FLIR92 predictions, however, do appear to go to zero in the low frequency limit. The measured data and the

VISMODII predictions do not. The figure shows that there is a sharp increase in measured MRTD at around 0.9 cy/mrad. This cutoff is predicted by VISMODII which includes aliasing effects that become significant near this spatial frequency. As observed in Chapter IV, this region also marks the limits of the resolution of the system. Beyond this point, a single bar in the bar pattern spans less than one pixel on the display. The four bars blend together, making resolution of each an impossibility. It is suggested by the data that the pixel resolution limit of the system is not perfectly predicted by either model. It is clear from both Fig. 6.1 and Fig. 6.2 that the visibility model concepts can be used with some success in predicting the performance of second generation systems.

B. EXPLORATION OF THE MODEL

This section is a brief exploration of the visibility model and the impact of the second generation modeling considerations presented in Chapter III. Although the modeling concepts have certain mathematical interest and validity, it is also valuable to see if their effects are significant in the actual prediction of device performance.

Figures 6.3 and 6.4 present the VISMODII predictions for the two systems for both vertical and horizontal measurement. The VISMODII predictions appear to be quite accurate, closely paralleling measured results. Because of the assumed vertical clock-out scheme of the Amber system, the predictive performance in the vertical and horizontal directions are slightly different. Since the detectors in this system are square, this is the only effect that is expected to differ between the two orientations. The measured data suggests that there is a slight difference in the performance of the Amber system in the two directions. This difference is predicted by VISMODII.

For the Mitsubishi system, the model gives predictive results that very closely match the performance of the device. In this case there is a clear distinction between the two orientations as the detectors are rectangular, not square. This fact, plus the clock-out effect cause the vertical MRTD performance for this system to be much poorer than the horizontal. VISMODII predicts this rapid decline in resolvability in the vertical direction.

The effect is predominantly due to the assumed vertical clock-out pattern and the difference in sampling frequencies caused by the rectangular shape of the detector cells in the focal plane array. Figure 6.4 suggests that both the clock-out process and the aliasing effects are properly modeled for this device. It also demonstrates again the validity of the visibility model concepts.

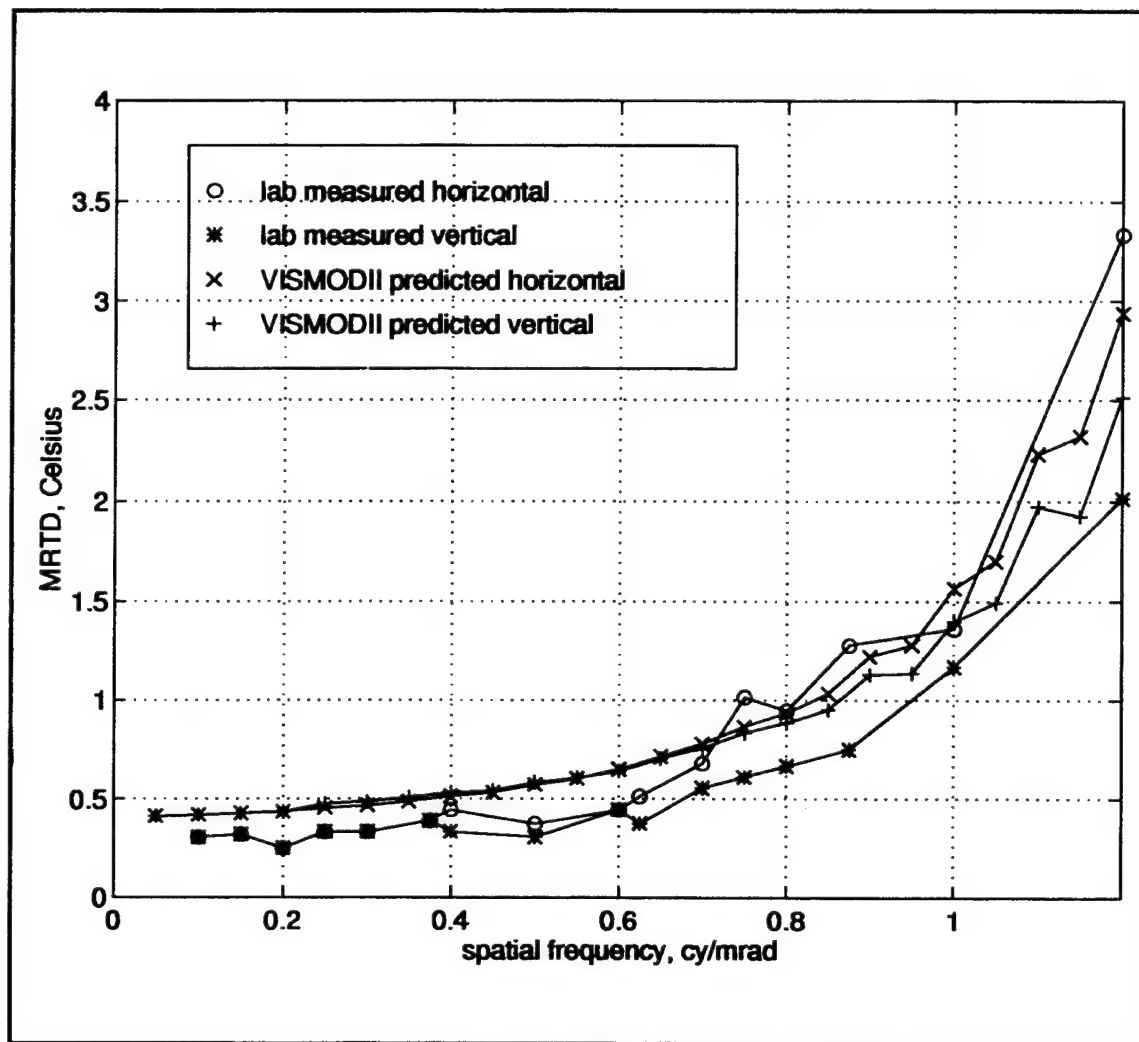


Figure 6.3. Amber system horizontal/vertical predictions

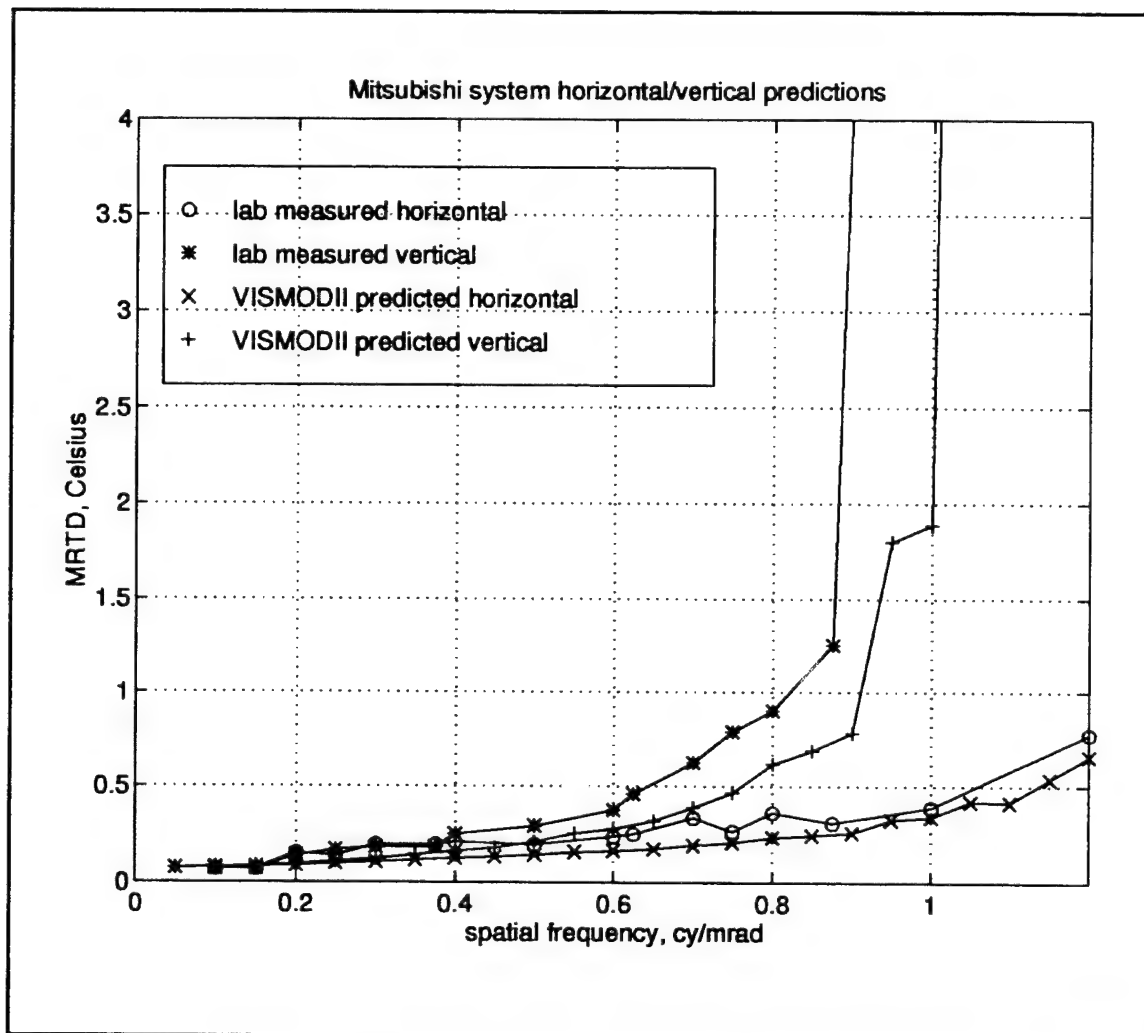


Figure 6.4. Mitsubishi system horizontal/vertical predictions

The next two plots demonstrate the effects of aliasing and sample-scene phasing effects on the predictive model. In Fig. 6.5, different methods of including sample-scene phase effects are presented and compared. In Fig. 6.6, the effect of ignoring aliasing effects on both horizontal and vertical MRTD performance is demonstrated.

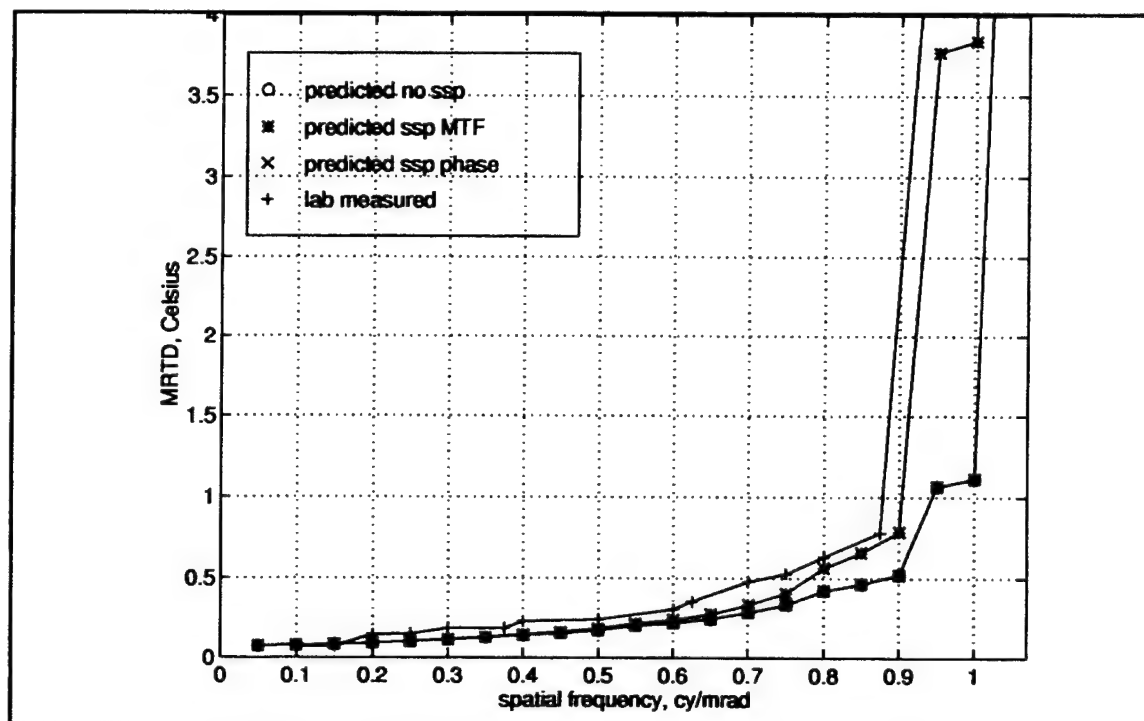


Figure 6.5. Mitsubishi system sample-scene phase effects

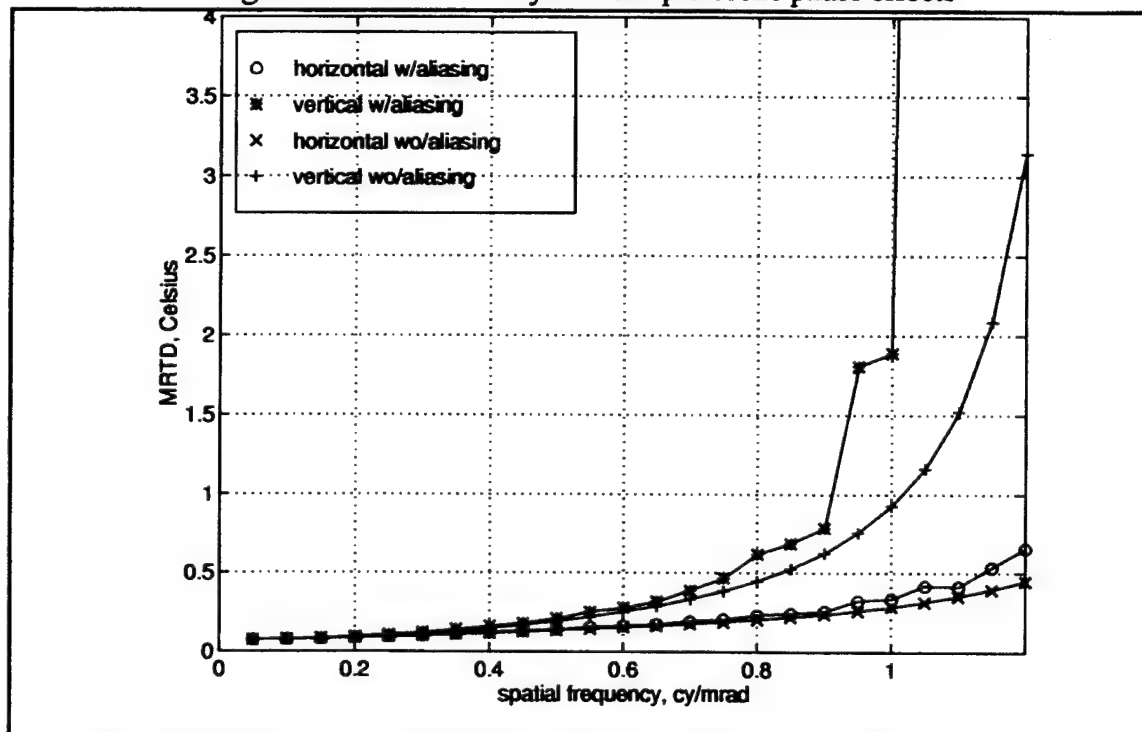


Figure 6.6. Mitsubishi system aliasing impact on predicted MRTD

Figure 6.5 demonstrates the effect of sample-scene phasing (ssp) on the predictive model. Four curves are shown. The predicted two dimensional MRTD curve with no sample-scene phase effects coincides exactly with the curve predicted when the sample-scene phase effect is included as multiplication by a complex exponential as given by Eq. 3.31. This indicates that multiplication by an exponential does not have a measurable effect on performance prediction and could, in practice, be reasonably ignored.

A second means of modeling sample-scene phase effects is to include an additional MTF in the image formation filter [Ref. 16]. This is the method used in FLIR92, as discussed in Appendix C. This MTF, when included, brings the predicted MRTD curve much closer to measured results. This is probably because the original prediction curve is too optimistic. This method of modeling may impose too severe constraints on predicted system performance as it has a large effect on the predictive outcome of the model. This large effect intuitively seems out of proportion to the actual effects of sample scene phasing. In all cases, the models converge at low frequencies. In the low frequency case, the objects to be resolved are larger and cover more detector elements in the array. This makes the relative position between the image on the detector plane and the centers of the detector elements themselves less important.

Figure 6.6 demonstrates the impact of failing to include aliasing effects in the predictive model. As shown, the prediction curves without aliasing are quite a bit more optimistic than the predictions that include aliasing effects. Aliasing effects are also shown to be present even below the system Nyquist frequency. The effects of aliasing are clearly present at spatial frequencies as low as 0.6 cy/mrad. This suggests that the FLIR92 method of stopping predictions at the Nyquist frequency is inadequate. For accurate predictive results, aliasing effects must be included at even low frequencies.

The effects of aliasing are also shown to affect the shape of the curves. Whereas the unaliased curves are smooth, corresponding to the general Gaussian roll-off of the image formation and reconstruction filters, the aliased ones include some high frequency 'ripple'. This is consistent with the modeling of aliasing as demonstrated in Chapter III.

The spurious aliasing term consists of relatively higher frequency components, creating the 'ripple' effect. This may help explain some of the ripple effect that appears in the laboratory measured curves as well.

C. CONCLUSIONS

The laboratory validation of the VISMODII predictive results is an important milestone. The results obtained, although limited in scope, do indicate that an MRTD predictive model based on a minimum threshold contrast and a contrast transference parameter can provide reasonably accurate results. The visibility model, then, is confirmed as a simple yet accurate means of predicting FLIR performance. It is predicted from these limited results that a more robust analysis would confirm the viability of the visibility model concepts.

The power of the model developed, however, is that it can achieve prediction accuracy on a par with other second generation models without making complicated eye/brain recognition process assumptions. VISMODII, although computationally and conceptually simple, is also more complete than some other models in its treatment of the entire aliasing/scene phasing process. As seen in this chapter, these effects cannot be ignored even at low frequencies. The implementation of three dimensional noise and clock-out frequency effects is also a valuable addition to a predictive model.

The move toward objective ATR type systems is well underway, and is not likely to change course. Because the visibility modeling process makes no assumptions about the eye/brain recognition process, it could easily be used to predict performance for ATR devices as well as human observer systems. This may be the most significant result of the visibility model. This model clearly demonstrates the feasibility of an objective MRTD concept based on a contrast transference, and serves as a possible basis for further exploration of the whole ATR objective MRTD modeling process. An accepted definition of the 'objective' MRTD, however, still needs to be found. A more desirable course of action may be the development of a replacement figure of merit.

It is clear from the results obtained that MRTD performance prediction models for second generation systems that are extrapolations of first generation concepts that ignore many second generation effects will probably prove to be inadequate. VISMODII is hopefully a bridge that, on one hand, is backwards compatible with the community standard figure of merit, the subjective MRTD; and, on the other hand, is a step in the development of a new and more objective resolvability criterion. It is hoped that it will be useful in further development in this direction.

D. DIRECTIONS FOR FURTHER RESEARCH

The wide scope of the thermal imaging process makes it a fascinating topic. Elements of physics, optics, electronics, mathematics, and visual psycho-physics are all present. Additionally, computer imaging, digital signal processing and electrical engineering are all present in various degrees. In following one path through this interdisciplinary subject matter, it is not possible to cover all topics of interest. The possibilities for further research are almost endless. A few specific items of interest are provided as possible directions for future research.

VISMODII could be enhanced by the addition of several features. The model currently only calculates exactly horizontal and exactly vertical MRTD's. A predictive model in the future should be able to predict performance for all angles. Along with the increased flexibility, VISMODII could benefit from more efficient computer coding and a better user interface. It could include a more complete MTF analysis, and a more complete heuristic formulation of the critical threshold contrast.

The process of finding the appropriate objective threshold input contrast value for an ATR device is an interesting question, and deserves further analysis. Since the framework of the VISMODII is already in place, this could open the door to a new objective measure of resolution. A more complete analysis of the subjective MRTD's application to ATR devices would be helpful in this regard.

More laboratory validation is required. Laboratory measurements for more complex ATR devices could be obtained and compared to subjective results. This would help determine the framework for an objective resolution criterion and figure of merit.

Finally, VISMODII still refers to a four-bar target pattern (as do other state-of-the-art models). To address the application of systems to real field situations and the detection of real targets, i.e., ships, tanks, and people, it would be valuable to explore the possibility of replacing the standard four-bar test with one requiring the discernment of spatial detail or patterns from a complex or cluttered background scene.

LIST OF REFERENCES

1. J.A. Ratches, W.R. Lawson, L.P. Obert, R.J. Bergemann, T.W. Cassidy, J.M. Swenson, "Night Vision Laboratory Static Performance Model For Thermal Viewing Systems," U.S. Army Electronics Command Report # 7043, Night Vision Laboratory, Fort Belvoir, Virginia, 1975.
2. F.A. Rosell, G. Harvey, eds., "The Fundamentals of Thermal Imaging Systems," Navy Research Laboratory Report No. 8311, Naval Research Laboratory, Washington, D.C., 1979.
3. J.M. Lloyd, *Thermal Imaging Systems*, Plenum Press, New York, 1975.
4. W. Wittenstein, J.C. Fantenella, A.R. Newberry, J. Baars, "The Definition of the OTF and the measurement of aliasing for sampled imaging systems," *Optica Acta*, Vol. 29, No. 1, pp. 41-50, 1982.
5. G.C. Holst, *Electro Optical Imaging System Performance*, SPIE Optical Engineering Press and JCD Publishing, Winter Park, FL, 1995.
6. Papoulis, A., *Probability, Random Variables, and Stochastic Processes*, 3rd ed., McGraw-Hill, Inc., New York, 1991.
7. D.L. Shumaker, J.T. Wood, C.R. Thacker, *Infrared Imaging Systems Analysis*, Environmental Research Institute of Michigan, Ann Arbor, MI, 1993.
8. C.M. Webb, "MRTD, How Far Can We Stretch It?," *SPIE Proceedings on Infrared Imaging Systems: Design, Analysis, Modeling, and Testing*, Vol. 2224, pp. 297-307, April, 1994.
9. R.J. Pieper, A.W. Cooper, "A visibility model for MRTD prediction," *SPIE Proceedings on Infrared Imaging Systems: Design, Analysis, Modeling, and Testing*, Vol. 2224, pp. 258-269, April, 1994.
10. A.R. Ugarte, "Modeling For Improved Minimum Resolvable Temperature Difference Measurements," Master's Thesis, Naval Postgraduate School, Monterey, CA, September, 1991.
11. M.J. Jenquin, "A Bridge Between Modulation Transfer Function and Minimum Resolvable Contrast," *SPIE Proceedings on Infrared Imaging Systems: Design, Analysis, Modeling, and Testing*, Vol. 2470, pp. 380-385, April, 1995.

12. H.V. Kennedy, "Modeling Noise in Thermal Imaging Systems," SPIE Vol. 1969, pp. 66-77, August, 1993.
13. J.A. D'Agostino, "A 3-D Noise Analysis Methodology," *IRIS Passive Sensors Symposium*, March, 1991.
14. C.M. Webb, P.A. Bell, G.D. Mayott, "Laboratory Procedure for the Characterization of 3-D Noise in Thermal Imaging Systems," *IRIS Passive Sensors Symposium*, March, 1991.
15. L. Scott, J.A. D'Agostino, "NVEOD FLIR92 Thermal Imaging Systems Performance Model," SPIE Vol. 1689, September, 1992.
16. U.S. Army Night Vision and Electronic Sensors Directorate, *FLIR92 Thermal Imaging Systems Performance Model Analyst Reference Guide*, Document RG5008993, Ft. Belvoir, VA, January, 1993.
17. F.O. Huck, N.Halyo, S.K. Park, "Aliasing and blurring in 2-D sampled imagery," *Applied Optics*, Vol. 19, No. 13, July, 1980.
18. S.K. Park, R. Hazra, "Aliasing As Noise, A Quantitative and Qualitative Assessment," SPIE Vol. 1969, pp. 54-65, August, 1993.
19. L.M. Biberman, *Perception of Displayed Information*, Plenum Press, New York, 1973.
20. T. Meitzler, G. Gerhart, "Spatial aliasing effects in ground vehicle IR imagery," SPIE Vol. 1689, pp. 226-240, September, 1992.
21. A.H. Lettington, Q.H. Hong, "An Anti-aliasing Algorithm for Focal Plane Arrays," SPIE Vol. 2470, pp. 134-140, April, 1995.
22. E.A. Watson, R.A. Muse, F.P. Blommel, "Aliasing and blurring in microscanned imagery," SPIE Vol. 1689, pp. 242-250, September, 1992.
23. S.K. Park, R.A. Schowengerdt, "Image sampling, reconstruction, and the effect of sample-scene phasing," *Applied Optics*, Vol. 21, No. 17, pp. 3142-3151, September, 1982.
24. S.K. Park, R.A. Schowengerdt, M.A. Kaczynski, "Modulation transfer function analysis for sampled image systems," *Applied Optics*, Vol. 23, No. 15, pp. 2572-2582, August, 1984.

25. M.A. Chambliss, J.A. Dawson, E.J. Borg, "Measuring the MTF of undersampled staring IRFPA sensors using 2D discrete Fourier transform," *SPIE Vol. 2470*, pp. 312-324, April, 1995.
26. H.V. Kennedy, "Modeling second-generation thermal imaging systems," *Optical Engineering*, Vol. 30 No. 11, pp. 1771-1778, November, 1991.
27. U.S. Army Night Vision and Electronic Sensors Directorate, *FLIR92 Thermal Imaging Systems Performance Model User's Guide*, Document UG5008993, Ft. Belvoir, VA, January, 1993.
28. J. M. Mooney, "Effect of spatial noise on the minimum resolvable temperature of a staring sensor," *Applied Optics*, Vol. 30 No. 23, pp. 3324-3332, August, 1991.
29. C.M. Webb, "An Approach to 3-Dimensional Noise Spectral Analysis," *SPIE Vol. 2470*, pp. 288-299, April, 1995.
30. D.A. Scribner, M.R. Kruer, C.J. Gridley, "Measurement, characterization, and modeling of noise in staring focal plane arrays," *SPIE Proceedings on Infrared Sensors and Sensor Fusion*, Vol. 782, pp. 147-160, 1987.
31. H. Orlando, T. Luu, "Modulation transfer function (MTF) analysis for a FLIR system with nonlinear video electronics," *Proceedings of the IEEE 1993 National Aerospace and Electronics Conference*, Vol. 2, pp. 1056-1059, August, 1993.
32. L. Obert, J.D'Agostino, "An experimental study of the effect of vertical resolution on FLIR performance," *Proceedings of the IRIS Passive Sensors Symposium*, Vol. I, pp. 235-251, January, 1990.
33. L.O. Vroombout, "Second generation thermal imaging systems design trades modeling," *SPIE Proceedings on Infrared Imaging Systems: Design, Analysis, Modeling, and Testing*, Vol. 1309, pp. 17-26, April, 1990.
34. A.D. Schnitzler, "Theory of spatial-frequency filtering by the human visual system," *Journal of the Optical Society of America*, Vol. 66, No. 6, pp. 608-625, June, 1976.
35. F.W. Campbell, "The Human Eye as an Optical Filter," *Proceedings of the IEEE*, Vol. 56, No. 6, pp. 1009-1014, June, 1968.
36. G.H. Kornfeld, W.R. Lawson, "Visual-Perception Models," *Journal of the Optical Society of America*, Vol. 61, No. 6, pp. 811-820, June, 1971.

37. I. Overington, "Towards a complete model of photopic visual threshold performance," *Optical Engineering*, Vol. 21, No. 1, pp. 002-013, January/February, 1982.
38. Amber Engineering, Inc., *AE4128 Infrared Imaging System User's Manual*, Release 1.0, Goleta, CA, March, 1992.
39. E.G.D. Youngs, R.K. McEwen, "A performance prediction and simulation model for 2 dimensional array imagers," *Proceedings of the IEE Fourth International Conference on Advanced Infrared Detectors and Systems*, No. 321, London, UK, 1990.
40. Mitsubishi Electronics Corporation, *IR-M500 Thermal Imager User's Guide*, Cypress, CA, January, 1994.
41. Personal communication (FAX), Mitsubishi Electronics Corporation, Cypress, CA, September, 1995.

APPENDIX A. THERMAL IMAGING SYSTEM PARAMETERS

This appendix contains the physical system parameters used in producing MRTD prediction plots and taking laboratory measurements. The sample first generation system was chosen to coincide with the sample first generation system detailed in Lloyd [Ref. 3]. The Amber and Mitsubishi systems are second generation staring focal plane array devices, representative of many of the commercially available systems to be found. These two systems were also used to make laboratory measurements. For the two second generation systems, the data is presented in the same format as required by the FLIR92 program. The data listed for the Amber system was obtained from the User's Manual [Ref. 38]. The data for the Mitsubishi system was obtained from the user's manual [Ref. 40], and from Mitsubishi Electronics America, Cypress, CA [Ref. 41].

A. SAMPLE FIRST GENERATION SYSTEM

Focal length.	50 mm
Diameter of lens	20 mm
F/number.	2.5
Detector element size	5 mm x 5 mm
Horizontal angular subtense	1 mrad
Vertical angular subtense	1 mrad
Spectral Bandpass	8 μm - 11 μm
D*	$2.0 \times 10^{10} \text{ cm Hz}^{0.5}/\text{W}$
Frame rate	30 Hz
Scan rate format	60 fields/sec
Number of scan columns	150
Number of scan lines	300
Interlace.	2 to 1
Scan efficiency	0.64
Detector vertical spacing.	1 mrad

Horizontal Field of View	400 mrad
Vertical Field of View	300 mrad
Detector dwell time	2.67×10^{-5} sec
Horizontal scanning velocity	37453.2 mrad/sec
3-dB Electronic roll-off frequency	18716.6 Hz
CRT spot size	0.25 mrad
Reference bandwidth for NETD	29.4 kHz
Background temperature	300 K
Target wavelength (monochromatic)	10 μ m
Optical efficiency of the viewer	0.8
Threshold SNR	4.5
Eye integration time	0.2 sec

B. AMBER ENGINEERING MODEL AE4128

Laboratory temperature	300 K
Background temperature	294 K
BLIP performance	YES
Spectral cut-on	3.0 μ m
Spectral cut-off	5.0 μ m
F/ number	3.0
Focal length	10.0 cm
Optical transmittance	0.95
Frame rate	109 Hz
Detector active horizontal dimension	40 μ m
Detector active vertical dimension	40 μ m
D*	5.9×10^{11} cm Hz ^{0.5} /W
Integration time	8887.615 μ sec

Number of columns in detector array	128
Number of rows in detector array	128
Detector cell horizontal dimension	50 μm
Detector cell vertical dimension	50 μm
Number of active CRT lines	480
Display brightness	10.0 mLamberts
Display height	17.78 cm
Display viewing distance	88.9 cm
Threshold SNR	6.0
Eye integration time02 sec
3D noise level (used in FLIR92, see Appendix C)	MOD

C. MITSUBISHI M500 THERMAL IMAGER

Laboratory temperature	300 K
Background temperature	294 K
BLIP performance	YES
Spectral cut-on	3.0 μm
Spectral cut-off	5.0 μm
F/ number	1.4
Focal length	5.0 cm
Optical transmittance	0.95
Frame rate	60 Hz
Detector active horizontal dimension	16.24 μm
Detector active vertical dimension	12.49 μm
D*	$5.0 \times 10^{10} \text{ cm Hz}^{0.5}/\text{W}$
Integration time	16145.833 μsec
Number of columns in detector array	512

Number of rows in detector array	512
Detector cell horizontal dimension	26 μm
Detector cell vertical dimension	20 μm
PtSi emission coefficient.	0.16 1/eV
Schottky barrier height22 eV
Number of active CRT lines	480
Display brightness.	10.0 mLamberts
Display height.	27.94 cm
Display viewing distance	88.9 cm
Threshold SNR	6.0
Eye integration time	0.2 sec
3D noise level (used in FLIR92, see Appendix C)	MOD

APPENDIX B. RATCHES/LLOYD CONVERSION FACTOR

The Ratches and Lloyd first generation MRTD prediction models can be shown to be equivalent with the addition of a frequency dependent conversion factor. This conversion factor was first postulated in Ref. 9. A more complete derivation of this factor is contained in this appendix.

The two formulations for MRTD given by the Ratches and Lloyd models are presented as Eq. 2.8 and Eq. 2.16 respectively. These formulations are repeated here for convenience:

$$\text{MRTD}_R = \frac{\left(\frac{\pi^2}{8}\right) \text{SNR}_{\text{thr}} \text{NETD}}{H_{\text{sys}}(f_x) L \int_{-\infty}^{\infty} H_L^2 H_{\text{sys}}^2 df_y} \left[\frac{\Delta y_i v}{\Delta f_n F_{\text{dot}} t_e} \int_{-\infty}^{\infty} \frac{S(f_x)}{S(f_{\text{ox}})} H_{\text{elect}}^2 H_{\text{sys}}^2 H_L^2 H_W^2 H_d^2 df_x df_y \right]^{0.5} \quad (\text{B.1})$$

and,

$$\text{MRTD}_L = \frac{0.66(\text{SNR}_{\text{thr}})(\text{NETD})(f_x)}{(\Delta f_n)^{0.5} H_{\text{sys}}(f)} \left(\frac{\alpha \beta}{F_{\text{dot}} t_e \tau_d} \right)^{0.5} \quad (\text{B.2})$$

The assumed formulation for conversion between the two models is given by:

$$\chi = \frac{\text{MRTD}_R}{\text{MRTD}_L} \quad (\text{B.3})$$

Removing the terms common to both formulations; namely, SNR_{thr} , F_{dot} , t_e , NETD , $\text{MTF}(f)$ and Δf_n ; and, recognizing that the scan velocity is given by:

$$v = \frac{\alpha}{\tau_d}, \text{ and} \quad (\text{B.4})$$

$$\Delta y_i = \beta, \quad (\text{B.5})$$

yields the following:

$$\chi = \frac{\left(\frac{\pi^2}{8}\right) \left[\int_{-\infty}^{\infty} \int_0^{\infty} \frac{S(f_x)}{S(f_{ox})} H_{\text{elect}}^2 H_{\text{sys}}^2 H_L^2 H_W^2 H_d^2 df_x df_y \right]^{0.5}}{0.66 \cdot L \cdot f_x \cdot \int_{-\infty}^{\infty} H_L^2 H_{\text{sys}}^2 df_y}. \quad (\text{B.6})$$

Since the bar height is seven times the width, and the spatial frequency is given by the inverse of the spatial period (2W):

$$L \cdot f_x = 7W \cdot \frac{1}{2W} = \frac{7}{2}, \quad (\text{B.7})$$

and,

$$\left(\frac{\pi^2}{8}\right) \left(\frac{2}{7}\right)^{0.5} = 0.66, \quad (\text{B.8})$$

gives:

$$\chi = \frac{\sqrt{2} \left[\int_{-\infty}^{\infty} \int_0^{\infty} \frac{S(f_x)}{S(f_{ox})} H_{\text{elect}}^2 H_{\text{sys}}^2 H_L^2 H_W^2 H_d^2 df_x df_y \right]^{0.5}}{\sqrt{7} \int_{-\infty}^{\infty} H_L^2 H_{\text{sys}}^2 df_y}. \quad (\text{B.9})$$

Applying an unconventional 'simplification':

$$\sqrt{7} = \frac{L}{\sqrt{WL}}, \quad (\text{B.10})$$

If the length of a target bar in the vertical direction is large compared to the system vertical response (which is almost always the case) then the vertical transfer function effects can be ignored. The bar (contrast), in effect, is undegraded in the vertical direction. Then,

$$\int_{-\infty}^{\infty} \frac{S(f_x)}{S(f_{ox})} H_{\text{sys}}^2 H_L^2 df_y = 1. \quad (\text{B.11})$$

The post-detector transfer functions are one-dimensional in x, and therefore the vertical system response can be set to one for these terms as well:

$$\int_0^{\infty} H_{\text{elect}}^2 H_W^2 H_d^2 df_y = 1, \quad (\text{B.12})$$

which yields the final form of the correction factor:

$$\chi = \frac{\sqrt{2WL} \left[\int_0^{\infty} H_{\text{elect}}^2 H_W^2 H_d^2 df_x \right]^{0.5}}{L \int_{-\infty}^{\infty} H_L^2 H_{\text{sys}}^2 df_y} \quad (\text{B.13})$$

APPENDIX C. FLIR92

Several second generation models have been developed incorporating the modeling considerations of Chapter III to varying degrees. The most notable of these is FLIR92, a product of the U.S. Army's Night Vision and Electronic Sensors Directorate (NVESD). [Refs. 16,24] The NVESD is a direct descendent of the previously named Night Vision Laboratory (NVL). FLIR92 is the de facto standard for second generation modeling efforts, and a key predictor used to evaluate any TIS introduced for DOD consideration. FLIR92 is a computer-based thermal imaging system MRTD and MDTD predictor released in 1992. It is a direct descendent of the 1975 NVL model, and a refinement of the earlier released FLIR90. Like its predecessors, FLIR92 is a computer based predictor, developed to aid the Army in analyzing potential TIS systems for various applications. Available in executable code for PC's or UNIX, it is designed to handle staring imagers and parallel scanning systems, as well as first generation serial scanning systems. It is capable of providing MRTD, MDTD, and NETD predictions for all of the above systems. Unlike previous models, FLIR92 is fully configuration managed, so model improvements and adjustments can be incorporated through controlled revisions. It is a 'static' model, it does not account for target acquisition or tracking problems. Also, it is limited to imaging systems operating in the thermal region of the spectrum.

Like the 1975 model, FLIR92 is based on a signal to noise analysis degraded by a system MTF. The MTF's incorporated are more sophisticated and flexible than the earlier models, but the basic application of linear systems theory remains unchanged from 1975. The model has 'generic' MTF's built in for default component analysis, but also allows the user the flexibility of inputting measured MTF's from a particular sub-system component, if desired. The most revolutionary aspect of the FLIR92 model is its treatment of noise. The model incorporates the full 3-D noise analysis scheme as discussed in Chapter III. This noise analysis results in correction factors to be applied to the vertical and horizontal

MRTD calculations. The vertical MRTD predictions from FLIR92 are considered reliable, an improvement over earlier models.

FLIR92 compromises on the treatment of sampling in imaging systems by cutting off MRTD predictions at the system Nyquist frequency. On one hand, this is conservative because significant information is often available above the Nyquist frequency, although it may not be perfectly resolved. On the other hand, this liberally ignores the effects of aliasing felt at frequencies below Nyquist. Finally, in FLIR92, the eye is treated as a synchronous integrator instead of a matched filter. This method gives nearly the same results as the matched filter model for periodic targets, but is much easier to model [Ref. 16]. FLIR92's treatment of 3-D noise, including MRTD correction factors and eye/brain integration factors is contained in Chapter III. This appendix describes FLIR92's treatment of MTF modeling, sampling and aliasing, and MRTD/MDTD correction factors. Following these descriptions, the input data files for the Amber and Mitsubishi systems are included. Finally, the output of FLIR92 for both of the second generation systems used in the laboratory is also presented.

A. MTF ANALYSIS

The MTF analysis of FLIR92 is more complex than in its predecessor. Like the older models, FLIR92 groups the individual component MTF's into categories; pre-filter, temporal post-filter, and spatial post-filter. Each category is made up of a cascade of individual component MTF's. In each case, individual component MTF's may be either entered in exactly, or may be approximated by a default model. Most of the MTF's listed are optional, while some apply only to specific cases. If the MTF does not apply to the particular system, its value is set to 1.0. Each category also allows the user to input a 'spare' MTF to make the category MTF a better match for the modeled system. The subscript 'z' indicates that the variable exists in both the vertical and horizontal directions, and should be included in both analyses with the appropriate subscript (v or h).

1. Pre-filter MTF

The pre-filter MTF, $H_{\text{PRE}}(f)$, includes components of the system from the target to the detector array. Components such as system optics, detector spatial properties, focal plane array (FPA) integration, and image motion effects are included. The pre-filter MTF is analogous to the image formation filter presented in Chapter III. The pre-filter MTF is given by:

$$H_{\text{PRE}}(f) = H_{\text{opt}} H_{\text{ogb}} H_{\text{det}} H_{\text{di}} H_{\text{ssp}} H_{\text{ml}} H_{\text{mr}} H_{\text{ms}}(f) , \quad (\text{C.1})$$

where the individual component MTF's are described in Table C.1.

TABLE C.1. Pre-filter MTF's

Symbol	Component
H_{opt}	Optical diffraction limited
H_{ogb}	Optical geometric blur
H_{det}	Detector spatial
H_{di}	FPA integration
H_{ssp}	Sample-scene phasing
H_{ml}	Linear image motion
H_{mr}	Random image motion
H_{ms}	Sinusoidal image motion

The first of these elements is the system optics MTF, composed of a diffraction limited MTF (assumes cylindrical symmetry):

$$H_{\text{opt}}(f) = \frac{2}{\pi} \left(\arccos \left(\frac{\lambda f}{D_o} \right) - \left(\frac{\lambda f}{D_o} \right) \left(1 - \left(\frac{\lambda f}{D_o} \right)^2 \right)^{0.5} \right) , \quad (\text{C.2})$$

and a geometric blur MTF accounting for optical aberrations:

$$H_{\text{ogb}}(f) = \exp(-2\pi^2 \sigma_g^2 f^2) . \quad (\text{C.3})$$

Second in the pre-filter cascade is the detector spatial MTF:

$$H_{\text{det}}(f) = \frac{\sin(\pi\Delta_z f)}{\pi\Delta_z f} , \quad (\text{C.4})$$

where Δ_z is the physical dimension of the individual detector element in either the vertical or horizontal direction.

Scanning systems have a finite detector integration time which is accounted for by the FPA integration MTF:

$$H_{\text{di}}(f) = \frac{\sin(\pi f_t v_s t_i)}{\pi f_t v_s t_i} , \quad (\text{C.5})$$

where t_i is the finite integration time of the detector, and v_s is the scan velocity. Finally, in the pre-filter cascade, MTF's are available to model sample scene phasing, and image motion. Image motion is further subdivided into linear, sinusoidal, and random motion MTF's, each describing a relative target imager motion. For still target modeling, such as in a laboratory environment, all of these are set to 1.0. They can, however, aid in the proper modeling of a fielded system where image motion or scene phasing are expected.

2. Temporal Post-filter

All of the pre-filter MTF's are spatial frequency dependent. After the detector, there are both temporal and spatial frequency degradation effects. Combined, they make up the image reconstruction filter presented in Chapter III. In FLIR92, the post-filter MTF's are subdivided into temporal and spatial components.

The temporal post-filter MTF is given by:

$$H_{\text{TPF}}(f) = H_{\text{dt}} H_{\text{ehp}} H_{\text{elp}} H_{\text{eb}} , \quad (\text{C.6})$$

and is made up of the individual component MTF's described in Table C.2.

TABLE C.2. Temporal Post-filter MTF's

Symbol	Component
H_{dt}	Detector temporal
H_{ehp}	Electronics low-frequency
H_{elp}	Electronics high-frequency
H_{eb}	Electronic boost

Each of these individual component MTF's represents a temporal degradation of the displayed image. The temporal post-filter is used for scanning systems only, in the direction of scan. It is not appropriate for staring arrays, or for directions normal to the scan direction. For staring arrays, this filter is set to 1.0. Each of these MTF's is given below:

$$H_{dt}(f_t) = \left(1 + \left(\frac{f_t}{f_{dt}}\right)^2\right)^{-0.5}, \quad (C.7)$$

$$H_{ehp}(f_t) = \frac{\left(\frac{f_t}{f_{ehp}}\right)^n}{\left(1 + \left(\frac{f_t}{f_{ehp}}\right)^{2n}\right)}, \quad (C.8)$$

$$H_{elp}(f_t) = \left(1 + \left(\frac{f_t}{f_{dt}}\right)^{2n}\right)^{-0.5} \quad (C.9)$$

$$H_{eb}(f_t) = 1 + \frac{B_a - 1}{2} \left(1 - \cos\left(\frac{\pi f_t}{f_b}\right)\right). \quad (C.10)$$

3. Spatial Post-filter

The spatial post-filter models the system "back end" [Ref. 16]. The spatial post filter is given by:

$$H_{SPF}(f) = H_{eom} H_{dig} H_d H_{ccd} H_{dsh} H_{eye}(f), \quad (C.11)$$

and is made up of the individual component MTF's contained in Table C.3.

TABLE C.3. Spatial Post-filter MTF's

Symbol	Component
H_{eom}	Electro-optic multiplexor
H_{dig}	Digital filter
H_{d}	CRT display
H_{ccd}	CCD Charge transfer
H_{dsh}	Display sample and hold
H_{eye}	Limiting eye/brain

The electro-optically multiplexed system is given by:

$$H_{\text{eom}}(f) = \frac{\sin(\pi f \delta_{\text{led}})}{(\pi f \delta_{\text{led}})} , \quad (\text{C.12})$$

where δ_{led} is the angular subtense of an individual LED element (Of course, this MTF is only included for electro-optically multiplexed systems. It is set to 1.0 for systems with only electronic multiplexing).

The model incorporates an MTF for linear phase symmetrical impulse response digital filters. For odd N:

$$H_{\text{dig}}(f) = \sum_{i=0}^{\frac{(N-1)}{2}} a_i \cos\left(2\frac{\pi i f}{f_{\text{co}}}\right) , \quad (\text{C.13})$$

for even N:

$$H_{\text{dig}}(f) = \sum_{i=1}^{\frac{N}{2}} a_i \cos\left(2\frac{\pi\left(i - \frac{1}{2}\right)f}{f_{\text{co}}}\right) , \quad (\text{C.14})$$

where N is the number of samples, a_i is the filter coefficient, and f_{co} is the filter cutoff frequency.

If the display is a standard CRT, the model assumes a Gaussian spot MTF, just like earlier MTF models. If the monitor is non-standard, another MTF may be entered. The Gaussian spot MTF is given by:

$$H_d(f) = \exp(-2\pi^2 \sigma^2 f^2) \quad . \quad (C.15)$$

The CCD charge transfer efficiency MTF is:

$$H_{ccd}(f) = \exp\left(-N(1 - \epsilon)\left(1 - \cos\left(2\pi\frac{f}{r_N}\right)\right)\right) \quad (C.16)$$

The eye sample and hold MTF is given by:

$$H_{dsh}(f) = \frac{\sin(\pi\delta f)}{\pi\delta f} \quad . \quad (C.17)$$

Finally, the post-filter spatial MTF includes a limiting eye MTF based on the angular subtense of the eye. This is a function of the ambient light level and the system magnification:

$$H_{eye}(f) = \exp\left(\frac{-\Gamma f}{2M}\right) \quad . \quad (C.18)$$

As with the other category MTF's, a spare filter is also available if the above transfer functions do not adequately describe the system.

4. System MTF

The complete system MTF is given by:

$$H_{SYS}(f) = H_{PRE}H_{TPF}H_{SPF}(f) \quad . \quad (C.19)$$

This MTF is used in system calculations of the MRTD and MDTD.

The system noise filter is defined as the overall filter which acts on detector noise. It is used in the calculation of eye/brain spatial integration effects [Ref. 16]. It is given by:

$$H_{NF}(f) = H_{di}H_{ehp}H_{TPF}H_{SPF}(f) \quad . \quad (C.20)$$

B. SAMPLING EFFECTS

The literature abounds with complex mathematical models and procedures for accounting for sampling in imaging systems of all types [Refs. 17-23]. Unfortunately, most of these presentations are more suitable to understanding sampling effects, and are not amenable to incorporation into a practical predictive model like FLIR92. Unquestionably, this area requires further study. Sampling effects are rather quickly disposed of in FLIR92 by the rejection of any frequencies above the calculated system Nyquist frequency. No output is given for frequencies above this cutoff. Unfortunately, the insidious effects of aliasing are felt below this threshold as well, and are ignored by this model. FLIR92 presupposes that aliasing and other deleterious sampling artifacts can be effectively eliminated by good design. It is true that frequencies above Nyquist cannot be fully reconstructed by the system. Therefore, at these frequencies, MRTD can never be reached by strict definition. FLIR92 does not choose to model undersampled frequencies as aliasing noise in the current version. Instead, for frequencies greater than the calculated Nyquist frequency, the system does not calculate an MRTD at all. This can be frustrating to the user because it places a tight bound on system modeling, and appears inconsistent with the fact that the effects of aliasing on frequencies below cutoff are ignored. The only sampling effect considered by the FLIR92 is the sample scene phasing effect included in the pre-filter MTF. This MTF is inserted to account for degradation caused by the scene being projected onto the detector array in a less than optimum position. Use of this feature is optional.

C. SYSTEM NOISE

In FLIR92, the modeling of each of the seven noise components is implemented by one of two methods. The process of predicting the directional noise terms for a particular system from simple system parameters is difficult at best, and calls for some flexibility in modeling methods. FLIR92 provides this flexibility. The first (default) method involves scaling each of the noise factors to the random pixel noise. This method selects a scaling

factor for each of the other six noise components referenced to the value for σ_{tvh} . The value for σ_{tvh} is calculated in a manner analogous to the method used in first generation models to calculate the NETD, and is given as Eq. 3.9. The default scaling factors used based on this value of σ_{tvh} depend on the type of system being modeled, and are derived from a series of measurements made by NVESD with several different system types [Ref. 16]. Table C.4 shows the default value for staring systems, and Table C.5 shows the default values used for scanning systems. Note the default values for the scanning system are selected by choosing a relative noise level; either low, moderate, or high. Because the system noise sources add in quadrature, only the most significant noise components are given scale values. The remaining directional noise components are set to zero.

TABLE C.4. Default scale factors for staring systems

Noise component	Default value
σ_{vh}	.40

TABLE C.5. Default scale factors for scanning systems

Noise component	low noise	moderate noise	high noise
σ_{tv}	.25	.75	1.0
σ_v	.25	.75	1.0

The second way to implement the 3-D noise components is to enter actual measured values if they can be obtained. The measurement procedure was presented by D'Agostino in 1991 [Ref. 13]. Although this will give more accurate predictions, it is obviously difficult to measure these values.

D. MRTD PREDICTION

FLIR92 uses the MTF models, noise data, and eye/brain spatial and temporal integration factors to calculate a predicted MRTD in both the horizontal and vertical directions. The correction factors used are given in Chapter III. FLIR92 takes the geometric mean of the horizontal and vertical MRTD values to give a two dimensional MRTD value. All three values for MRTD are provided in the output.

E. SYSTEM OUTPUT

The two dimensional MRTD is FLIR92's final output. This spatial frequency dependent MRTD function can, for example, be inserted into other electro-optic decision aids such as EOTDA, or NVESD ACQUIRE [Ref. 16] to develop range predictions for proposed systems. The same information is provided for MDTD. FLIR92 was run for the systems used in the lab experiments, and the results were plotted. The plots of the data are included as Figs. C.1 and C.2. These results are compared to VISMODII predictions and measured laboratory results in Chapter VI.

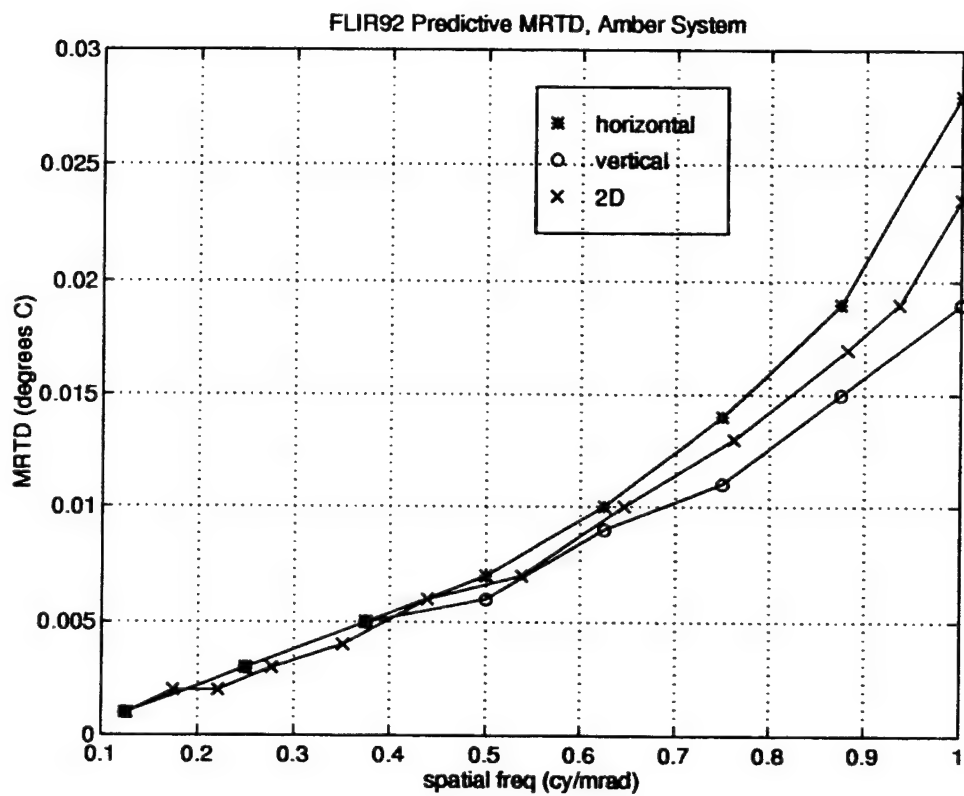


Figure C.1. FLIR92 predicted MRTD for Amber system

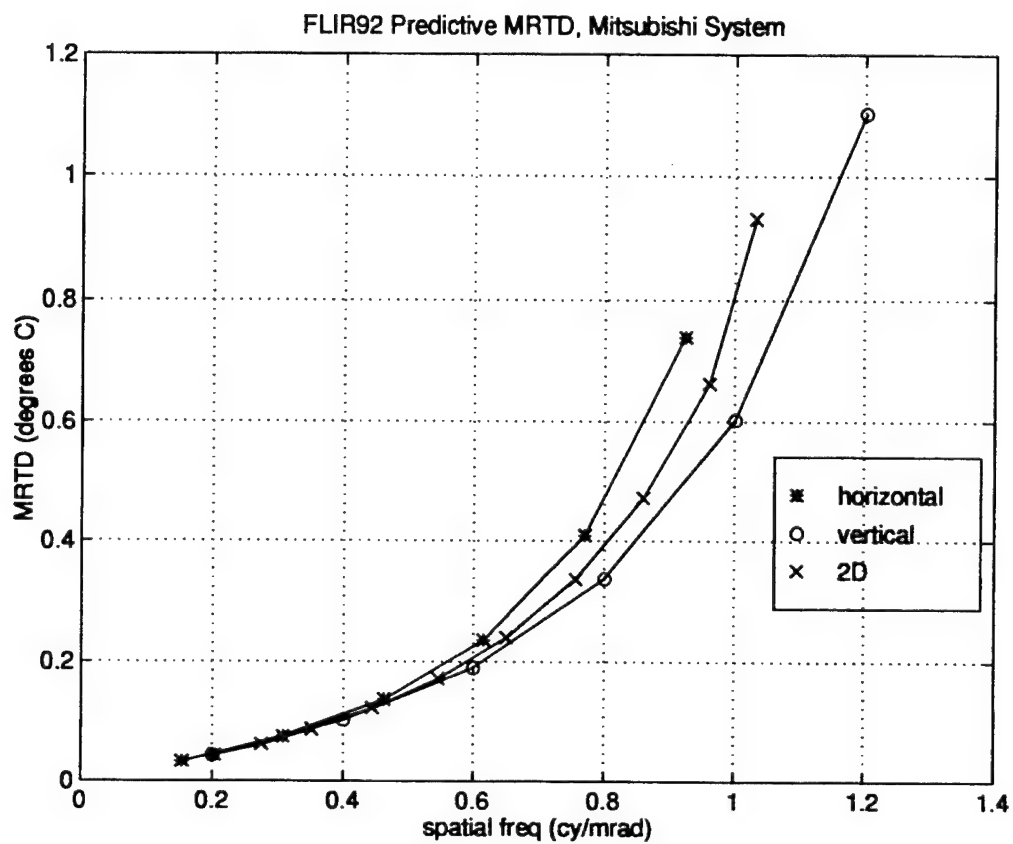


Figure C.2. FLIR92 predicted MRTD for Mitsubishi system

APPENDIX D. LABORATORY MEASUREMENT RESULTS

This appendix contains the tabulated results for the laboratory measurements made. Tables D.1 and D.2 contain the results for the AMBER system. Figures D.1 and D.2 are the plots of the tabulated data. The average and two dimensional MRTD plots are contained in Chapter IV.

TABLE D.1. Amber system measured horizontal MRTD

Spatial freq (cy/mrad)	Trial 1 (degrees C)	Trial 2 (degrees C)	Average (degrees C)
.10	.33	.28	.31
.15	.33	.31	.32
.20	.33	.17	.25
.25	.28	.39	.33
.30	.36	.31	.33
.375	.33	.44	.39
.40	.39	.28	.33
.50	.33	.28	.31
.60	.44	.44	.44
.625	.42	.33	.38
.70	.56	.56	.56
.75	.61	.61	.61
.80	.58	.75	.67
.875	.67	.83	.75
1.0	.78	1.6	1.17
1.2	1.5	2.6	2.01

TABLE D.2. Amber system measured vertical MRTD

Spatial freq (cy/mrad)	Trial 1 (degrees C)	Trial 2 (degrees C)	Average (degrees C)
.10	.33	.28	.31
.15	.33	.31	.32
.20	.33	.17	.25
.25	.28	.39	.33
.30	.36	.31	.33
.375	.39	.39	.39
.40	.44	.44	.44
.50	.19	.56	.38
.60	.25	.64	.44
.625	.42	.61	.51
.70	.56	.81	.68
.75	1.1	.89	1.0
.80	1.1	.83	.94
.875	1.6	1.0	1.3
1.0	1.6	1.1	1.4
1.2	3.3	3.3	3.3

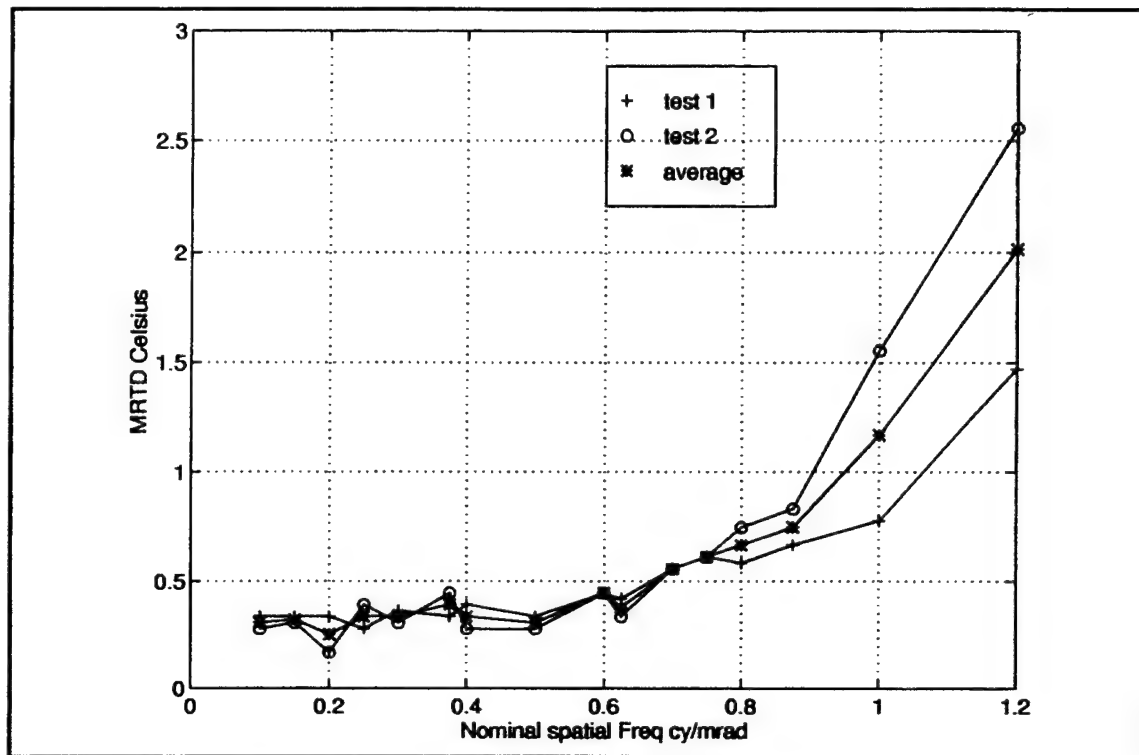


Figure D.1. AMBER system, horizontal MRTD trials

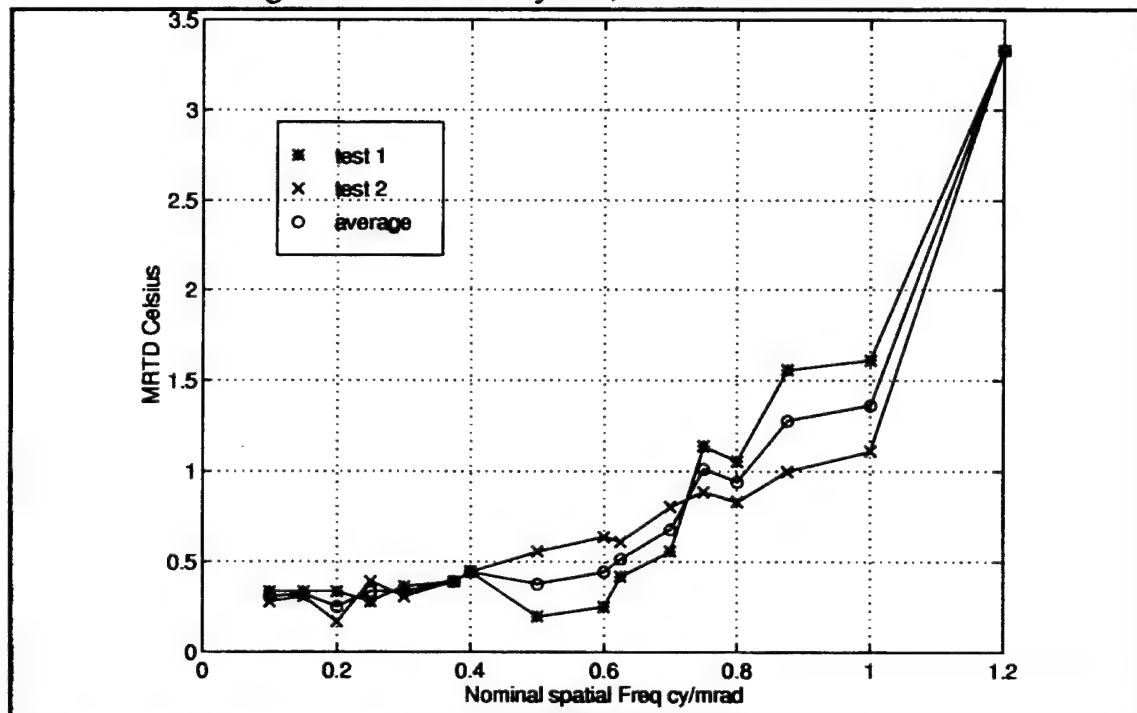


Figure D.2. AMBER system, vertical MRTD trials

Tables D.3 and D.4 contain the measurement results for the Mitsubishi system. This data is plotted in Figs. D.3 and D.4. The average and two dimensional plots are contained in Chapter IV.

TABLE D.3. Mitsubishi system measured horizontal MRTD

Spatial freq (cy/mrad)	Trial 1 (degrees C)	Trial 2 (degrees C)	Average (degrees C)
.10	.08	.06	.07
.15	.08	.06	.07
.20	.12	.18	.15
.25	.15	.13	.14
.30	.28	.11	.19
.375	.26	.13	.19
.40	.28	.14	.21
.50	.26	.13	.19
.60	.28	.19	.24
.625	.31	.19	.25
.70	.36	.31	.33
.75	.28	.25	.26
.80	.36	.36	.36
.875	.31	.31	.31
1.0	.44	.33	.39
1.2	.78	.78	.78

TABLE D.4. Mitsubishi system measured vertical MRTD

Spatial freq (cy/mrad)	Trial 1 (degrees C)	Trial 2 (degrees C)	Average (degrees C)
.10	.08	.06	.07
.15	.08	.06	.07
.20	.17	.11	.14
.25	.22	.11	.17
.30	.25	.11	.18
.375	.22	.14	.18
.40	.39	.11	.25
.50	.39	.19	.29
.60	.44	.31	.38
.625	.44	.47	.46
.70	.81	.44	.63
.75	.83	.75	.79
.80	1.1	.70	.90
.875	1.3	.69	1.3
1.0	**	**	**
1.2	**	**	**

** beyond spatial resolution of system, no MRTD possible.

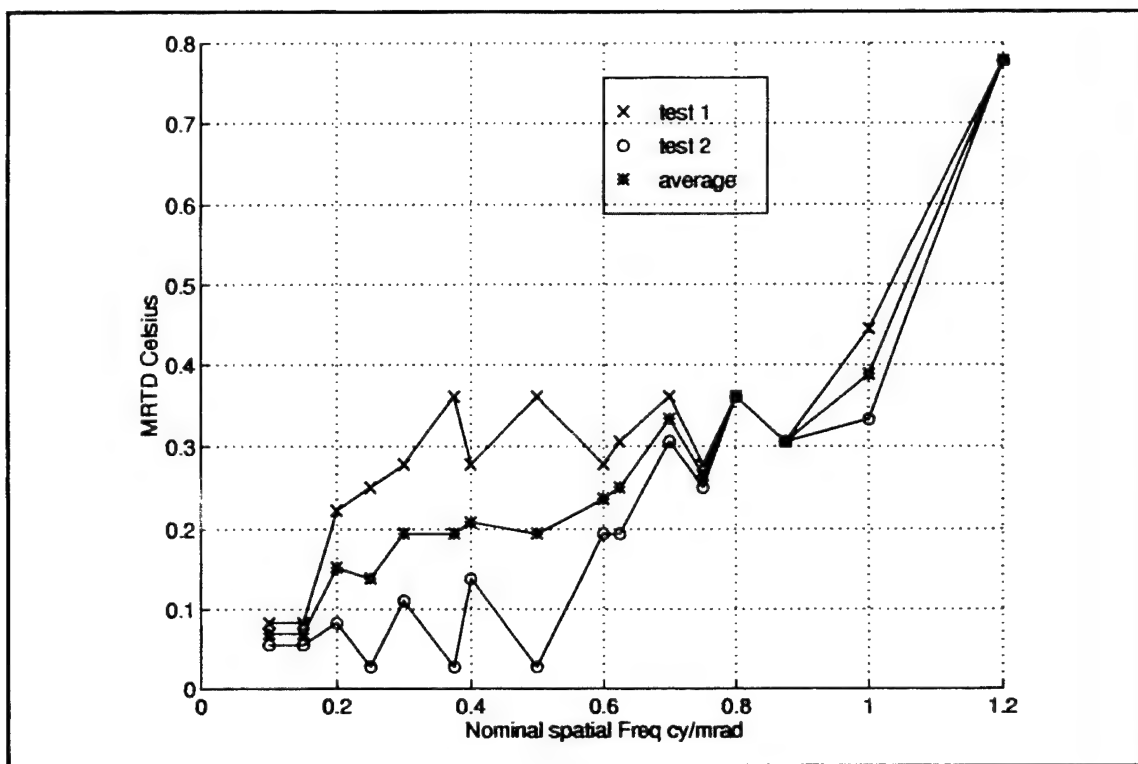


Figure D.3. Mitsubishi system, horizontal MRTD trials

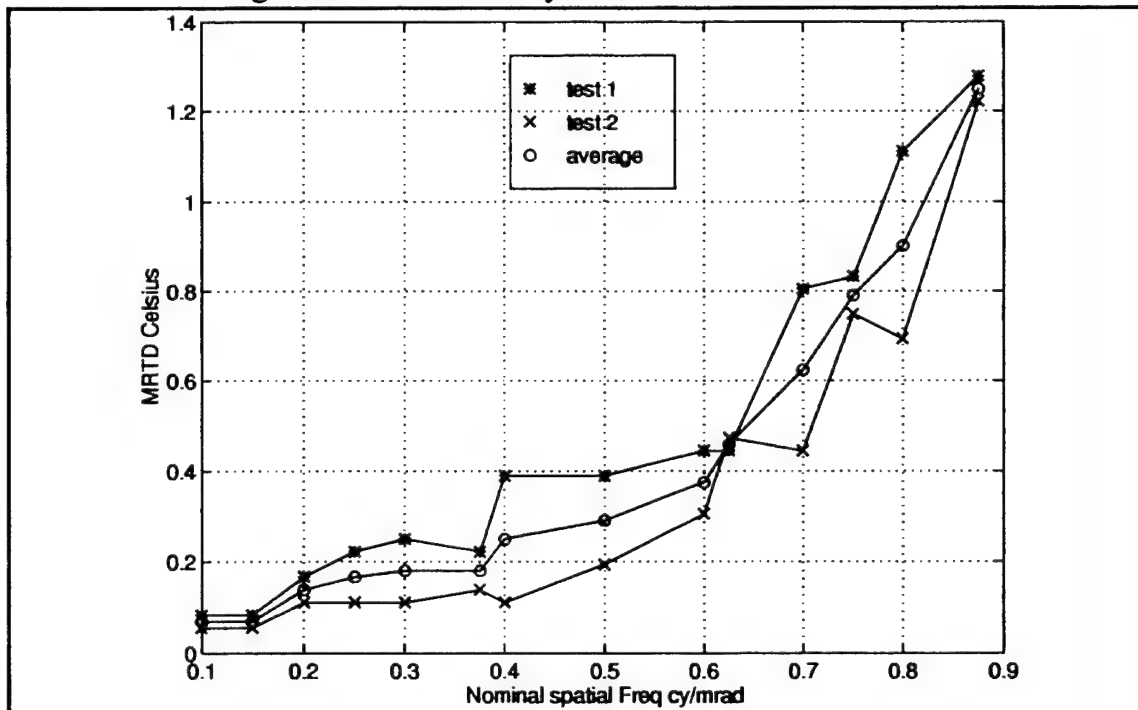


Figure D.4. Mitsubishi system, vertical MRTD trials

Tables D.5, D.6, and D.7 contain the data obtained in the 'objective' MRTD measurements. This data is plotted in Chapter IV, and discussed in Chapter V.

TABLE D.5. Constant SNR = 6.0

Spatial freq (cy/mrad)	delta T (Celsius)
0.2	2.9
0.3	2.9
0.4	3.35
0.5	3.6
0.6	4.25
0.7	4.3
0.8	4.85

TABLE D.6. Constant delta T = 3.5 Celsius

Spatial freq (cy/mrad)	SNR
0.2	6.25
0.4	6.23
0.5	5.5
0.6	4.75
0.7	4.25
0.8	3.38

TABLE D.7. Constant spatial frequency = 0.5 cy/mrad

SNR	delta T
1	0.8
2	1.5
3	1.8
4	2.35
5	3.0
6	3.7
7	4.2
8	5.0

APPENDIX E. MATLAB CODE

An example of the MATLAB script files that produced the VISMODII prediction curves are contained in this appendix. There are three files. The first, 'v2', is the shell program that contains the TIS information and the preliminary calculations. It calls the second program, 'effcnt', to calculate the contrast transference parameter. The 'effcnt' program calls 'alias' to calculate the aliasing and sample scene phase terms. Control is then handed back to 'v2', which calculates the ΔT_{sc} term. V2 also calculates and plots the MRTD curves.

A. V2.M

```
%%%%%%%%%%
% Mike Groen
% 11/01/95
% VISMODII MITSUBISHI
% Given system parameters, this script file will predict
% MRTD curve for staring arrays
% requires: effcnt.m, alias.m,formmtf.m,reconmtf.m,plotmtf.m
%
%%%%%%%%%%
clear;
clg;
%%%%%%%%% Define spatial frequencies of interest (cy/mrad)
fbar = [.05:.05:1.2];
% fbar=.6
%%%%%%%%% System Parameters
% number of horizontal detector elements
nh=512;
% number of vertical detector elements
nv=512;
% detector active horizontal dimension (um)
a=16.24;
% detector active vertical dimension (um)
b=12.49;
% detector pitch, horizontal (um)
hpitch = 26;
% detector pitch, vertical (um)
vpitch = 20;
% system f-number
fnumber = 1.4;
% focal length (mm)
focal = 50;
% frame rate (Hz)
Fdot=60;
% clock-out factor (determines integration time)
clock = .97;
```

```

Dstar=5e10; % peak D-star (cm-Hz1/2/Watt)
lambdap=5.0; % peak wavelength (um)
lambda1=3.0; % wavelength 1 (um)
lambda2=5.0; % wavelength 2 (um)
fxec=2.3e6; % electronic cut off (Hz)
monfac=.25; % monitor gaussian rms factor normalized by alpha
poles= 1; % number of poles for electronic filter
blurspot = 0; % standard deviation of blur spot diameter (mrad)
theh = 0; % average angle off array center image is (rad)
thev = 0; % ditto, vertical (rad) [usually zero or .785]
lloyd2 = 1.4388e4;
Tbg = 300;
To = .95;
delTsc = 0;
sigmahv = .4;
SNRthr = 6.0;
te = .2;
%
% preliminaries
%
avglambda=0.5*(lambda1+lambda2); % ave lambda
opdia = focal/fnumber; % optical diameter(mm)
alpha=hpitch/focal; % alpha in mrad
beta=vpitch/focal; % beta in mrad
ao=pi*(opdia/2)^2; % area of collecting lens (mm^2)
td=clock/Fdot; % compute dwell time (sec)
fopt=opdia/avglambda; % optical cut off in cy/mr
fsh = focal/hpitch; % horizontal sampling frequency (cy/mr)
fsv = focal/vpitch; % vert samp freq (cy/mr)
tclock=nh*nv*Fdot;
fth=alpha*tclock;
ftv=beta*tclock/nh;
fehos = fxec*focal/(Fdot*nh*hpitch); % out of clock direction, elec cutoff
% in (cy/mrad)
fevis = fxec*focal/(Fdot*nh*nv*vpitch); % in clock out direction (cy/mrad)
%sspmaxh = hpitch/2;
sspmaxh=0;
%sspmaxv = vpitch/2; % max sample scene phase error
sspmaxv=0;
%%%%%%%%%%%% Calculate contrast function
%%%%%%%%%%%%

```

```

[ctf,vctf,delf,alias] =
meffcnt(fbar,fsh,fsv,fopt,alpha,beta,blurspot,theh,thev,fehos,fevis,poles,monfac,sspmmaxh,
sspmmaxv);
%           plot contrast transfer function
plot(fbar,ctf)
axis([0 2 0 1])
xlabel('Spatial Frequency (cy/mrad)')
ylabel('CTF')
title('Contrast Transfer Function, horizontal MRTD')
%keyboard
plot(fbar,vctf)
axis([0 2 0 1])
xlabel('Spatial Frequency (cy/mrad)')
ylabel('CTF')
title('Contrast Transfer Function, vertical MRTD')
%keyboard
%%%%%%%%%%%% Find system delta T critical
%%%%%%%%%%%%
if delTsc > 0 % that is, it's given

        delTsc = delTsc;

else % calculate delTsc
    % NETD part first

        refbw = (pi/4)*(1/td);
        n1 = pi*sqrt(a*1e-4*b*1e-4*refbw);
        d1 = (alpha*beta*1e-6*To*ao*1e-2*Dstarp);
        d2 = lloyd2/(lambdap*Tbg^2)*(quad2var('sre', lambda1, lambda2,
Tbg));
        NETD = n1/(d1*d2)
    % SNR improvements
        tn2 = (1+sigmavh^2)*pi^2*SNRthr/(8*sqrt(te*Fdot));
    % bandwidth correction
%       MTFsys = abs(MTFrf);
%       totbw = sum(MTFsys)*delf*tclock;
%       bwcorr = sqrt(totbw/refbw);
    % new delTsc
%       delTsc = tn2*NETD*bwcorr;
end
delTsc=.07;
%%%%%%%%%%%% Find system MRTD
%%%%%%%%%%%%

```

```

MRTDH = delTsc./ctf;MRTDV = delTsc./vctf;
plot(fbar,MRTDH, 'co')
axis([0 1.6 0 3])
xlabel('Spatial Frequency (cy/mrad)')
ylabel('MRTD')
title('Mitsubishi system MRTD, nnyn')
%keyboard
hold on
plot(fbar,MRTDV, 'y*')
axis([0 1.2 0 1.4])
%xlabel('Spatial Frequency (cy/mrad)')
%ylabel('MRTD')
%title('Vertical MRTD')
%%%%%%%%%%%%%%%%%%%%%%%%%%%%%%%%%%%%%%%%%%%%%%%%%%%%%%%%%%%%%%%%%%%%%%%% 2D MRTD %%%%%%%%%
MRTD2D = (MRTDH+MRTDV)./2;
plot(fbar, MRTD2D, 'g+')
legend('Horizontal', 'Vertical','2D MRTD')
plot(fbar,MRTDH, 'c')
plot(fbar,MRTDV, 'y')
plot(fbar, MRTD2D, 'g')
grid
save mhz2nnyn
%print
%exit

```

B. EFFCNT.M

```

%           Mike Groen
%
%           This script creates a standard four bar pattern of freq
%           specified by the user. It then passes it through a simulated
%           TIS ( as represented by an MTF and aliasing), and produces the
%           reconstructed pattern at the output.
%           Loops through the range of spatial freq's desired, and
%           calculates the contrast function
function [contrast,vercon,MTFrf,delf,ACF ] = meffcnt(fbar,fsh,fsv,fopt,alpha,beta,
blurspot, theh, thev,fxec,poles,monfac,fth,ftv,sspmaxh,sspmaxv);
%clear;fbar=.6;fsh=2;fsv=2;fopt=3.4;alpha=.25;beta=.55;blurspot=0;theh=0.785;thev=0.
785;
d=size(fbar);d2=d(2);
%%%%%%%%%%%%%%%%%%%%%%%%%%%%%%%%%%%%%%%%%%%%%%%%%%%%%%%%%%%%%%%%%%%%%%%%
% create bar pattern
%%%%%%%%%%%%%%%%%%%%%%%%%%%%%%%%%%%%%%%%%%%%%%%%%%%%%%%%%%%%%%%%%%%%%%%%

```

```

col1 = zeros(130,10);
col2 = [zeros(30,10);ones(70,10);zeros(30,10)];
col3 = zeros(130,93);
row1 = zeros(63,256);
A=[row1;col3,col2,col1,col2,col1,col2,col1,col2,col3;row1];
V=A';
%%%%%% transform A into spatial freq domain
B= fft2(A);w=fft2(V);
b=abs(B);x=abs(w);
%%%%%%%%% now loop through frequencies
for counter = 1:d2;
fx=fbar(counter);
%           W refers to the actual width of one bar in mrad
%           the 'del' terms are used to find the appropriate frequency and
%           space scales
W=1/(2*fx);
Nw = 10;      % number of elements in one bar(x)
Nt = 256;     % number of elements in vector(m x m)
delt = W/Nw;
DELt = Nt*W/Nw;
delf = 1/DELt;
DELf = 1/delf;
fmax = DELf/2;
fscale = linspace(-fmax,fmax,256);
xscale = linspace(-DELt/2,DELt/2,256);
yscale = linspace(-DELt/2,DELt/2,256);
%%%%%%%%% create image formation MTF
%%%%%%%%%
umatrix=[];
ux=linspace(.01,fmax,128);
uy=ux';
% make 2D xfer fcn
for count =1:128;
        gaussu = sqrt(ux(count)^2.+uy.^2);
        umatrix = [umatrix, gaussu];
end
% DIFFRACTION LIMITED OPTICAL MTF.  (diffraction limited,circular aperture)
c1=umatrix ./fopt;
c2=sqrt(1-c1.^2);
ro=2/pi.*(acos(c1)-(c1.*c2));
% GEOMETRIC BLUR OPTICAL MTF
f1 = (umatrix.^2).*pi^2.*(-2).*blurspot^2;

```

```

rb = exp(f1);
% HORIZONTAL AND VERTICAL SAMPLE SCENE PHASE MTF
rsh = (2*umatrix(:,1)/fsh)*thesh;
rsh2 = cos(rsh);
rsv = (2*umatrix(1,:)/fsv)*thesh;
rsv2 = cos(rsv);
rs = rsh2*rsv2;
% DETECTOR HORIZONTAL MTF. (for rectangular detector)
c3=pi.*alpha.*umatrix(1,:);
rdh=abs(sin(c3)/c3);
% DETECTOR VERTICAL MTF. (for rectangular detector)
dv=pi.*beta.*umatrix(:,1);
rdv=abs(sin(dv)/dv);
% DETECTOR 2D MTF
rd=rdv*rdh;
MTFif = ro(1,:).*rd(1,:).*rb(1,:).*rs(1,:);
u=ro.*rd.*rb.*rs;
% get mtf in appropriate matrix configuration
mtfif = [u,flipr(u)];
mtfif2 = [mtfif;flipud(mtfif)];
mtfif = fftshift(mtfif2);
%%%%%%%% multiply image spectrum times image formation MTF1
d=fftshift(B);d2 = fftshift(w);
mess = d.*mtfif;mes2 = d2.*mtfif;
% aliasing stuff starts here
aliasterm = zeros(size(mess));
valiasterm = aliasterm;
disp('Calculating aliasterm for:');fbar(counter)
aliasterm = alias(fscale,fsh,fsv,mess,sspmaxh,sspmaxv);
valiasterm = alias(fscale,fsh,fsv,mes2,sspmaxh,sspmaxv);
%% add alias term to filtered scene
withalias= mess + aliasterm;
vertalias = mes2 + valiasterm;
%%%%%%%% Now, create the image reconstruction filter
%%%%%%%%
clear u ux uy K gaussu
umatrix = [];
ux=linspace(.01,fmax,128);
uy=ux';
% make 2D gaussian symmetric xfer fcn
for count =1:128;
gaussu = sqrt(ux(count)^2.+uy.^2);

```

```

        umatrix = [umatrix, gaussu];
end
% ELECTRONICS MTF. (multi-pole low pass filter)
tfreqh=umatrix*fth;
c6=(umatrix ./fxec) .^(2*poles);
re=1 ./sqrt(1+c6));
% ELECTRONICS PTF
        eptf = -atan(umatrix./fxec);
        ptf = exp(j*eptf);
% CRT MONITOR SPATIAL MTF.
        c7=(umatrix ./ (1/alpha)) .^2;
        c8=(monfac) .^2;    % sigma/alpha = .25
        rm=exp(-2 *pi^2 .*c7 .*c8);
MTFrf = (re(1,:).^2).*(rm(1,:).^2);
u=re.*rm.*ptf;
% get mtf in appropriate matrix configuration
mtf2 = [u,flipr(u)];
mtf2a = [mtf2;flipud(mtf2)];
mtf2b = fftshift(mtf2a);
%%%%%%%% multiply image reconstruction times the aliased, filtered, scene
outalias = withalias.*mtf2b;
noalias = mess.*mtf2b;
veral2 = vertalias.*mtf2b;
veral3 = mes2.*mtf2b;
%%%%%%%%%%%%%
%%%%%%%%%%%%% transform back to spatial domain
%%%%%%%%%%%%%
messy = fftshift(outalias);messy2 = fftshift(noalias);
gigo = fftshift(veral2);gigo2 = fftshift(veral3);
C=ifft2(messy);D=ifft2(messy2);E=ifft2(gigo);F=ifft2(gigo2);
C=abs(C);D=abs(D);E=abs(E);F=abs(F);
%%%%%%%%%%%%%
%%%%%%%%%%%%% calculate aliasing contrast reduction
%%%%%%%%%%%%%
aliasnoise = C-D;vertnois = E-F;
ver = aliasnoise(93:163,93:163);aver = vertnois(93:163,93:163);
ACF(counter) = mean(mean(ver));ACF2(counter) = mean(mean(ver));
%%%%%%%%%%%%%
%%%%%%%%%%%%% Find the output contrast value
%%%%%%%%%%%%%
newbar = [D(93:163,98:99)];

```

```

verbar = [F(98:99,93:163)];
m=size(newbar);nu=m(1)*m(2);
high = sum(sum(newbar))/nu;
verhigh = sum(sum(verbar))/nu;
newspace = [D(93:163,108:109)];
verspace = [F(108:109,93:163)];
n=size(newspace);nn=n(1)*n(2);
low = sum(sum(newspace))/nn;
verlow = sum(sum(verspace))/nn;
contrast(counter) =high - low - ACF(counter);
vercon(counter) = verhigh-verlow-ACF2(counter);
if contrast(counter) < 0;
    contrast(counter)=contrast(counter-1)/10;
end
if vercon(counter) < 0;
    vercon(counter) = vercon(counter-1)/10;
end;end

```

```
% Mike Groen
%
% This is the aliasing portion of effcnt.m
function [aliasterm] = alias(fscale,fsh,fsv,mess,b,c)
% % % % % represent aliasing by repeating the filtered spectrum at
% % % % % sampling freq intervals
% % % % % 
aliastx=zeros(256,256);
aliasty=aliastx;
where = find(fscale/fsh >1);
if where == [];
    cent = 256;multiple = 0;
else
    cent = where(1);multiple = 1;
end
start=cent-128;unused = 256-start;
aliastx(:,start:256) = mess(:,1:unused+1);
aliastx=aliastx.*exp(j*2*pi*b*fsh);
aliaslr = fliplr(aliastx);
aliasx = aliastx+aliaslr;
```



```

wherev = find(fscale/fsv >1);
if wherev == [];
    centv = 256;multiplev = 0;
else
    centv = wherev(1);multiplev = 1;
end
startv=centv-128;unusedv = 256-startv;
aliasty(startv:256,:) = mess(1:unusedv+1,:);
aliasty=aliasty.*exp(j*2*pi*c*fsv);
aliasud = flipud(aliasty);
aliasy = aliasty+aliasud;
%%% alias cross terms
aliasyx(startv:256,:) = aliasx(1:unusedv+1,:);
aliasyxud = flipud(aliasyx);
aliasyx = aliasyx+aliasyxud;
aliasxy(:,start:256) = aliasy(:,start:256);
aliasxylr = fliplr(aliasxy);
aliasxy = aliasxy + aliasxylr;
crossterm = multiple*multiplev*(aliasxy+aliasyx);
aliasterm = multiple*aliasx + multiplev*aliasy +crossterm;

```


INITIAL DISTRIBUTION LIST

1. Defense Technical Information Center 2
8725 John J. Kingman Rd., STE 0944
Ft. Belvoir, VA. 22060-6218

2. Dudley Knox Library, Code 013 2
Naval Postgraduate School
Monterey, CA. 93943-5101

3. Director, Training and Education 1
MCCDC, Code C46
1019 Elliot Rd.
Quantico, VA 22134-5027

4. Chairman, Code EC. 1
Department of Electrical and Computer Engineering
Naval Postgraduate School
Monterey, CA. 93943-5121

5. Chairman, Code PH. 1
Department of Physics
Naval Postgraduate School
Monterey, CA 93943-5117

6. Prof. Ron J. Pieper, Code EC/Pr 1
Department of Electrical and Computer Engineering
Naval Postgraduate School
Monterey, CA. 93943-5121

7. Prof. Alfred W. Cooper, Code PH/Co. 1
Department of Physics
Naval Postgraduate School
Monterey, CA 93943-5117

8. Naval Command and Control and Oceanic Surveillance Center 1
RDT&E division, Attn: Dr. J.H. Richter, Code 54
53570 Silvergate Ave.
San Diego, CA 92152-5230

9. Program Executive Office, Theater Air Defense 1
Attn: J.E. Misanin, Code D233
2531 Jefferson Davis Hwy
Arlington, VA 22242-5170
10. Captain Michael S. Groen 2
48 West 37th St.
Holland, MI 49423